Molecular Dynamics Study of Model Systems Showing Dynamic Heterogeneity

by

Xinyi Wang

A thesis submitted in partial fulfillment of the requirements for the degree of

Doctor of Philosophy

in

Materials Engineering

Department of Chemical and Materials Engineering

University of Alberta

Abstract

Glass-formation is a ubiquitous phenomenon that is often observed in a broad class of materials ranging from biological matter to commonly encountered synthetic polymer, as well as metallic and inorganic glass-forming (GF) materials. Despite the many regularities in the dynamical properties of GF materials, the structural origin of the universal dynamical properties of these materials has not yet been identified. In the current thesis, we employ the methodologies for characterization of dynamics in numerous GF liquids to study the 'dynamic heterogeneity' (DH) in model metallic glass systems under three scenarios. In particular, we investigate the dynamics within the mobile interfacial layer of secondary prismatic plane $(11\bar{2}0)$ of hexagonal ice, metallic GF liquids, and deformed metallic glasses by molecular dynamics simulation and test the metrology drawn from the field of glass-forming liquids. Relaxation mode is examined above and below glass-transition temperatures. Firstly, the width ξ of the mobile interfacial layer varies from a monolayer to a few nm as the temperature is increased towards the melting temperature T_m in the study of interfacial dynamics in hexagonal ice. The dynamics within this mobile interfacial layer prove to be "dynamically heterogeneous" in a fashion that has many features in common with glass-forming liquids over a reduced temperature range, $2/3 < T / T_m < 1$. We also find that the common non-Gaussian diffusive transport, decoupling between mass diffusion and structural relaxation, and stretched exponential relaxation. String-like cooperative motion is identified within the mobile layer, confirming that the mobile layer evidently shares many common features with GF liquids. Then, we extend the study on dynamic heterogeneity arising in the coarse-grained polymeric GF liquids to metallic GF liquids with vastly different molecular structure and chemistry (i.e., Cu-Zr, Ni-Nb and Pd-Si). By identifying the lifetimes of mobile and immobile clusters, we confirm the ‘universality’ of DH phenomenon. While the mobile clusters arise from molecular diffusion, the immobile clusters are dominated by α-relaxation. Finally, we examine the relaxation mode in the low-temperature regime. Model metallic glasses Cu-Zr systems with different thicknesses under different temperatures are investigated. We observe that the applied stress acts as excitation instead of diffusion to particles and makes them ‘mobile’, and these ‘mobile’ particles form the soft spots initiating the formation of shear band (SB) region. The ‘Debye-Waller factor’ provides a useful method for estimating the shear modulus of the entire material and, by extension, the material stiffness at an atomic value. This metrology further proves that that SB formation indeed occurs through the strain-induced formation of localized soft regions that percolate within the SBs in our deformed metallic glass with free surfaces. The current thesis work clearly provides us a better understanding of the nature of universal relaxation from a dynamic heterogeneity perspective.

Preface

This dissertation is submitted for the degree of Doctor of Philosophy at the University of Alberta. The research conducted for this thesis is a part of an international research collaboration, led by Dr. Hao Zhang at the University of Alberta, Dr. Jack Douglas from National Institute of Standards and Technology, and Dr. Wen-sheng Xu from Changchun Institute of Applied Chemistry. Chapter 3 of this thesis has been published as X. Wang, X. Tong, H. Zhang, and J. F. Douglas, “String-like collective motion and diffusion in the interfacial region of ice,” *J. Chem. Phys.*, vol. 147, no. 19, p. 194508, 2017. Chapter 4 of this thesis has been published as X. Wang, W.-S. Xu, H. Zhang, and J. F. Douglas, “Universal nature of dynamic heterogeneity in glass-forming liquids: A comparative study of metallic and polymeric glass-forming liquids,” *J. Chem. Phys.*, vol. 151, no. 18, p. 184503, 2019. Chapter 5 of this thesis has been published as X. Wang, H. Zhang, and J. F. Douglas, “The Initiation of Shear Band Formation in Deformed Metallic Glasses from Soft Localized Domains” *J. Chem. Phys.*, vol. 155, no. 20, p. 204504, 2021. In all the above publications, I was responsible for data collection and analysis as well as manuscript preparation. Dr. Hao Zhang contributed to the manuscript composition and Dr. Jack Douglas contributed to the revision.

Acknowledgements

I would like to express my deep and sincere appreciation to my supervisor Dr. Hao Zhang for his guidance and encouragement for my study and my future career path. During my study at the University of Alberta, Dr. Hao Zhang has shown extraordinary tolerance and patience. It was a great privilege and honour to work and study under his guidance. Besides my supervisor, I would like to thank the rest of my committee, Dr. Hongbo Zeng, Dr. Phillip Choi, Dr. Chuang Deng, and Dr. Zhehui Jin for their insightful comments.

I am grateful to the professors whose courses I have taken. Dr. Hongbo Zeng, Dr. Phillip Choi, Dr. Gabriel Hanna, Dr. Kamyar Davoudi, and Dr. Mohammad Khalkhali have influenced me with their profound knowledge in their expert areas. I appreciate the help from the group members, Mr. Gazi Mahmud and Mr. Muziyuan Gao. The discussion has been effective and helpful. I am grateful for the unconditional support from my family, my parents Xiaoqi Wang, Jun Gao, and my sister Luoyi Su. Every time I encountered any difficulties in life, they have led me back to the right path. My special thanks go to Yuxin Cao for his patience and encouragement. I would also extend my thanks to all of my friends. They have all been there for me during this tough time.

Table of Contents

List of Tables

List of Figures

1. Introduction

1.1 Relaxation processes in Glass-forming liquids

Glass-formation has been identified in a broad class of materials ranging from biological materials and synthetic polymers to metallic and other inorganic GF materials, a phenomenon that has been intensively studied, which is concretized as the slowing down of dynamics at temperatures near 2/3 of the melting temperature. A significant number of GF materials exist in nature and human-made materials. At low temperatures, this wide variety of materials exhibits tendency to form medium or short-range structural order, but still shows similar or enhanced mechanical properties as solid.

Take metallic glasses (MG) as an example, MGs are metallic alloys with amorphous structure. The main method for synthetization is quenching the high-temperature metallic melts to room temperature with a high cooling rate, thus the liquid structures are “frozen” before metals have the chance to crystallize. [1,2] The existence of the amorphous structure prompts that MGs do not have crystalline defects such as vacancies, dislocations, and grain boundaries. The lack of translational long-range order provides unusual structural properties and non-traditional deformation mechanisms; it also empowers this special kind of materials with superior high strength, large ductility, high hardness, and high resistance to corrosion compared with their crystalline counterparts.

Another example of GF liquids would be most of the water appearing in the universe. Amorphous water ice is found as interstellar ice in the dense molecular clouds using spectroscopic. [3] The formation of this unusual structured ice is caused by the low-pressure vapour deposition. [3] Also the amorphous silica, the result of volcanic activity, constitutes the earth crust. [4] A prerequisite in generating the amorphous structure in GF liquids is that crystallization is depressed, and normally achieved by applying a relatively high cooling rate to prevent nucleation in the systems. Normally viscosity η shows an exponential increase with decreasing temperature T, which could be described using the Arrhenius equation: $\eta = \eta_0 \exp\,(W/kT)$. As expected, if the material follows the Arrhenius temperature dependence, a linear relationship should be observed between $\log(\eta)$ and $\log(1/T)$. However GF liquids does not follow the rule as shown in Figure 1.1, and exhibit deviation from the behavior of SiO_2 which is known to show near-Arrhenius behavior. [5]

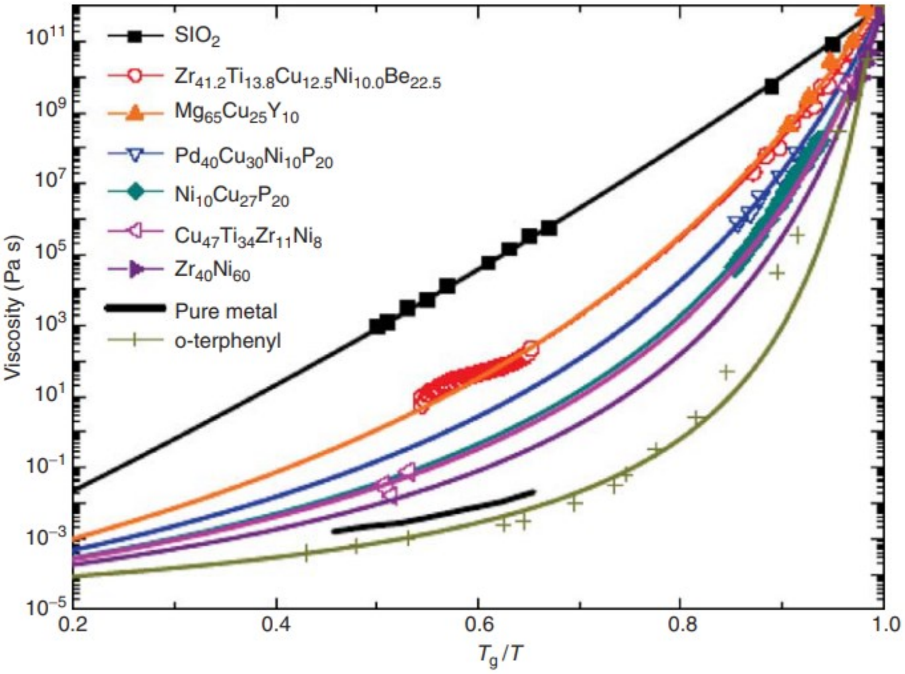

Figure 1.1 Relationship between T and h in a wide range of GF liquids. [5]

Relaxation in GF liquids happens in a hierarchical order, involving separate relaxation processes in the timescales and length scales. These relaxation processes both have different influences on the observable properties of this broad class of materials. The character of these processes is found to be greatly dependent on the T. To be more specific, at elevated T, only structural relaxation process exists while the properties of the fluid show Arrhenius relaxation. In this 'homogenous' liquid regime at elevated T, the shear viscosity η of the liquid behaves consistently as simple liquid, also the Stokes-Einstein relation $D = k_B T/6\pi\eta r$ between D and viscosity η still holds.

At T lower than onset temperature T_A the relaxation has switched to non-Arrhenius mode. Relaxation time τ_α and viscosity η may undergo dramatic change by more than 15 orders of magnitude in the range of T below T_A. And further, a primary relaxation process called α-relaxation has raised, ranging from ps to even minutes. On a much shorter timescale of ps, an initial relaxation process has occurred in the glass-forming liquids and very small molecules like water, identified as 'β-relaxation' or 'fast' relaxation process. [6] As shown in Figure 1.2, the two-point density correlation function indicates that glass-forming liquids typically exhibit a multi-stage hierarchical process. The α-relaxation clearly shows retardation as temperature decreases, also the short time β-relaxation has emerged. There is a growing consensus that α-relaxation is associated with cooperative motion and has unprecedented significance in understanding the many properties of the materials. Much of the modeling of GF liquids has focused on the α-relaxation since its associated relaxation time τ_α is important in explaining challenges in diverse practical applications.[7–11] However, β-relaxation in glass-state has drawn increasing attention because of its short time scales. Particularly, it is widely accepted that the 'anomalous' temperature dependence of thermal conductivity, specific heat and some low temperature-dependent properties in the GF liquids could be attributed to β-relaxation. [6,12–15] The relaxation time τ_α of α-relaxation has been identified as the primary relaxation process of GF liquids in the fluid state. However, when T id below the glass transition time T_g τ_α usually comes to several minutes and the dynamics will slow down. [16] Since it is not feasible or simulation-wise to study the α-relaxation process in the glass state, the fast relaxation process has become preeminently important in understanding the performance of glass materials for many practical applications. The urgent need for comprehending the molecular origin of β-relaxation has become both theoretical and technological concern.

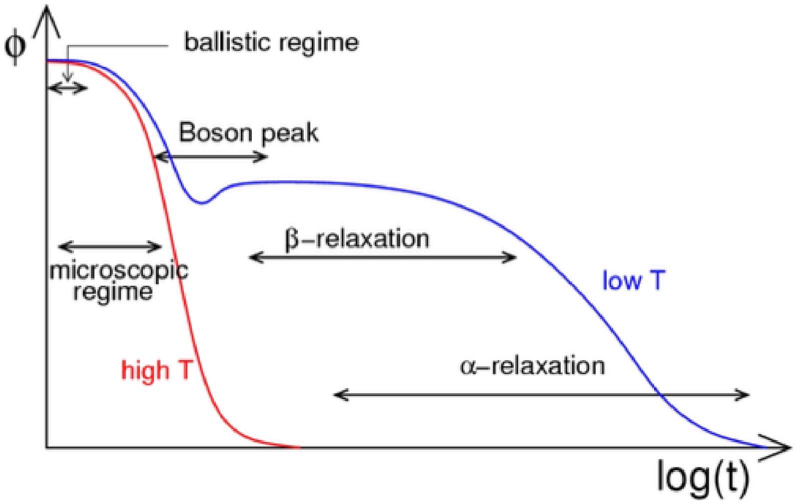

Figure 1.2 Sketch of two-point density correlation function Q as a function of time t for a binary glass-forming liquids. [17]

Many molecular dynamics simulations [18,19] and experimental studies [20,21] have proposed that β-relaxation is closely related to collective atomic motion which takes place on a ps time scale and in form of particles undergoing string-like displacements over a broad class of GF liquids. Betancourt et al. have examined the atomic motion related to α- and β-relaxation in a coarse-grained polymer melt. Since relaxation occurs in a multi-stage hierarchical order, strings have been acted as excitation in different regimes. However, the variation of string length with temperature is reversed in these processes. At first, the inertia motion of the particles dominates β-relaxation, and fast "stringlet" collective motion has been suppressed as temperature decreased. Then the string-like cooperative motion governed by diffusion has raised and mediated the relaxation approaching glass-transition. [6] Near T_A characteristic timescales of α- and β-relaxation, τ_α and τ_β become equal. Then upon cooling the increase of molecular caging inhibits the collective motion at short times. Particles are confined in the cage formed by surrounding particles, leading to the large-scale collective motion, string-like cooperative motion, is desired to mediate the structural relaxation. A relationship between strings and stringlets corresponding to a connection between α- and β-relaxation has been established. [6,22]

In the low-T regime (below T_g), relaxation and mobility are ceaselessly changing, and it is not rational to simply extrapolate the dynamical properties from the T regime above T_g. Rather, a new relaxation process has emerged identified as Johari-Goldstein (JG-β) or "slow-β" relaxation process. This process can not be directly confirmed using intermediate scattering function, [6] however it has dominated the diffusion and other material properties in the glass state. JG-β relaxation has replaced α-relaxation in the glass regime as the primary relaxation process concerning the material properties. Naturally, the engineering community has put much effort in understanding this fundamentally significant process in metallic, polymeric and other GF liquids to interpret the basic engineering properties like toughness, hardness, and impact resistance.[23,24] Recent simulation results have shown that fast β-relaxation is corresponding to the highly mobile atomic movements which follow Arrhenius temperature dependence and exhibit exponential decay in the correlations. And α-relaxation is identified with major structural rearrangements and shows highly non-Arrhenius behavior. Stretched exponential decay could well capture the time dependence of α-relaxation. [25–27]

1.2 Dynamic heterogeneity

Based on the extensive simulation studies on the GF liquids, we can conclude that the slowing down of the dynamics and the accompanying increase in the activation energy for relaxation and diffusion often correlates with the growth in DH which can be defined by the spatially divided regions involving particles with relatively high and low mobility. The observed change in mobility is the comparative of the Brownian motion of particles. The geometrical form of heterogeneities has shown a lack of sensitivity to the different kinds of compositions, remarkably similar to the performance of DH in the metallic glasses [28] and polymeric GF liquids [29]. This universal feature shared between metallic glasses and polymeric GF liquids is the result of the morphological similarity. A variety of systems besides metallic glasses and polymeric GF liquids have displayed this kind of DH in the form of spatial correlations shown in Figure 1.3. Here, clusters or particles with relatively high and low mobility have emerged in different systems, although the mobility is probed using different methods. Also, it reveals that particles with similar mobility tend to aggregate rather than appear randomly throughout the system, suggesting that structural relaxation in GF liquids is a fluctuated dynamical process. Therefore, we could classify the particles in the systems into mobile and immobile clusters over an intermediate timescale.

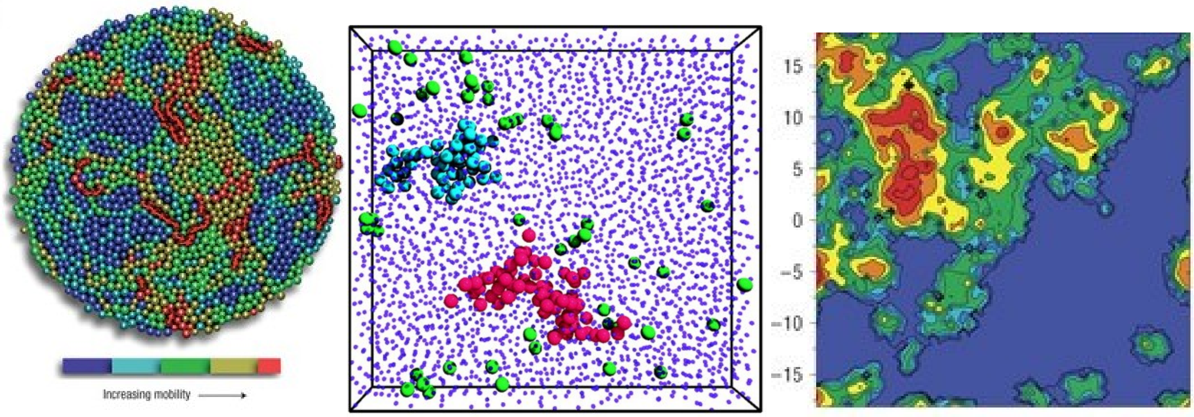

Figure 1.3 The examples of dynamical heterogeneity in granular matter [30], colloidal hard spheres [31], repulsive disks [31].

1.3 Characterization of Dynamical Heterogeneity

After the discussion on the dynamic heterogeneity, the underlying question is what method could be used to characterize this phenomenon. Experimentally, the existence of DH can be observed using different techniques. Gokhale et. al have utilized video microscopy and holographic optical tweezers to show that 'Dynamical Facilitation' in colloidal GF forming liquids increases with the density inclusive of the fraction of pinned particles. [32] Some well-established theories like free-volume [33] and mode-coupling [34,35] which treated the liquid as homogeneous would not be adequate to explain this heterogeneity. Theoretically, Adam and Gibbs have proposed specific dynamic structures called "cooperatively rearranging regions" (CRRs) in 1965. [36] They proposed that the increase in the relaxation time and dramatic dropping in the diffusion rate could attribute to the increment of these hypothetical clusters. Postulation of the direct proportional relation between the activation energy ΔG_a and the product of the number of particles in the proposed clusters and the activation free energy $\Delta\mu_a$ under the condition of high temperature and Arrhenius behaviour was purported which could be expressed as $\Delta G_a(T) = z(t)\Delta\mu_a$. To correlate the theoretical hypothesis with the experiments, they further speculate that $z(t)$ exhibits inversely scaling with the configurational entropy S_c of the GF liquids. The abstract of AG's theory is that as T decreases the number of accessible configurational states rapidly drops. Then diffusion and relaxation have to happen through the collective motion of CRRs, and this correlated excitation results in an increase of the activation energy of transport. [28,36] The random first-order transition (RFOT) theory [37–39] is proposed on the basis of the same concept to explain the slow down of dynamics upon cooling, which states that the growth in the size of these cooperatively dynamic clusters holds account for the increase in the activation energy of diffusion and structural relaxation. However, AG and RFOT theories both provide only conceptual understanding and little information on the definition or algorithm for the CRRs.

Recent computational works have attempted to understand DH founded on the fundamental concepts of CRRs by modeling the string-like cooperative clusters as a form of equilibrium polymerization. [29,40] The string model (SM) has been developed to quantitively describe the relaxation process in the polymeric GF liquids at different temperatures. [29] This theory has been tested over a large range of polymeric GF liquids including thin polymer films with various thicknesses, substrate roughness, and substrate rigidity also polymer nanocomposites with different compositions and concentrations and have shown great coherency with the SM. [41,42] The SM theory has been tested on metallic GF liquids to further support its universality in describing the DH in the wide range of GF liquids. [28] In Figure 1.4, a typical string-like cooperative motion in the metallic GF liquids has been shown geometrically. The direction of the movement was identified using arrows. Zhang et al. [28] have investigated Cu- Zr metallic GF liquids over a wide range of temperatures and compositions with a focus on the mobile particles inside the system. With the tools derived from polymeric GF liquids, the dynamic of metallic GF liquids can be described by DH in the terms of clusters undergoing collective motion. Strings exhibit a dynamical appearance and disappearance within the string lifetime t^* in the system. There is no certainty that particular atom will always participate in the string-like cooperative motion. At this moment, one particular atom could be mobile, it might be immobile at next time interval. String length L confirms to be a good approximation to the changes in the diffusion coefficients and relaxation time. There exists a dynamic equilibrium between localized ('solid-like') and wandering ('liquid-like') particles then the dynamic heterogeneity could be treated as a type of self-assemble process. [43]

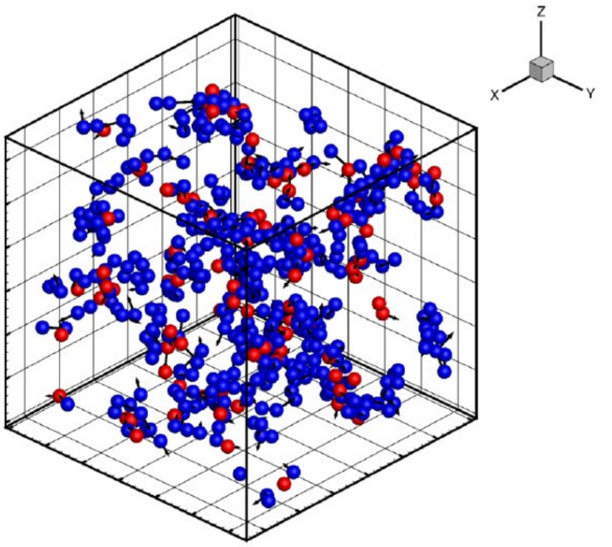

Figure 1.4 Typical string-like cooperative motion in $Cu_{64}Zr_{36}$ at $T = 1000$ K. [28]

Hypothetically, Grain boundaries (GBs) in the polycrystalline caused by adjacent grains with different orientations should have shared common features with GF liquids, since GBs exhibit medium-range order similar to GF liquids. [44,45] It leads to the suspicion that similarity in the dynamics should be observed in both systems. GBs have been observed to be ordered and relatively immobile at low T, however, an increase in T has ignited the region and resulted in high mobility and structural disorder. The nonlinear relationship has been observed in the Arrhenius plot of GBs which is the most common feature in the GF liquids. [45] Zhang et al. have observed similar string-like cooperation motion inside the grain boundaries. Previous findings in GF liquids have shown that the average string length n and the effective activation energy for structural relaxation grow as T decreases. [46,47] Similar correlation still holds in GBs, even the magnitude and distribution of string length are practically the same in both materials. [45] Besides GBs, the string-like cooperative motion has been observed in other non-typical GF liquids like interfacial dynamics of Ni nanoparticles, melting and freezing of nanoparticles, and the interfacial dynamics of crystalline Ni. [48–50] Especially in crystalline materials, many of the important properties such as mechanical properties, catalytic behaviour, is essentially determined or deeply influenced by the dynamics and thermodynamics of their interfacial regions. At elevated temperatures, researchers find that the dynamics inside the region behave similarly to the GF liquids. The collective atomic dynamics exhibiting in the interfacial region of crystalline Ni are strongly consistent with the findings in GF liquids. Zhang et al. show that the noise component α of $\langle u^2 \rangle$ is directly related to the average string length L, the extent of string-like collective motion, by a simple equation $\alpha = L - 1$. [48]

Another commonly used analysis measure utilized in the characterization of DH would be non-Gaussian parameter, α_2, which is defined to be zero when the particle is moving as

Brownian particles. An inverse proportional relation has been discovered between D/T where D is the diffusion constant and t^* the peak time of α_2 confirming that t^* is a characteristic timescale to represent mass diffusion in GF liquids and other non-typical GF liquids. All the investigation done on these strongly interactive particle systems has developed a similar trend that the lifetime of the mobile clusters exhibiting the string-like cooperative motion is controlled by the mass diffusion relaxation time, t^*. Schober and coworkers have studied relaxation in a soft-sphered glass and accentuated that the existence of string-like motion on the timescale of picoseconds indicating the onset of atomic caging could have great influence on studying the intrinsic properties of GF liquids. [51,52]

Since correlation between mobile atoms, string-like cooperative motion and mass diffusion has been established, the question falls on which timescale could correlate with momentum diffusion i.e., shear viscosity. We have noticed that the structural relaxation time τ_α, a characteristic time developed from the intermediate scattering function has been frequently affiliated with the momentum diffusion. [53] Based on the Maxwell scaling relation $\eta = G_\infty \tau_s$, we can conclude that the shear viscosity and high frequency shear modulus G_∞ and the shear stress relaxation time τ_s are highly correlated. Then the expectation of the structural relaxation time τ_α to vary with T like η has been confirmed in many simulation studies on metallic GF liquids [28], supercooled water [54], polymer [55]. A "decoupling exponent" ξ has been identified to describe this decoupling phenomenon between the characteristic timescales of structural relaxation and diffusion $t^* \sim (\tau_\alpha)^{1-\xi}$ which could quantify the breakdown of the Stokes-Einstein relation.[28,54] Starr et al. then have identified that the time scale of highly mobile particles correlates with the string-like motion, while the time scale of particles with low mobility is associated with the structural relaxation time. These two distinct dynamical clusters and different characteristic timescales have perfectly explained the decoupling phenomenon between structural relaxation time and diffusion. [55]

1.4 Objectives of this study

The intensive research work mentioned above indicates that DH is a universal feature in the GF liquids. Much simulation research on polymeric GF liquids has tried to develop a universal measure on characterizing DH. It is not yet clear whether supercooled interfacial layer of water exhibits dynamical heterogeneity sharing common features with GF liquids. We have investigated the collective motion of water molecules in the mobile interfacial layer over a wide range of Ts. The analysis tools drawn from polymeric GF liquids have been utilized to confirm the universality of the DH phenomenon in different metallic GF liquids i.e., Cu-Zr, Ni-Nb, and Pd-Si alloys. The structural origin of this universal phenomenon has been examined by identifying the clusters with dramatically different mobilities. As the third part of the study, simulation was performed in comparable size scales and T well below T_g to provide insight into the initiation of shear band (SB) formation in deformed metallic glasses which could help understand the atomic mechanism of shear banding and lead to a solution to overcome the limited application of metallic glasses.

2. Simulation methodology

Molecular dynamics simulation has been employed to study atomic-level process, which is not feasible nor efficient with experiments. Before the emergence of MD simulation, researchers often use direct observations or analytical machines to obtain insight on different matters. With great effort made in the computational power and theoretical studies, MD simulations have been empowered to simulate the phenomena that are can hardly be characterized by experiments. Especially in the field of simulating metallic glasses, with the high requirements on the experimental level and lack of understanding on the atomic level applications of MGs have been limited. MD simulations could provide in-depth insights on the atomic trajectory, atomic stress, and structural information which are not acquirable in the experiments.

2.1 Equations of motion

The classic molecular dynamics method is established on Newton's second law:

$$F_i = m_i a_i \qquad 2.1$$

where F_i, m_i, and a_i are the force, mass, and acceleration of atom i. When the force on each atom in the system is known and initial positions and velocities of each atom are assigned, then it is feasible to determine the acceleration of each atom a_i.

$$a_i = \frac{dv_i}{dt_i} = \frac{d^2 r_i}{dt^2} \qquad 2.2$$

where v_i is the velocity of atom i and can be computed by calculating the second derivative of displacement of atom i with respect to time. The acting force F_i can be expressed as the derivation from the interatomic potential energy $V(r_i)$:

$$F_i = -\nabla V(r_i) \tag{2.3}$$

Combining equation 2.1, 2.2 and 2.3, then we have

$$-\frac{dV(r_i)}{dr_i} = m_i \frac{d^2 r_i}{dt^2} \tag{2.4}$$

In statistic mechanics, Hamiltonian, **H**, is employed to describe a microstate in the whole system, which can be illustrated by the sum of kinetic energy K and potential energy U. Both energies can be expressed using functions of Cartesian momentum and coordinates of each microstate.

$$\boldsymbol{H} = K(p) + U(r) = \sum \frac{|P_i|^2}{2m_i} + U(r^N) \tag{2.5}$$

where P_i is the momentum of atom i. Through derivation on the Hamiltonian's equation, we can obtain the force acting on each atom and velocity of each atom shown as follow:

$$-\frac{\partial H(r,p)}{\partial r_i} = \frac{dp_i}{dt} = F_i \tag{2.6}$$

$$-\frac{\partial H(r,p)}{\partial p_i} = \frac{dr_i}{dt} = \frac{p_i}{m_i} \tag{2.7}$$

The integration of Hamiltonian's equations of motion has been performed each step of the MD simulation to acquire the updated positions and velocities of the particles in the system. Then the trajectory of each atom has been stored. A schematic of MD simulation is shown in Figure 2.1.

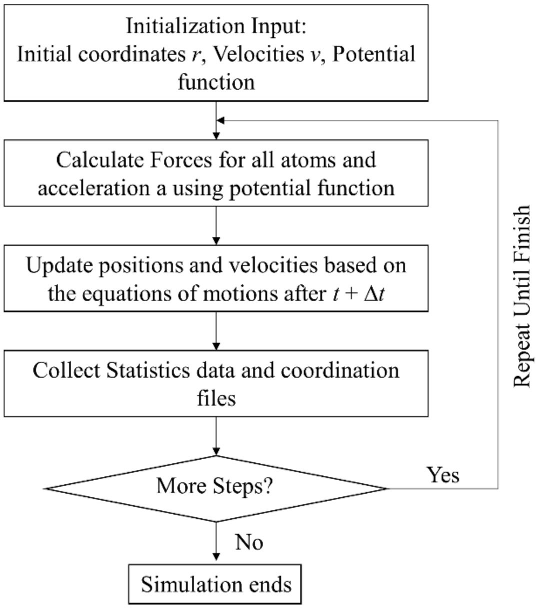

Figure 2.1 Schematic of MD simulation

In the MD simulation, one of the key parts is the numerical algorithms of the equations of motions. The accuracy and simulation time are highly relied on the choice of the algorithm. The Velocity Verlet algorithm [56] was developed to overcome the limitations of the Verlet algorithm [57] and obtain higher accuracy. The velocity v_i is calculated at mid-step:

$$v\left(t+\frac{\delta t}{2}\right)=v(t)+\frac{1}{2}a(t)\delta t \qquad 2.8$$

The positions r_i are then computed using the new v_i

$$r(t+\delta t)=r(t)+v(t+\frac{\delta t}{2})\delta t \qquad 2.9$$

In this form, the velocities v_i are calculated at mid-step using the force and velocity from step t. Then it is sufficient to allow the calculation of the atom positions at $t+\delta t$. Using the Velocity Verlet algorithm will require less usage of computer memory.

2.2 Potentials

Potential energy surfaces are required to be constructed before molecular simulation. Potential is a function $v(r_1 \cdots r_i \cdots r_N)$ of the positions of the nuclei, served as potential energy surface of metallic glasses when the atoms are arranged in a specific configuration. The Embedded Atom Method (EAM) [58] has incorporated many-body interactions unlike pairwise interaction considered only two-body approximations. EAM can guarantee quantitative agreement with experimental data although more time and memory are required. Another appealing reason for using EAM is its physical picture of metallic bonding. Each particle is constrained in a host electron gas created by the surrounding particles, which is intrinsically more complex than the simple pair-wise model. Particularly, EAM empowers a simple way to establish how coordination influences the bonding inside the system, and naturally leads to a distinguishment between bulk and surface bonds. [59]

The total potential energy is represented by the following equation:

$$U = \sum_{i=1}^{N-1} \sum_{j=i+1}^{N} \varphi^{\alpha_i \alpha_j}\left(r_{ij}\right) + \sum_{i=1}^{N} \Phi^{\alpha_i}(\rho_i) \qquad 2.10$$

In the above equation, i and j represent different atoms; N is the total number of atoms in the system; r_{ij} is the distance between atoms i and j; α_i is the element type of atom i; ρ_i is the background charge density, which is expressed by:

$$\rho_i = \sum_j \psi^{\alpha_i \alpha_j}\left(r_{ij}\right) \qquad 2.11$$

Total potential energy consists of two components: a pairwise and a local density part. The functions are determined by taking the sublimation energy, equilibrium lattice constant, elastic constants, and vacancy-formation energies into consideration.

2.3 Ensembles

In statistical mechanics, all the possible microstates like coordination and momentum of the particle will be the subject of interest. The behaviour of all the possible microstates could eventually represent the change in the macroscopic properties for instance temperature *T*, pressure *P* and volume *V*. An ensemble refers to a collection of microstates that could possibly exist in the system. According to the ergodic hypothesis, the correlation between MD simulation and experiments can be established, since we could consider the systems are consisted of many replicas, each replica could be considered as ensemble. Over a long period of time, the time average of the observed properties could be considered as ensemble average. To make the connection between simulation and experiments, sufficient time for the microstates to fulfill the quasi-ergodic theorem is necessary.

Different statistical ensembles have been generated based on different thermodynamic parameters. We have listed four kinds of ensembles in Figure 2.2. A microcanonical ensemble NVE is considered as an isolated system, Number of particles, N, volume of the system, V, and the total energy, E are conserved. The system and surroundings are completely cut off. A canonical ensemble NVT represents fixed number of particles and volume. The system could exchange energy through heat with a heat reservoir to keep temperature fixed, but there will be no work done by the system on the reservoir or vice versa. In isothermal-isobaric ensemble NPT, pressure could be controlled by changing the volume of the system, and temperature is being fixed the same way as it is in the NVT ensemble. In the grand canonical ensemble μVT, since the number of the particles is not fixed then the chemical potential could be controlled through exchanging particles with the surroundings.

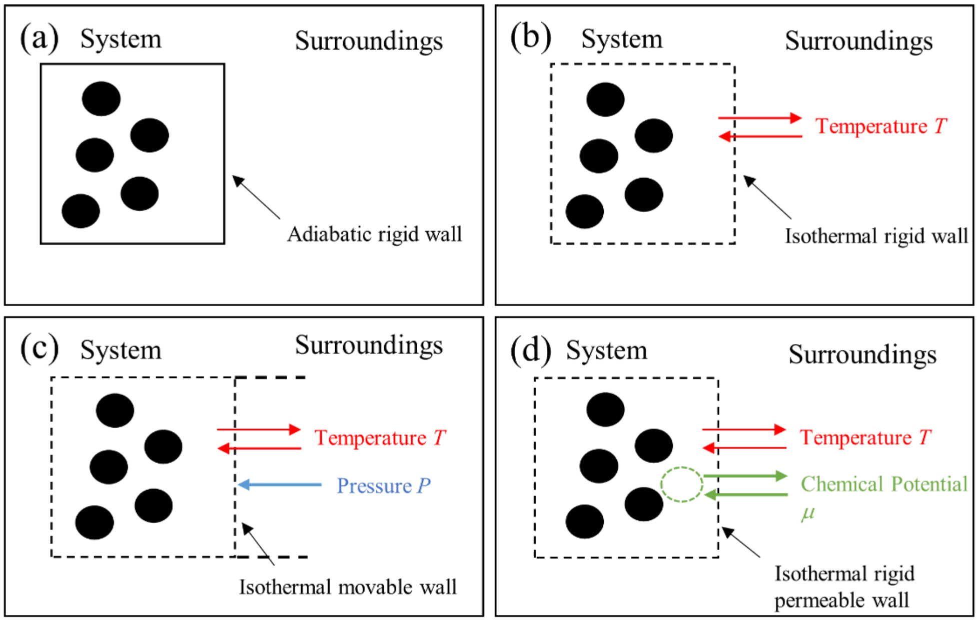

Figure 2.2 Schematic illustrations of different ensembles (a) microcanonical ensemble NVE, (b) canonical ensemble NVT, (c) isothermal-isobaric ensemble NPT, and (d) grand canonical ensemble μVT.

2.4 Periodic boundary conditions

Considering the rational utilization of the computing power, the whole system simulation is unnecessary and infeasible. An area of interest in the whole system is chosen prior to the simulation. The finite size of the unit cell will cause boundary effects and lead to uncertainty in connecting the simulation with macroscopic sample. Usually, when the goal of the simulation is to study bulk properties, periodic boundary conditions (PBC) will help to overcome the limitations on the number of atoms in each simulation cells. In Figure 2.3 a representation of PBC is shown. In PBC presented systems, the primary unit call is replicated in all simulation directions shown as image cells. All the image cells share the same number, positions, and momentum of particles. When the atom in the primary unit cell moves, the corresponding atom in the image cell will move in the same manner. Once the atom leaves the cell from one end, it will re-enter the cell from the other end. Also, the atoms could interact across the boundary since PBC has minimized the surface effect [60]. For the study of the surface properties, vacuum spaces will be added to the surface of interest.

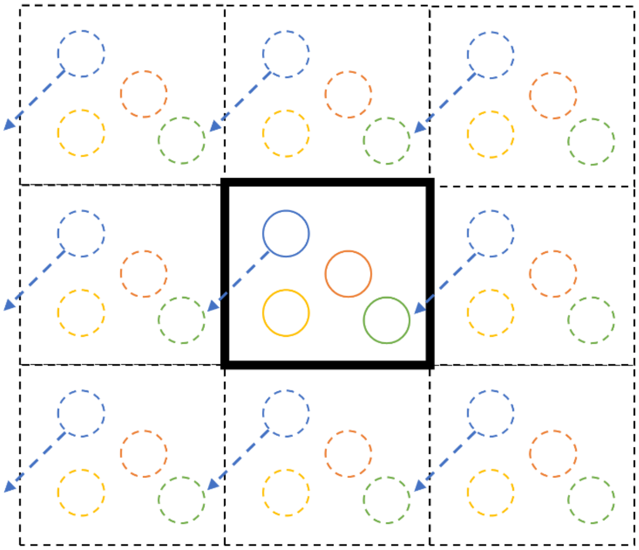

Figure 2.3 Periodic boundary condition (PBC) represented in two dimensions (2D).

2.5 Temperature and pressure control

2.5.1 Temperature Control

Isothermal-isobaric NPT ensemble is mostly used in the study. Temperature is controlled by Nose-Hoover thermostat. The general idea of the Nose-Hoover method [61,62] is to consider the heat reservoir as an integral part of the whole system with an additional fictitious coordinate.

$$H_{Nose-Hoover} = \sum_{i=1}^{N} \frac{P_i^2}{2m_i} + U(R) + \frac{\zeta^2 Q}{2} + (3N)\frac{\ln s}{\beta} \qquad 2.12$$

The last two terms in the above equation are correlated with the external hear reservoir. ζ represents the friction coefficient. By connecting the system with an external hear reservoir the time evolution of the positions and momenta needs to be updated.

$$a = \frac{dv_i}{dt} = -\frac{1}{m_i}\frac{\partial U(R)}{\partial r_i} - \zeta v_i \qquad 2.13$$

$$\frac{d\zeta}{dt} = \left(\sum m_i |v_i|^2 - 3Nk_B T\right)/Q \qquad 2.14$$

The choice of the heat reservoir mass Q influences the coupling between the system and the external heat reservoir.

2.5.2 Pressure Control

The pressure is controlled by the Parrinello-Rahman algorith [63], an extension method of Anderson [64]. Initially, Anderson barostat only allows the simulation cell to scale the volume. We could consider Andersen barostat as an extended system method by connecting the system to an external variable. This coupling system simulate the action of piston on a real system. [64,65] By applying Parrinello-Rahman barostat, the simulation box is allowed to change shape and size.

The simulation cell is allowed to have an arbitrary shape. The new coordinates are rescaled as: $r_i = \mathbf{H}s_i$ where $\mathbf{H}$ is a 3×3 matrix. Then the potential and kinetic energies are rescaled with the fluctuating volume.

2.6 Data Analysis Techniques

2.6.1 Mean Squared Displacement

A representative time correlation function is the mean square displacement (MSD) which is expressed as $\langle r^2(t)\rangle = \langle (r(t) - r(0))\rangle^2$ for all atoms. At ultrashort times, the MSD and time have a quadratic dependence. This stage is the so-called "ballistic regime", because particles move ballistically with constant velocity, and have not "felt" each other. At long times, collision happens between particles. Diffusive motion appears and MSD has linear relation. Diffusion coefficient is defined at this stage. $(\Delta r(t))^2 = 6Dt$, where D is diffusion coefficient. As we can notice there is a caging regime at low temperatures. At this point, MSD is approximately constant, representing particles are trapped by the particles near them. When temperature decreases, the dynamics slows down because of the increased length of the plateau.

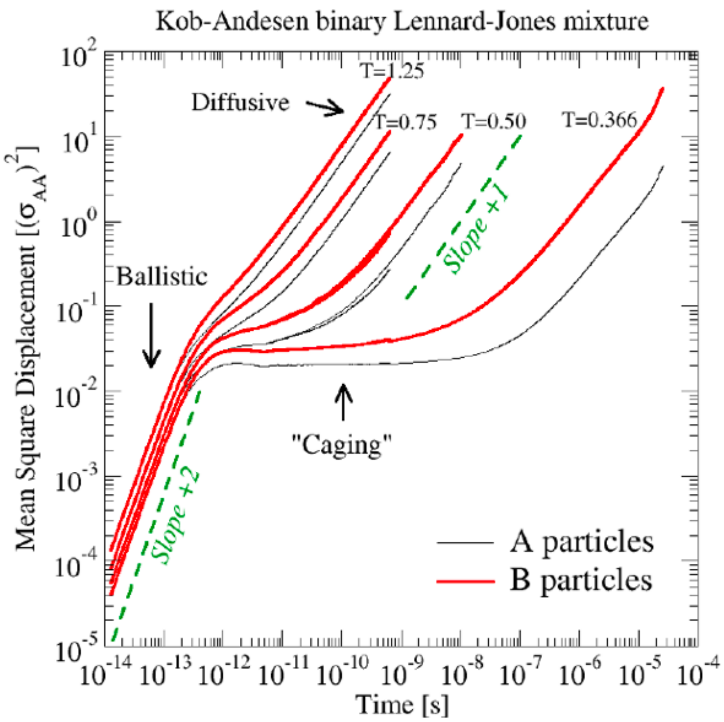

Figure 2.4 Mean square displacement of A and B particles of the Kob-Andesen binary Lennard-Jones mixture. [66]

2.6.2 van Hove Distribution

Self-part of the van Hove correlation function $G_s(r,\Delta t)$ is utilized to characterize fundamental aspects of dynamic properties, which illustrates the probability distribution of the position r of an atom after a time Δt. [67,68] It is written as:

$$G_s(r,\Delta t) = \frac{1}{N}\langle \sum_{I=1}^{N} \delta(\vec{r_i}(\Delta t) - \vec{r_i}(0) - r)\rangle \qquad 2.15$$

At small Δt, $G_s(r,\Delta t)$ has become Gaussian, indicating the existence of harmonically localized motion. From $G_s(r,\Delta t)$ at different time intervals, we can observe the path taken by atom when it moves around and quantify these motions in terms of atomic displacement. When

Δt increases, non-Gaussian behaviour is expected. The non-Gaussian parameter α_2 can be served as basic measure of dynamic heterogeneity. [69,70] It can be expressed mathematically as:

$$\alpha_2(\Delta t) = \frac{3\langle r^4(\Delta t)\rangle}{5\langle r^2(\Delta t)\rangle^2} - 1 \tag{2.16}$$

where $r(\Delta t)$ is the displacement of atom after time Δt.

By performing Fourier transformation of van Hove correlation function, self-intermediate scattering function is obtained as [68]:

$$F_s(q,t) = \langle exp\{-iq[r_i(t) - r_i(0)]\}\rangle \tag{2.17}$$

$F_s(q,t)$ can estimate the mean structural relaxation time. The dynamic structural factor $F_s(q,t)$ always exhibit a plateau stage then associated with stretched exponential behaviour. At low temperatures, a plateau stage happens at an intermediate time because of the existence of cage motion (β relaxation). Then particles leave cages and exhibit Kohlrausch (stretched exponential) behaviour. At high temperatures, the decay of correlation is notable after microscopic regime. [17]

2.6.3 Four-point Susceptibility

The observation of clusters with relatively high or low mobility has intrigued many attempts to propose a unified way to distinguish these two clusters. The emergence of the four-point correlation function has been broadly accepted as a universal tool to analyze dynamical heterogeneity. First time-dependent self-overlap function $Q_s(t)$ [71] is defined as follow:

$$Q_s(t) = \sum_{j=1}^{N} \omega\left(\left|r_j(t) - r_j(0)\right|\right) \tag{2.18}$$

the mean-squared variance of $Q_s(t)$ then defines the (self-part) of χ_4 [72]

$$\chi_{4,s} = \frac{V}{N^2}[\langle Q_s(t)^2\rangle - \langle Q_s(t)\rangle^2] \tag{2.19}$$

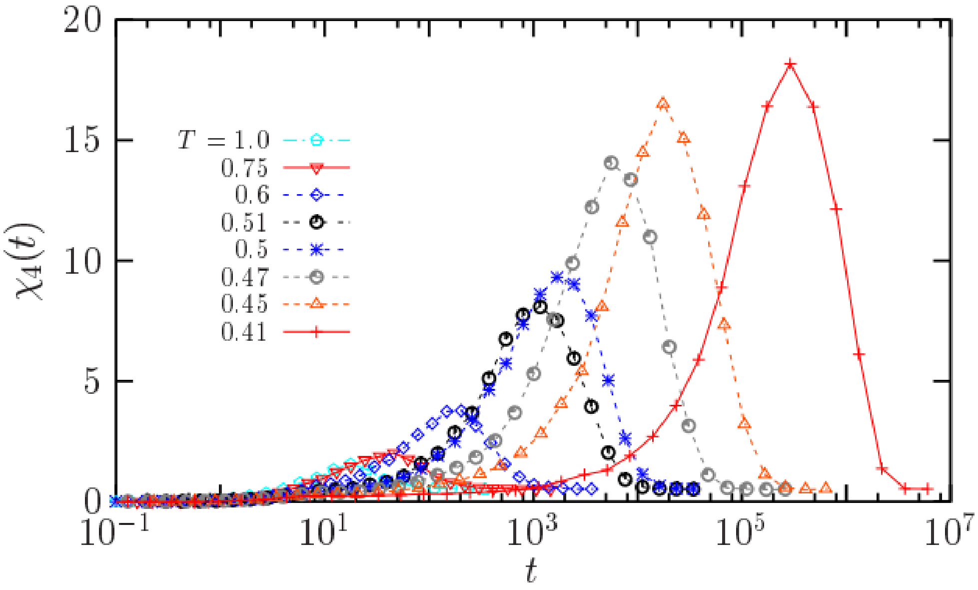

Figure 2.5 Time dependence of $\chi_4(t)$ representing the spontaneous fluctuations of the self-intermediate scattering function in a Lennard-Jones supercooled liquid. [73,74]

2.6.4 String-like cooperative motion

Dynamic heterogeneity has been identified in glass-forming liquids for quite some time. MD simulation with stored positions and velocities allowed us to characterize the cooperative motion. String-like cooperative motion implies that the spatial connection between the atoms is preserved to some degree as the atoms move.

The first step in characterizing the string-like cooperative motion is to isolate the 'mobile' particles in the system. In glass-forming liquids, the mobile particles normally refer to the particles with displacement larger than the average amplitude of atomic vibration and are defined by a threshold atomic displacement condition involving the average interatomic spacing.

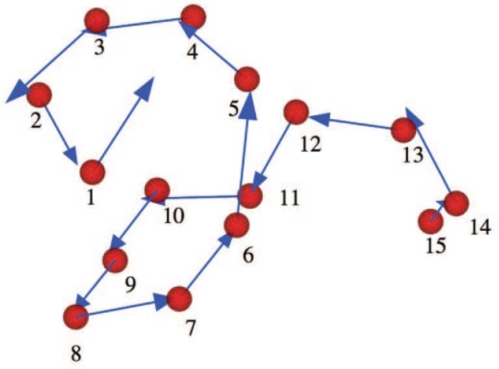

Figure 2.6 Typical string of 15 particles at T = 1840 K in homogeneous melting of Ni crystals. [50]

The mobile particles were identified by atomic displacement $a < |r_i(t^*) - r_i(0)| < b$ at t^*. $t^*$is the peak time of non-Gaussian parameter. a and b are determined from self-part of van-Hove function $G_s(r,t)$ at t^*.

$$G_s(r,\Delta t) = \frac{1}{N}\langle \sum_{i=1}^{N} \delta(r_i(\Delta t) - r_i(0) - r)\rangle \qquad 2.20$$

a is the value of the first minimum of the function.

We then define a ‘mobile particle cluster’ as the group of neighbouring particles having a separation less than 1.2 times the interatomic spacing, r_0. Explicitly, two reference mobile particles i and j, if $\min\left[\left|r_i(t^*) - r_j(0)\right|,\ \left|r_i(0) - r_j(t^*)\right|\right] < 1.2r_0$. This condition means that one mobile particle moved to another position, then the neighbouring particle has occupied its original position. Figure 2.8 shows a typical string of 15 particles. Most representative strings are free end but loops also show modest frequency.

3. String-like Collective Motion and Diffusion in the Interfacial Region of Ice

3.1 Introduction

Crystalline materials generally become “reactive” at T well below their melting temperature T_m and, in particular, Tammann suggested a widely reported empirical rule of thumb that this onset temperature for the reactivity of solid state materials should be $\approx 2/3\ T_m$. [75–77] It is natural to suppose that this onset of reactivity is associated with a change in the interfacial mobility given that this phenomenon is rather independent of the chemical nature of the material. In previous work [48], we examined this phenomenon in the interfacial dynamics of crystalline Ni where a sharp rise in atomic mobility was observed in the (110) interface of Ni at temperatures (T) near $2\ T_m / 3$ and the thickness ξ of this interfacial layer was observed to progressively increase with T up to T_m. Moreover, the dynamics within this mobile interfacial was neither like a perfect crystal or a simple liquid, but rather resembled the heterogeneous dynamics of GF liquids where atomic motion takes the form of string-like cooperative atomic exchange events and where individual particle displacement distances on a ps timescale exhibit large fluctuations reminiscent of earthquake data. Since the presence of such an interfacial layer can be expected to greatly impact the reactive, frictional and mechanical properties of crystalline materials, it is of interest to investigate the generality of this phenomenon by studying the interfacial dynamics of other substances.

We choose ice for the current study since it is a rather distinct chemistry from Ni and because the interfacial dynamics of ice is recognized to be important in a wide range of geophysical phenomena such as frost heave, the movement of glaciers, glacial motion, snow metamorphosis by grain sintering, the electrification of thunderclouds through charge and mass transfer between colliding ice particles, reactions in atmospheric ice particles influencing the ozone hole, etc. [78–82] The frictional properties of ice are also known to be greatly influenced by a mobile interfacial layer on ice below its T_m, a phenomenon relevant to the friction of tires and shoes on ice, and as well as skis, ice skates and other winter sporting equipment. Because of these many practical applications areas, the interfacial dynamics of ice has been studied in many previous experimental and computational studies, [78–81,83] allowing us to make comparison with our simulation observations.

Faraday [84,85] was apparently the first scientist to suggest that the relative low friction of ice over a wide T range below $T_m = 273$ K was due to the formation of a mobile layer at the surface of ice and he performed ingenious measurements to support the mobile interfacial layer hypothesis. In the absence of a theoretical explanation of this phenomenon, however, it took over a hundred years for these arguments and measurements to be appreciated. [78–81] Recent experimental [86,87] and computational studies [88] have confirmed that there is indeed a mobile interfacial layer near the surface of ice whose thickness grows upon approaching T_m , a phenomenon qualitatively resembling our previous observations on crystalline Ni. [48] We then examine the interfacial dynamics of ice and compare with our former simulations of interfacial dynamics of crystalline Ni. We specifically adopt a state of the art intermolecular water potential (TIP4P/2005) [89] for our simulations, and we focus our attention on the secondary prismatic plane of hexagonal ice, because its relatively loose packed nature leads us to expect that this should be the most mobile interface of ice. Correspondingly, the (110) interface of Ni is the most loosely packed low index interface of crystalline Ni, making this interface particularly suitable for comparison with our ice simulations. We note that Conde et al. [90] have recently simulated basal interface of hexagonal ice and found the onset of a mobile layer at about 0.63 T_m, a finding rather consistent both with our former interfacial Ni study and the empirical Timmerman rule for the onset of interfacial mobility. However, Conde et al. did not examine the heterogeneous dynamics and diffusion in this interfacial layer or utilize tools drawn from glass-forming liquids to quantify the dynamics of interfacial ice. We also note that Watkins et al. [91,92] and Limmer and Chandler [93] have also recently emphasized that interfacial water has many properties in common with glass-forming liquids and, correspondingly, Smit and Baker recently reported direct surface sum-frequency generation spectroscopy evidence indicating that interfacial ice contains a spectral component that is indistinguishable from supercooled water over a wide temperature range below the melting temperature. [94] However, it is not yet clear whether supercooled interfacial water on a solid substrate quantitatively resembles the pre-melted water layer in the interfacial region of ice since an active coupling between the ice underlayer and the mobile interfacial layer might lead to distinct dynamic features from a simple supercooled liquid. Below, we indeed find this to be the case.

3.2 Simulation Methodology

The intermolecular interactions of water molecules in the hexagonal ice state were described by the TIP4P/2005 water potential, [89] which is a rigid non-polarizable water model that consists of three fixed point charges and one Lennard-Jones center. The parameters in the TIP4P/2005 were optimized by fitting to six properties, i.e., the temperature of maximum density, the enthalpy of vaporization, the densities of liquid water at ambient conditions, the density of ice II at 123 K and zero pressure, the density of ice V at 223 K and 530 MPa, and, the range of temperatures at which ice III is the thermodynamically stable at a pressure of 300 MPa. [89] A previous comparative study of five related non-polarizable water models, namely TIP3P, TIP4P, TIP5P, SPC/E and TIP4P/2005, suggests that TIP4P/2005 potential model shows an overall better performance than most other non-polarizable water models. [95] In particular, TIP4P/2005 ice has a melting temperature T_m near 252 K, compared to T_m = 146 K for TIP3P water, T_m = 215 K for SPC/E water, T_m = 232 K for TIP4P water, and T_m = 274 K for TIP5P water. [96] Recent simulations of water in its liquid state using the TIP4P/2205f model [97] have shown quantitative agreement with water self-diffusion and shear viscosity data over a large temperature range (228 K to 360 K) where the heterogeneous dynamics of glass-forming liquid was exhibited over this entire T range.

Our simulation cell consists of 4,800 water molecules with a dimension of about 8 nm x 4.5 nm x 4.5 nm, oriented with crystallographic directions $[11\bar{2}0]$, $[1\bar{1}00]$ and [0001] in the X-, Y- and Z-directions. In all simulations, periodic boundary conditions were applied in Y-, and Z-directions and free boundary condition was applied in X-direction. Canonical ensemble (NVT) was employed and constant T was maintained by the Nose-Hoover method. [61,98] Molecular dynamics (MD) simulations were performed to characterize string-like collective atomic motion and self-diffusion on ice $(11\bar{2}0)$ free surface (a secondary prism face). Our MD simulations utilize the publicly available simulation package, Large-scale Atomic/Molecular Massively Parallel Simulator or LAMMPS, [99] which was developed at Sandia National Laboratories. Pfalzgraff et al. [100] provide excellent visualizations of the basal, prismatic and pyramidal facets of ice in its hexagonal form.

To characterize the interfacial dynamics of ice and the self-diffusivity D_s of interfacial atoms within the $(11\bar{2}0)$ interfacial region of hexagonal ice, we maintained our systems to fixed T values at which our isothermal simulations were performed: T = 210 K, 220 K, 250 K, 260 K, and 270 K. The "equilibrium melting temperature" T_m of 252 K was determined under the condition that ice and water co-exist. We observe that no superheating is required to melt the ice with a free surface, as observed previously. [95] At each T, simulations were conducted for at least 2 ns, and in some cases this time was extended to 20 ns. Diffusion coefficients D_s were determined from the slope of the mean-square-displacement $<r^2>$ of water molecules in the $(11\bar{2}0)$ interfacial layer versus time t. Specifically, the water self-diffusion coefficient D_s of the interfacial layer is defined by,

$$D_s \equiv (1/N) \sum_{i=1} (\langle \Delta x_i^2 \rangle + \langle \Delta y_i^2 \rangle + \langle \Delta z_i^2 \rangle) \,/\, 6\,t \qquad 3.1$$

in the limit of long times where the sum ranges all the atoms in the mobile interfacial layer. Below, we describe how the interfacial layer of ice is defined. It should be appreciated that D_s is an average diffusion coefficient describing the mobility in this layer as whole so that gradients of mobility in the interfacial layer are not considered.

Our crystalline ice material is modeled as a film having a thickness of 8 nm where periodic boundary conditions are considered in the plane of the film. We illustrate this film structure in Figure 3.1 at T = 250 K where we show an illustrative atomic configuration. The melting temperature T_m of bulk TIP4P/2005 water equals T_m = 252 K so that T = 250 K is slightly below T_m in our water model. The ice interfacial region is clearly somewhat disordered with respect to the film interior, consistent with previous computational and experimental studies. [78–81,83]

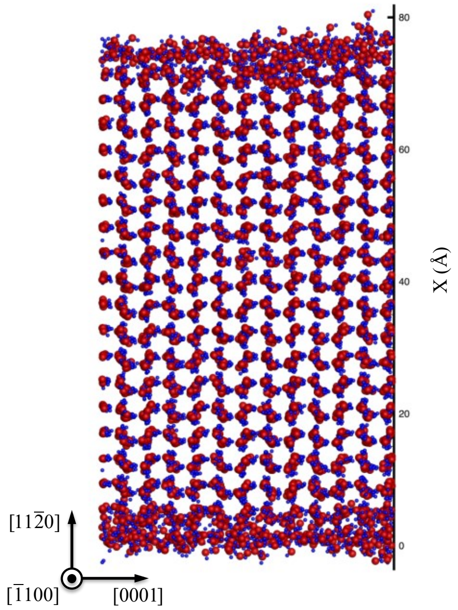

Figure 3.1 Atomic configuration of simulation cell at T = 250 K or T / T_m = 0.992 in reduced temperature units that should be more transferable to measurement. Red indicates oxygen and the blue indicates hydrogen atoms.

3.3 Results and Discussion

3.3.1 Definition of the Mobile Interfacial Layer of Ice

Following our previous discussion of the interfacial mobile layer in crystalline Ni, we define the interfacial layer of the $(11\bar{2}0)$ interface of ice by calculating the mean square displacement $<u^2>$ of the water molecules as a function of distance from the crystal surface. The thickness of the "quasi-liquid" interfacial layer is then determined between the point where the $<u^2>$ starts to deviate from the bulk value by ~ 5% and the point corresponding to the maximum value of $<u^2>$.

The Debye-Waller factor (DWF) $<u^2>$ is determined after a time on the order of 1 ps corresponding to a caging time [45] and Figure 3.2 shows $<u^2>$ as function of distance from the film surface for T = 250 K film shown in Figure 3.1. We see that the average amplitude of atomic motion $<u^2>$ near the ice surface is much larger than in the interior of the ice slab and that there is an interfacial region having a T-dependent width over which $<u^2>$ decays to within about 5 % of the nearly constant value in the center of the slab. The spatial variation of $<u^2>$ in the interfacial region can be fit to a good approximation by an exponential decay, as found in recent experimental studies on colloidal crystals [101] and in our recent study of the interfacial region of crystalline Ni. [48] The thickness of this interfacial layer ξ varies with T and we illustrate some representative $<u^2>$ profiles through the film in Figure 3.3 (a). We see that ξ grows with T, but its rate of growth is relatively small. We contrast this observation of a growing interfacial mobility length scale upon heating with a recent simulation study [102] of supercooled liquid near a neutral substrate of pinned water molecules where the interfacial mobility likewise varied nearly exponentially near the wall, but where the interfacial mobility scale increased upon cooling rather than heating so that it is then *inappropriate* to think of the interfacial mobile layer as being *equivalent* to a supercooled liquid on a non-interacting solid substrate. At the highest T simulated, about 3 K below T_m, we find $\xi \approx 2.5$ nm. An interfacial mobility length scale having this order of magnitude accords with recent computational and experimental estimates. [86,90,103] As shown in Figure 3.3 (b), a rough extrapolation of our ξ data to low T indicates that ξ becomes on the order of the diameter of a water molecule (2.75 Å) for $T \approx 165$ K, corresponding to an interfacial layer that is a molecular monolayer. Elastic Helium atom scattering measurements suggest that the onset of enhanced interfacial dynamics occurs for a comparable temperature around 180 K or $T / T_m \approx 0.66$, consistent with the Tammann onset condition for interfacial mobility. [104] We note that no direct connection can be generally made between interfacial structure, such as the gradient in the interfacial density, and interfacial mobility profile so that estimates of interfacial layer thickness from scattering measurements cannot be expected to coincide with estimates of the interfacial mobility gradient.

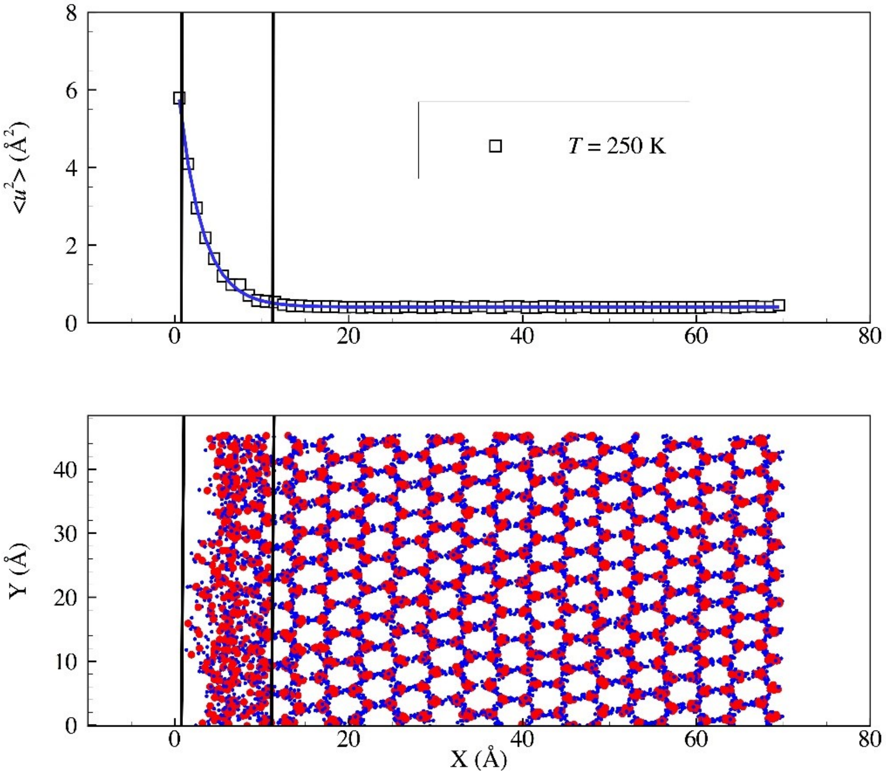

Figure 3.2 Variation of Debye-Waller factor along the normal to the $(11\bar{2}0)$ interface of ice (x-axis) at T = 250 K (above) and the corresponding atomic configuration (below). The thickness ξ of the mobile interfacial layer is determined between the position where the Debye-Waller factor starts to deviate from its bulk value and the position where $<u^2>$ exhibits its maximum value. The DWF profile along Y-axis can be well-fitted by an exponential function (blue solid line), providing another means of estimating ξ.

Estimates of the interfacial width based on thermodynamic arguments cannot then be directly compared to the interfacial mobility gradient scale. Further research is needed to better understand what factors control the width of the mobile layer of ice and other crystalline materials above the Tammann temperature.

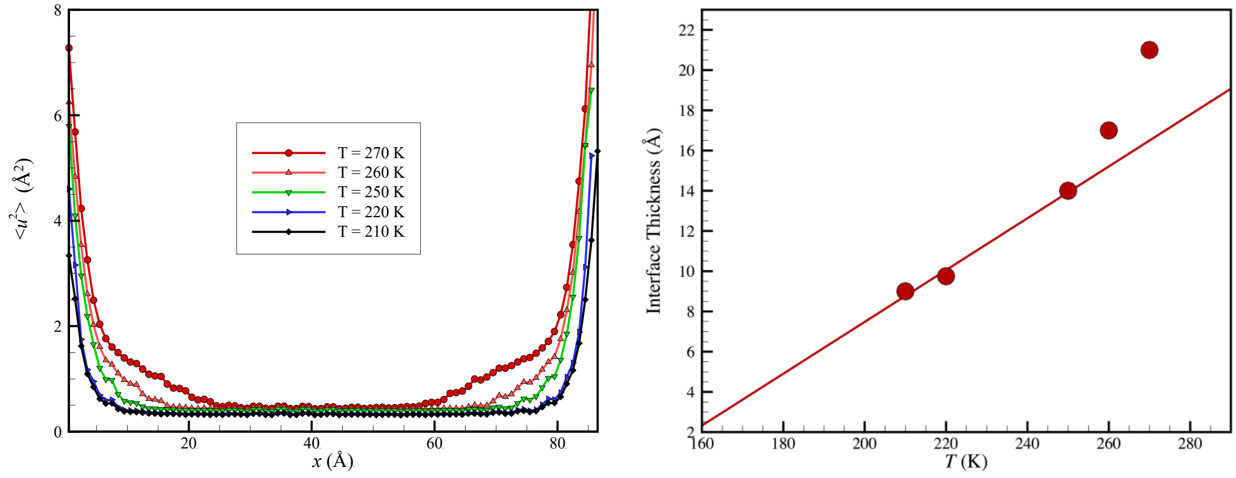

(a) (b)

Figure 3.3 (a) Variation of $\langle u^2 \rangle$ along direction normal to the $(11\bar{2}0)$ interface of ice (x-axis) for different T. (b) Interfacial width ξ of the mobile interfacial region of ice as a function of T. Extrapolating ξ for the lowest three temperatures to a scale corresponding to the molecular diameter indicates that a ξ reduces to the scale comparable to the molecular diameter of water (2.75 Å) for $T \approx 165$ K.

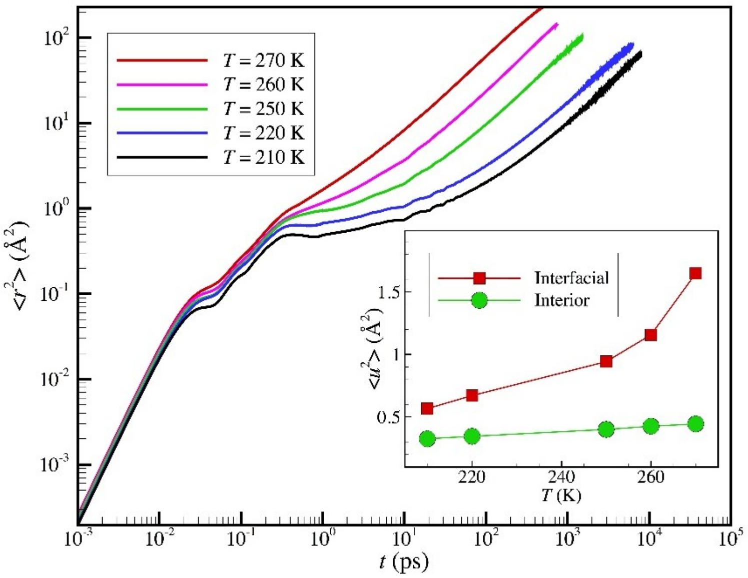

Figure 3.4 Mean square displacement of the water (log-log) in the $(11\bar{2}0)$ interfacial region of ice as a function of time at different temperatures. The inset shows the Debye-Waller factor $<u^2>$ in interfacial region and interior of the deep interior of crystal as a function of T.

Since most measurements cannot resolve the spatial gradients in $<u^2>$ in crystalline materials, it is also natural to average $<u^2>$ over the entire interfacial region and compare this interfacial $<u^2>$ to the magnitude of $<u^2>$ deep within the interior of the ice material. We show a comparison of this kind as function of T in Figure 3.4 where we see that the interfacial $<u^2>$ near T_m can be more than a factor 2 to 3 larger than its value deep in the interior of the ice material, as noted previously Kawamura et al. [80,105] Our previous simulations on the interfacial dynamics of Ni [4] and measurements on colloidal crystals [101] indicated that $<u^2>$ of atoms in the mobile interfacial region is often about twice the value of the bulk material so this significant amplification of $<u^2>$ near boundaries seems to be rather generic phenomenon associated with “interfacial pre-melting”. It is generally appreciated that this significantly larger amplitude of thermally excited atomic motion near the boundaries of crystals also explains why heterogeneous nucleation of melting tends to initiate from the boundary region. We now take a closer look at the water dynamics within the mobile interfacial layer, which is sometimes termed a "quasi-liquid" layer in the context of studies of ice. [78–81,83]

3.3.2 Quantifying Dynamics Heterogeneity Within the Mobile Interfacial Layer of Ice

The van Hove correlation function $G_s(r,t)$ describes the distribution function for molecular displacements from an arbitrary origin at $t = 0$ to a distance $r(t)$ at time t. Mathematically, the van Hove correlation function $G_s(r,t)$ is defined as, [106–108]

$$G_s(r,t) = \langle \sum_i \delta(r_i(t) - r_i(0) - r) \rangle / N \tag{3.2}$$

where $\mathbf{r}_i$ designates the atomic position of the i^{th} particle, $\mathbf{r}$ is a general position in space having a distance $r = |\mathbf{r}|$ from the origin, and N is the total number of atoms. For simple fluid undergoing Brownian motion, $G_s(r,t)$ can be described by a Gaussian function, but in glass-forming and other complex fluids $G_s(r,t)$ often develops multiple peaks reflecting the development of hopping molecular displacement motion in the fluid, after transient localization of molecules in cages created by surrounding molecules. This hopping process is evidently more complex in the interfacial dynamics of pre-melted crystal because there is a gradient in mobility in this layer so that there is averaging over hopping processes between different layers and within layers in the mobile interfacial layer. The position of the "hopping peak" in $G_s(r,t)$ accordingly varies somewhat with T rather than remaining at a fixed scale as in glass-forming liquids at fixed density. We illustrate $G_s(r,t)$ for water molecules in the ice interfacial region, defined above, in Figure 3.5. The van Hove function $G_s(r,t)$ for the interfacial atoms of crystalline Ni also exhibits this hopping phenomenon (See Figure 4 of ref. 4). We also remark on the general similarity between $G_s(r,t)$ in Figure 3.5 for the interfacial layer of ice to $G_s(r,t)$ for dense quasi-two dimensional colloidal fluids near their freezing point [109] although the height of the hopping peak in $G_s(r,t)$ is clearly relatively intense in the interfacial layer of ice in comparison to the quasi-two-dimensional colloidal suspension. Despite this superficial similarity in $G_s(r,t)$, we expect the active coupling of the dynamics of the atoms of the crystal below the interfacial leads to effects that make the interfacial mobile layer dynamics distinct from a molecular or colloidal glass-forming liquid and clear differences indeed emerge from the interfacial dynamics of crystals and glass-forming liquids below.

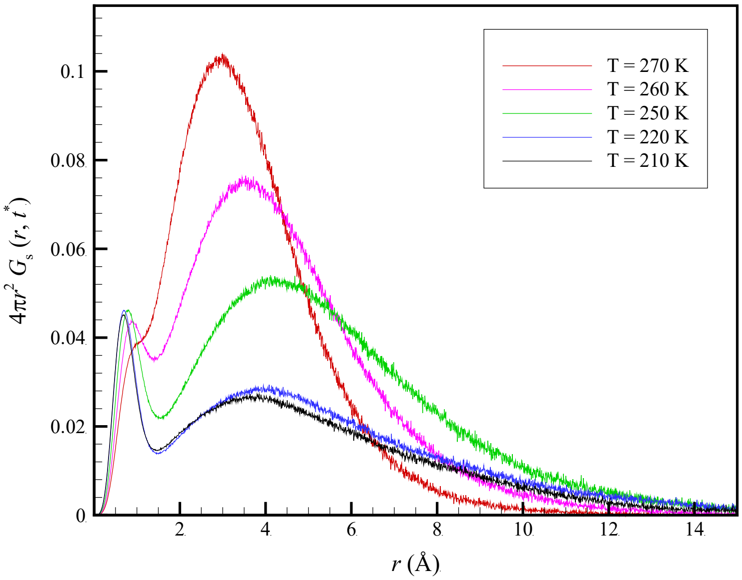

Figure 3.5 van Hove correlation function in the $(11\bar{2}0)$ interfacial region of ice at different T.

We next consider one of the most basic measures of dynamic heterogeneity (DH) in glass-forming liquids, the non-Gaussian parameter, α_2. This quantity is defined in terms of moments of the particle displacement distance from their initial position at $t = 0$ after time Δt,

$$\alpha_2(\Delta t) = (3\langle r^4(\Delta t)\rangle / 5\langle r^2(\Delta t)\rangle^2) - 1 \qquad 3.3$$

The non-Gaussian parameter α_2 is defined to equal zero for Brownian motion and this measure of dynamical heterogeneity has often been considered in previous MD simulation studies of GF liquids [110], grain-boundaries [45,111,112] and the interfacial dynamics of nanoparticles. [13,113]

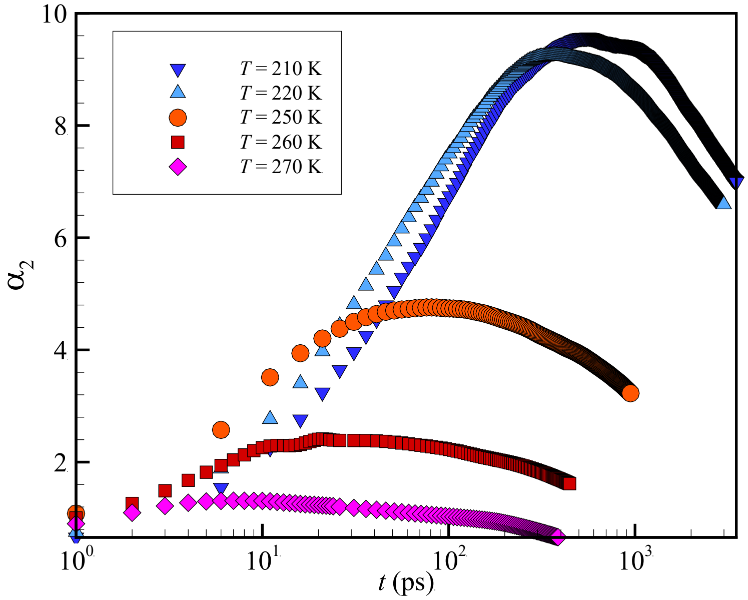

Figure 3.6 Non-Gaussian parameter in the $(11\bar{2}0)$ interfacial region of ice as function of simulation time at different T.

In Figure 3.6, we see that the peak value of α_2 progressively increases as we move away from T_m, providing clear evidence for heterogeneous dynamics. The same trend in the peak value of α_2 with T is observed the (110) interfacial region of Ni in Figure 3 of Zhang et al. [48] Again the analogy between the interfacial dynamics of Ni and ice is striking. Previously, Giovambattista et al. [53,114,115] observed a structurally similar dynamic heterogeneity in cooled liquid water and this phenomenon is familiar from experiments and simulations on essentially any glass-forming or incipiently freezing liquids.

It is well known that heterogeneous dynamics of glass-forming liquids is highly correlated with a non-Arrhenius self-diffusion coefficient D_s. Previous experimental and simulation observations on interfacial diffusion coefficients of metallic crystals as a function of T have also indicated a non-Arrhenius T dependence, [48] although the deviations observed from an Arrhenius T dependence are not as large as normally found in GF liquids. Figure 3.7(a) illustrates average mean square displacement data for the interfacial atoms of ice for a range of temperature below T_m (210 K $\leq T \leq$ 270K), and we show interfacial water D_s estimates in the inset of Figure 3.7(a). In our previous study [48] of the interfacial region of crystalline Ni, we found a similar concave upward shape of the Arrhenius plots as for D_s in the interfacial region of ice. Figure 3.7(b) shows a direct comparison of our simulation estimates of D_s for interfacial ice and the interfacial diffusion coefficient of Ni atoms in the interfacial regions of various crystallographic interfaces. We see that there is a strong correspondence between D_s for the $(11\bar{2}0)$ interface of ice and the (110) interface of Ni, as we anticipated. As a leading approximation, the T dependence of D_s exhibits high and low temperature Arrhenius regimes having rather different activation energies and prefactors [$D_s = D_0 \exp(E_a / k_B T)$]. In particular, we find the activation energy E_a to equal 0.51 eV and 0.26 eV in the high and low temperature regimes, respectively, and, correspondingly, D_0 equals 3.88×10^4 cm^2/s and 0.175 cm^2/s, respectively. The large increase in D_0 in the high T regime explains how D_s can increase upon heating while at the same time E_a becomes larger in the high temperature Arrhenius regime. A similar behavior has been observed for the interfacial dynamics of many crystalline metals, [116–118] and we suggest this trend is rather general for the interfacial dynamics of crystalline materials.

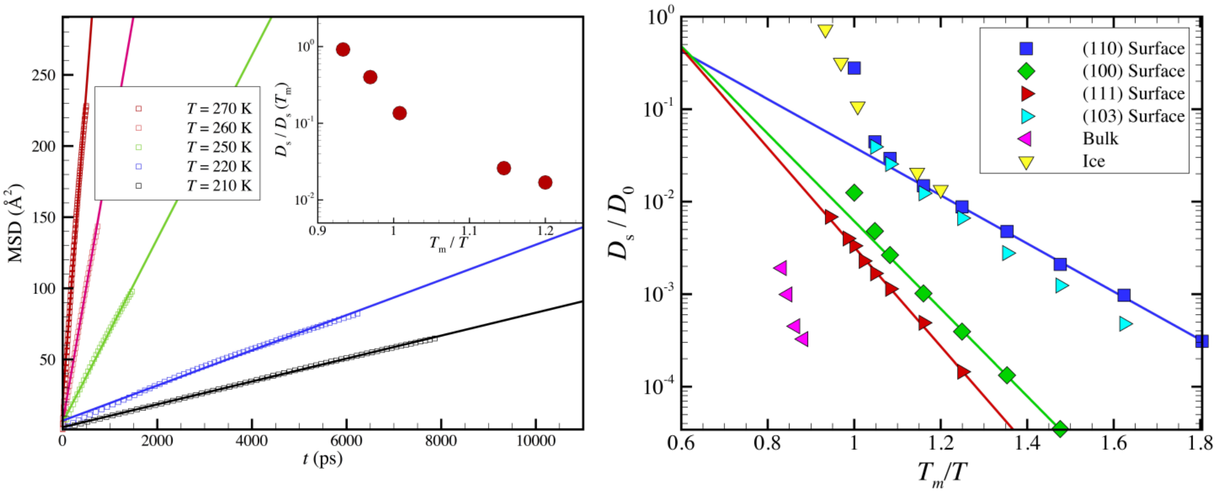

(a) (b)

Figure 3.7 (a) Mean square displacement of the water in the $(11\bar{2}0)$ interfacial region of ice as a function of time over a range of T. The inset shows corresponding reduced D estimates in the interfacial region. (b) Comparison of the reduced interfacial diffusion coefficient D_s / D_0 versus reciprocal reduced temperature T_m / T for the interface of ice and various crystallographic interfaces of Ni.

The non-Gaussian parameter $\alpha_2(t)$ provides a measure of the magnitude of mobility fluctuations [119] and the timescale where $\alpha_2(t)$ peaks t^* has previously been found [26,28,43,48,50,120] to scale with D_s / T, making t^* a characteristic diffusion or “hopping” time. Figure 3.8 confirms our expectation that D_s/T for interfacial ice likewise scale in inverse proportion to t^*, $D_s / T \sim t^*$.

This relation has been established before in glass-forming liquids [26,28,43,120], the interfacial dynamics of Ni [48], and in homogeneous melting of crystalline Ni [50], another material exhibiting dynamic heterogeneity. [28] We next characterize the structural relaxation time τ_α of the $(11\bar{2}0)$ interfacial water of ice.

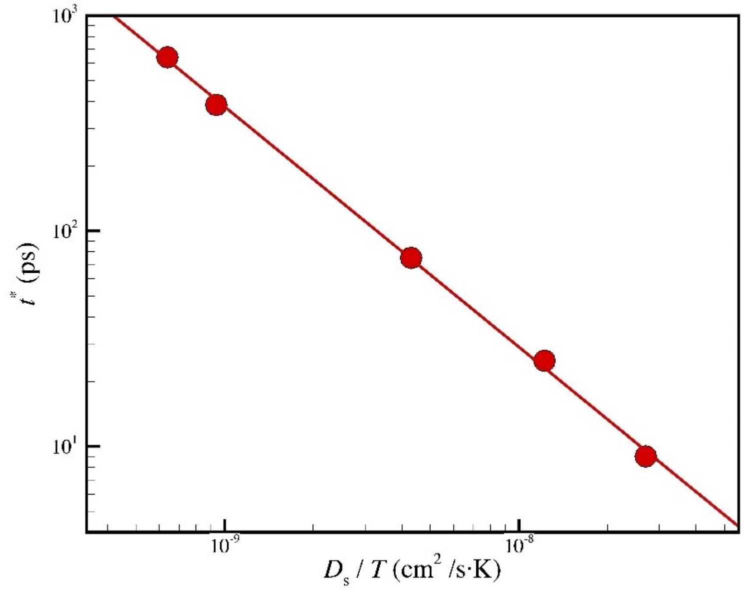

Figure 3.8 The reduced diffusion coefficient D_s / T within the $(11\bar{2}0)$ interfacial region of ice shows linear relationship with t^*, the time at which α_2 exhibits a maximum. The time t^* is the diffusive relaxation time.

Following standard practice in the field of glass-forming liquids, we estimate the structural time of the interfacial water by calculating the self-intermediate scattering function of the interfacial atoms, $F_s(q,t)$. This quantity is obtained from the Fourier transform of $G_s(r,t)$ and the magnitude of the scattering wavevector q is usually fixed to correspond to a scale on the order of the intermolecular distance. In Figure 3.9, we illustrate $F_s(q,t)$ for the same range of T as indicated for $G_s(r,t)$ in Figure 3.5. The relaxation occurs as two-step decay, a fast β-relaxation process having a timescale on the order of a ps, followed by an α-relaxation process characterized by a stretched exponential relaxation,

$$F_s(q,t)/F_s(q,t=0) \approx exp\left[-(t/\tau_\alpha)^\beta\right] \tag{3.4}$$

where τ_α is the structural relaxation time. The apparent β values obtained from fitting this data lie in a range between 0.76 to 0.9, depending on T. The relaxation time τ_α is often found to be related to D_s / T by a power law in glass-forming liquids, a phenomenon termed "decoupling". [121] The inset to Figure 3.9 shows that this relation also holds to a high approximation for the interfacial region of ice. Both these relationships were observed before for the interfacial dynamics of Ni and are universal features exhibited by glass-forming liquids. From all the accumulated evidence shown, the dynamics of mobile interfacial layer certainly resembles the dynamics of glass-forming liquid in many ways. We next investigate whether the interfacial dynamics of ice exhibits string-like molecular exchange motion, a feature observed many times before in glass-forming liquids. [68]

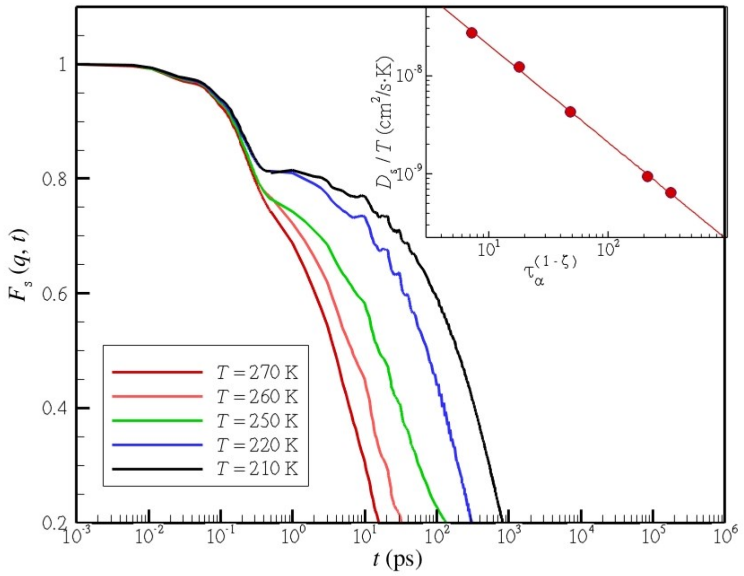

Figure 3.9 The self-intermediate scattering function for the $(11\bar{2}0)$ interfacial region of ice at different T. Those curves can be fitted using $F_s(q, t) \approx \exp[(t / \tau_\alpha)^\beta]$, where the apparent value of β varies between 0.76 to 0.9 over the T range indicated. The inset shows power-law decoupling relationship between D_s / T and τ_α, i.e., $t^* \sim (\tau_\alpha)^{1-\zeta}$, where the "decoupling" exponent ζ is estimated to be $\zeta \approx 0.1$.

3.3.3 String-like Collective Motion in the Mobile Interfacial Layer

The identification of cooperative exchange motion first requires the isolation of mobile particles that move further at t^* in comparison to Brownian particles. The mobile molecules in the interfacial region are defined as those that make displacements beyond the first minimum in $G_s(r,t)$ at the characteristic diffusive time, t^*. This well-defined cut-off scale is about 1.8 Å in Figure 3.5 and varies weakly with T. An examination of the mobile particles shows that their positions are highly correlated in space in the form fractal structures. In a series of recent papers, we have investigated collective motion in GF liquids [68], as well as in Ni GBs [45] and in the interfacial dynamics of Ni NPs[49], and in each case, there is a similar development of clusters of mobile clusters upon changing temperature.

Investigations of other strongly interacting particle systems have consistently indicated that the mobile particle clusters just defined are themselves clusters of more primitive clusters of particles undergoing string-like correlated motion. An examination of the specific geometrical form of the collective motion occurring on the secondary prismatic surface of crystalline ice reveals that we are dealing with the same physical phenomenon, cooperative string-like collective motion of water molecules. Since we have repeatedly described our method for determining these dynamic structures in recent publications in the context of other strongly interacting particle systems [13,28,45,48–50,113,119,122,123], we only briefly describe the method of characterizing this motion in Appendix A.** The basic idea of this procedure is that we sort the mobile particles into clusters constrained by the condition that they stay within about an intermolecular distance from each other within the lifetime over which the mobile clusters and strings exist, i.e., *t**.

Figure 3.10 illustrates representative strings of water molecules in the mobile interfacial layer of the secondary prismatic plane of ice at $T = 250$ K. The lines connect O atoms that belong to the same collective atom movement, in which the arrows indicate direction of atom movement, and the colors are introduced to help discriminate between distinct strings. The light grey molecules do not participate in the string-like cooperative motion. As in many previous studies of strings in other physical contexts, the mass distribution of these molecular exchange events is nearly exponential, as shown in Figure 3.11, and the average length of the strings $L \equiv \langle n \rangle$ obtained from these distributions is indicated in the inset of this figure. While the extent of cooperative motion in the interfacial grows upon cooling as in glass-forming liquids, [68] this trend is *not* the same as observed before in the interfacial dynamics of the (110) interface of Ni where *L* was found to *increase* upon heating. We return to this conspicuous difference between the interfacial dynamics of these materials below where we find that the *T* variation of *L* depends strongly on the particular type of interface, even for a fixed material type. We again emphasize that the interfacial dynamics of crystals clearly has aspects that are distinct from glass-forming materials.

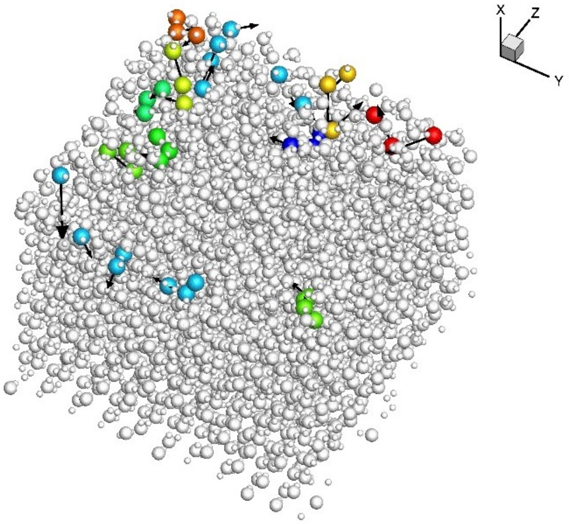

Figure 3.10 String-like collective atomic motion in the $(11\bar{2}0)$ interfacial region of ice at 2 K below the melting temperature. The lines denote O atoms that belong to the same collective atom movement, arrows indicate direction of atom movement, and the colors are introduced to help discriminate between distinct strings.

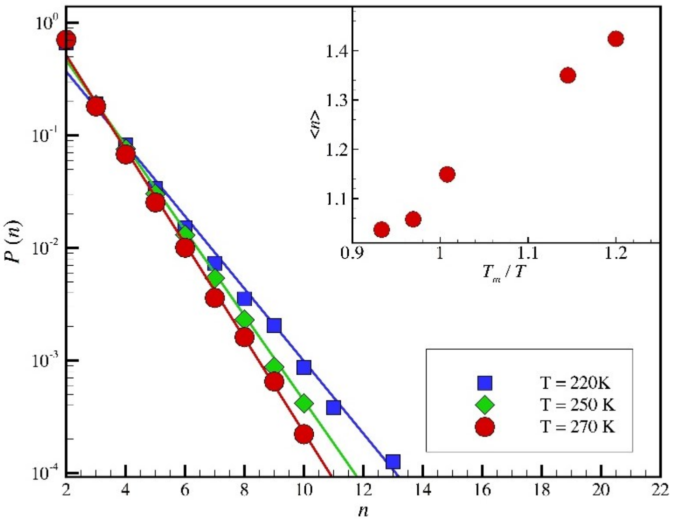

Figure 3.11 String-length distribution, $P(n)$, as a function of the length of the string for the $(11\bar{2}0)$ interfacial region of ice. The inset shows the average string, $L = \langle n \rangle$, as a function of temperature.

3.3.4 Colored Noise, Quakes and Collective Motion in Interfacial Ice

The existence of molecular clustering of mobile atoms in the interfacial regime of ice, and other strongly interacting fluids [13,48,68,123–125], implies the existence of mobility and potential energy fluctuations that should be observable as *noise* in the time series of these properties. In past studies of the interfacial dynamics of Ni nanoparticles, we found the time series for potential energy fluctuations and $\langle u^2 \rangle$, which is directly related to the average particle mobility [13], exhibit colored noise with a power spectral exponent α dependent on T and related to the scale of collective motion L under a wide range of conditions (doping the surface with different atoms to tune the scale of collective motion, varying nanoparticle size, etc.). In particular, we found that the noise exponent α for $\langle u^2 \rangle$ fluctuations was related to the scale of collective motion L by the approximation, $\alpha \approx L - 1$, and theoretical arguments were given to rationalize this relation based on the hypothesis that the string length distribution determines a distribution of activation energies for hopping displacement of the molecules. [13] The same relationship between α and L has been observed in the interfacial dynamics of Ni [48] and the internal dynamics of ubiquitin dissolved in glycerol, [123] although the data supporting this finding was found to be more limited and uncertain.

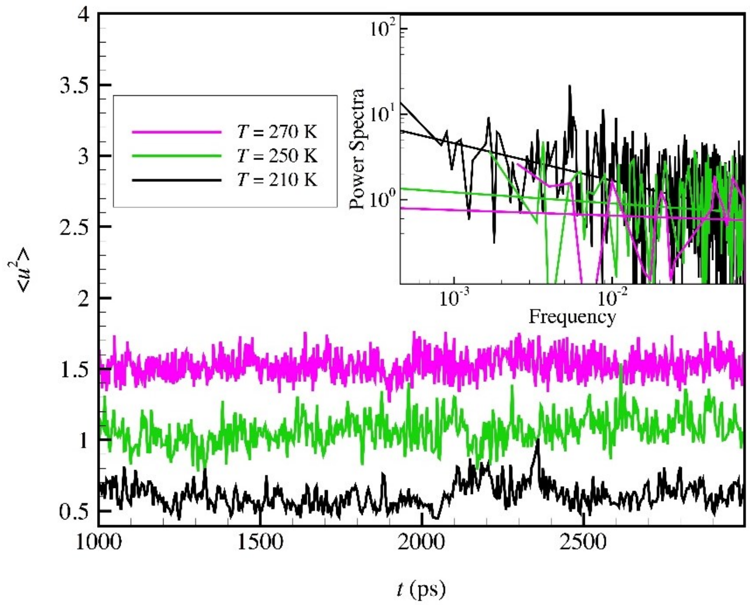

Figure 3.12 A representative portion of the $<u^2>$ times series from which the power spectra are derived at three different temperatures. The inset shows the power spectrum of $<u^2>$ fluctuations of the water molecules in the $(11\bar{2}0)$ interfacial region of ice.

We next consider whether the α noise exponent informs on the scale of collective motion L in the interfacial dynamics of ice. First, we illustrate the times series of $\langle u^2 \rangle$ for fluctuations of the interfacial water molecules for a range of temperatures (T = 210 K, 250 K, 270 K) in Figure

3.12. The observed $<u^2>$ fluctuations clearly have long correlations, and we show the power spectrum of the $<u^2>$ in the inset of Fig 3.12. Based on the α and L estimates given above, we check the relation $\alpha \approx L - 1$ in Figure 3.13. The noise exponent α and L are clearly correlated, but the data exhibit some uncertainty as in our former study of the interfacial dynamics of Ni. The growth of the color in the noise associated with mobility fluctuations grows hand in hand with the extent of collective motion.

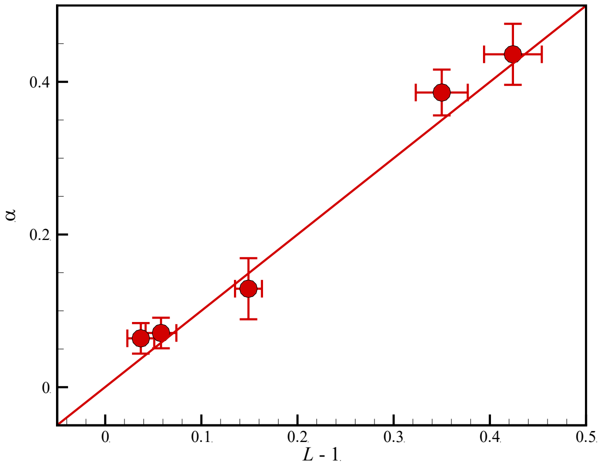

Figure 3.13 Noise exponent α of $<u^2>$ versus extent of collective motion, $L - 1$. To obtain uncertainty estimates, we estimated L uncertainty from the standard deviation of the slope fitted in Figure 3.11 where we assuming the curves are described by an exponential function, while the uncertainty of the noise exponent was estimated from a standard deviation from a fit of the noise spectra in Figure 3.12 to the power law function.

In our previous study of the interfacial dynamics of Ni we found that the time series for the $<u^2>$ values exhibited large fluctuations in intensity that resembled the power distribution in intensity observed in earthquake data. [126] This phenomenon was observed both for the interfacial dynamics of Ni nanoparticles [119] and the (110) interface of bulk crystalline Ni [48], and recently we found this phenomenon to arise even in the internal dynamics of the protein ubiquitin [123] so that this phenomenon seems to be rather general. Figure 3.14 (a) shows representative quake-like displacements for mobile molecules and immobile molecules, and Figure 3.14 (b) shows the probability distribution function $P(u^2)$ for the intensity of these $<u^2>$ "quake" events at $T = 250$ K where we again observe a power law scaling, $P(u^2) \sim (u^2)^{-\gamma}$. The inset shows that quake exponent γ changes in a concerted fashion with the $<u^2>$ noise exponent α and the average string length, L.

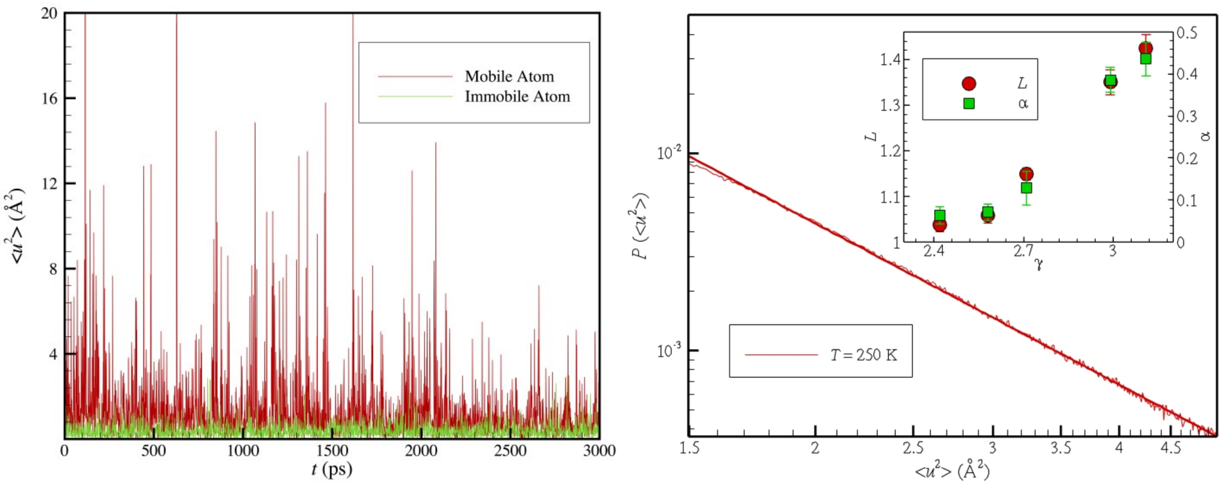

(a) (b)

Figure 3.14 (a) Representative quake-like displacements for mobile molecule and immobile molecule, (b) Probability distribution function $P(<u^2>)$ for $<u^2>$ events (peak values of $<u^2>$ in Figure 3.12) in the $(11\bar{2}0)$ interfacial region of ice at $T = 250$ K where we observe a convincing power law scaling, $P(u^2) \sim (u^2)^{-\gamma}$ as in previous systems showing glassy dynamics. The inset shows that the *quake exponent* γ varies in a correlated fashion with the $<u^2>$ noise exponent α

and the average string length L. To obtain uncertainty estimates, we estimated L uncertainty from the standard deviation of the slope fitted in Figure 3.11 where we assuming the curves are described by an exponential function, while the uncertainty of the exponent was estimated from a standard deviation from a fit of the noise to the power law function describing $P(<u^2>)$.

3.3.5 Activation Energy E_a (T) and the Mobile Interfacial Layer Width ζ (T)

In previous studies of both the interfacial dynamics of simulated glass-forming films [42] and the interfacial dynamics of the (110) interface crystalline Ni, [48] we found that the interfacial mobility scale ξ seemed vary linearly with L, while showing no obvious correlation to the density gradient in the interfacial region of the material. Unfortunately, when we consider this relation it does not hold for the secondary prismatic interfacial region of ice. In Figure 3.15, we observe that L increases upon cooling while ξ increases upon heating; ξ and L thus vary in an approximately *inverse* relation to each other for this interface. We must conclude that the linear scaling relation between ξ with L is not general for the interfacial region of crystalline materials.

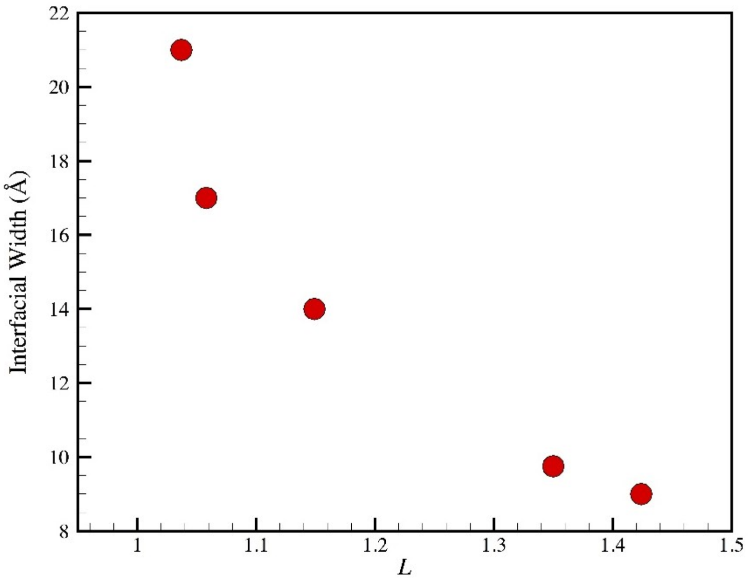

Figure 3. 15 The correlation between interfacial width and the average string length L in the $(11\bar{2}0)$ interfacial region of ice.

We also find that the direct proportionality between the D_s activation energy $E_a(T)$ and L, found before both for the (110) interfacial region of crystalline Ni and in the interfacial dynamics of both metallic [48] and polymeric glass-forming liquids [41,42,55,71,72,127–130], also fails to hold for the secondary prismatic plane of interfacial ice. Figure 3.16 shows that $E_a(T)$ decreases upon cooling, while L increases upon cooling. This is the first time in which we have seen that a change in $E_a(T)$ does not correspond to a proportional change in L. The relationship between $E_a(T)$ to the scale of cooperative particle exchange motion L apparently works differently in the interfacial dynamics of ice. We have checked other crystallographic interfaces of Ni and found the (110) interfacial dynamics of crystalline Ni follows a similar pattern of behavior as we have found for $(11\bar{2}0)$ interfacial region of ice. Unexpectedly, the relation between L and ξ depends on the particular crystallographic interface!

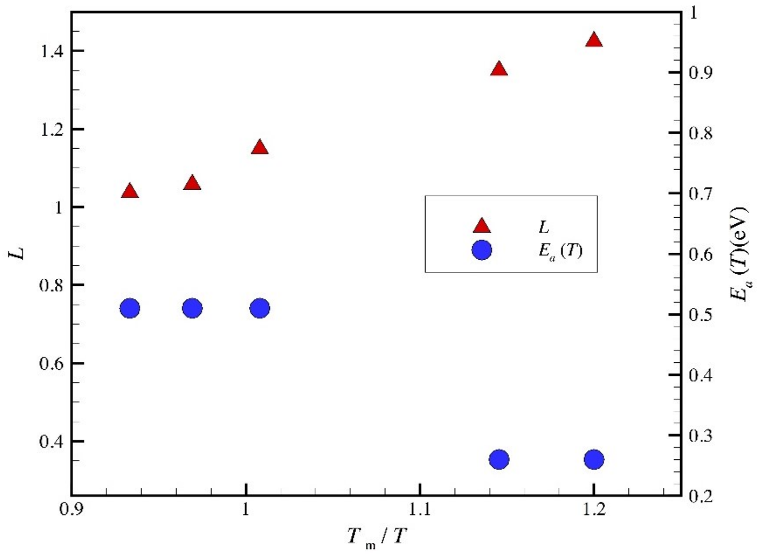

Figure 3.16 The correlation between L and apparent activation energy $E_a(T)$ for diffusion in the $(11\bar{2}0)$ interfacial region of ice.

If not L, what property of the interfacial region of crystalline materials governs the change in $E_a(T)$? It is evident that for all crystallographic interfaces that we have investigated that the $E_a(T)$ increases in parallel with the interfacial width and this trend is also observed in supported glass-forming polymer films. Perhaps the interfacial width itself is the more fundamental quantity governing the change of $E_a(T)$ with temperature in crystalline materials? We test this hypothesis in Figure 3.17, where the $E_a(T)$, normalized by its value in the low T Arrhenius regime, is plotted against the interfacial width of mobile interfacial layer divided by the average interfacial width before and after transition. The values of the high and low T activation parameters and normalizing interfacial width corresponding to this plot are given in Table 3.1. The reduced activation energy and reduced interfacial width vary proportionately in the region where $E_a(T)$ varies with T, but the reduced activation energy $E_a(T)$ approaches a plateau value at high temperature that apparently depends on the interface type and material. The entropy theory of glass-formation as applied to flexible glass-forming polymers [131] and experimental studies on glass-formation [132,133] are also consistent with the existence of a high and low T regimes of glass-formation having different activation energies whose relative values are material system specific, separated by a T range in which $E_a(T)$ changes with T.

Table 3.1 Activation energy parameters and normalizing thickness of different surfaces.

	Ice $(11\bar{2}0)$	Ni (110)	Ni (100)	Ni (103)
E_a (High) (eV)	0.51	1.68	2.64	1.57
E_a (Low) (eV)	0.26	0.83	1.49	0.94
Normalizing ξ (Å)	12.0	8.5	7.0	11.3

We again see another common phenomenological pattern in the interfacial dynamics of a crystalline material to glass-forming liquids, but at the same time we find a different relationship between the scale of collective molecular motion and the activation energy $E_a(T)$ and interfacial width ξ in these strongly interacting forms of condensed matter.

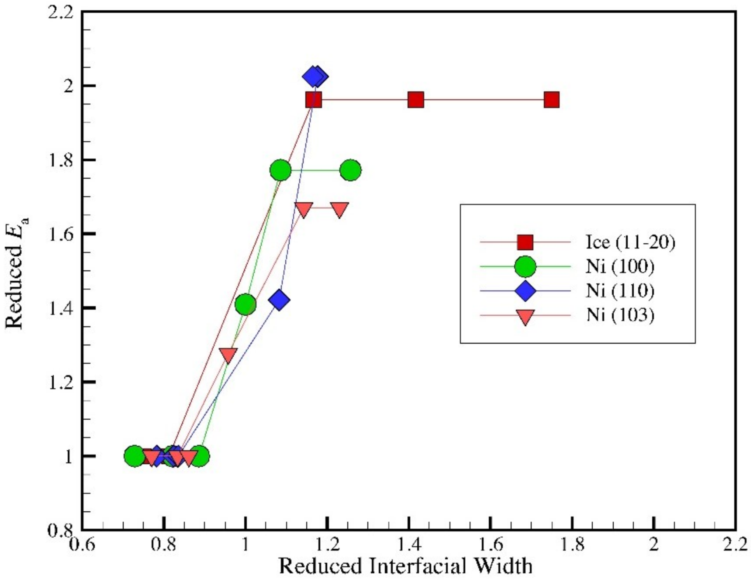

Figure 3.17 Reduced activation energy for diffusion in interfacial regions of Ni and the $(11\bar{2}0)$ interfacial region of ice.

3.4 Conclusions

In current study, we performed molecular dynamics simulation to examine string-like collective atomic motion and self-diffusion on ice $(11\bar{2}0)$ free surface and utilize tools drawn from glass-forming liquids to quantify the dynamics of interfacial ice. Our simulation results for interfacial ice were compared with our former simulations of the interfacial dynamics of crystalline Ni since both the (110) interface of Ni and the $(11\bar{2}0)$ secondary prismatic plane of hexagonal ice are relatively loosely packed crystalline interfaces. In our simulation, we utilized the TIP4P/2005 water potential [89] to describe the water intermolecular interaction in ice. For all the T examined, the amplitude of atomic motion in the interfacial region is significantly larger than in the interior crystal, explaining the origin of the “premelting” phenomenon and why heterogeneous nucleation of crystal melting tends to initiate from the boundary region.

Utilizing tools drawn from GF liquids, such as non-Gaussian parameter, the self-part of van Hove correlation functions, surface diffusion coefficients, and self-intermediate scattering function of the interfacial atoms, we quantify the dynamics of interfacial ice. Our simulation results show that the peak value of the non-Gaussian parameter becomes larger as T becomes further below T_m, the same trend observed before in the (110) interfacial region of Ni. The van Hove function of the interfacial water exhibits a multi-peaked structure, a feature often observed in glass-forming liquids that reflect the development of hopping motion in the fluid after transient localization of molecules in a cage, although this hopping motion is more complex due to gradient in mobility in the interfacial layer and different rates of hopping within the layer and between the different layers. The surface diffusion coefficient D_s / T shows inversely proportion to the peaks t^* in $\alpha_2 (t)$, a relation established before in glass-forming liquids. In addition, the relaxation time obtained from the intermediate scattering function is found to be related with D_s / T. From all this accumulated evidence, the interfacial dynamics of ice certainly resembles the characteristic dynamics of glass-forming liquids in many ways.

In all the glass-forming liquids that we have investigated before, we have observed string-like collective molecular exchange motion, a phenomenon that we believe is universal to all glass-forming liquids. We then characterized such molecular motions in the $(11\bar{2}0)$ interfacial region of ice and found cooperative motion that grows upon cooling as found before in glass-forming liquids. This trend is also not consistent with previous observations on interfacial dynamics of the (110) interface of Ni where the extent of string-like collective motion was found to grow upon heating rather than cooling, although we found that other interfaces of Ni were consistent with our findings of the dynamics of the $(11\bar{2}0)$ interface of water. The cooperative motion in the interfacial regions seems to be sensitive to the particular crystallographic interface considered so that some aspects of the dynamics of crystalline interfaces are evidently different from glass-forming liquids or colloidal fluids near their freezing point or glass transition. In addition, we examined the α noise exponent of the $<u^2>$ for fluctuations of the interfacial water molecules and found the noise exponent α and L to be highly correlated. The growth of the color in the noise is generally associated with mobility fluctuations that increase with the extent of collective motion.

Although we do not find a direct proportionality between the activation energy $E_a(T)$ for self-diffusion D_s and the width ξ of the mobile interfacial layer and the scale of collective motion L as found in the (110) interfacial region of crystalline Ni, we do find that $E_a(T)$ changes in proportion to $E_a(T)$ in the temperature range where $E_a(T)$ and ξ vary. Evidently, while the interfacial dynamics of crystalline materials and glass-forming materials exhibit many similarities, they also exhibit some dynamical properties that are rather distinct. Further simulation, experimental and theoretical studies are needed to better understand the relationships between these strongly interacting and disordered materials.

4. Universal Nature of Dynamics Heterogeneity in Glass-forming liquids: A Comparative Study of Metallic and Polymeric Glass-forming liquids

4.1 Introduction

Glass-formation has been observed in diverse materials ranging from biological matter and synthetic polymeric materials to metallic and other inorganic GF materials, a phenomenon having profound significance for materials design, processing and performance. Measurements on the dynamics of glass-forming liquids often show a dramatic slowing down of the relaxation dynamics and diffusivity that is accompanied by a large increase in the viscosity, which is often non-Arrhenius. [134] The dynamics of these complex GF liquids are often characterized by "dynamic heterogeneity" in the form of transient polymeric clusters of highly mobile atoms. This type of heterogeneous dynamics is characteristic of grain boundaries at elevated *T* [45], the interfacial dynamics of NPs, [49,122] dynamics of both metallic [28,48,50] and polymeric GF liquids in the bulk state, and the simulated dynamics of lipid membranes. [135,136] In addition, heterogeneous dynamics has also been observed in superionic materials, which are currently of intense interest in the development of safer, more efficient and longer lasting battery materials, and are also of great interest in understanding geophysical phenomena associated with the properties of the earth's Fe core and the $MgSiO_3$ perovskite material composing a substantial fraction the earth's lower mantle. [137–141] Apparently, dynamic heterogeneity is a *universal* phenomenon of materials composed of strongly interacting particles in a non-crystalline state of organization. Here, the term 'strongly interacting particle' system refers to material systems exhibiting non-trivial collective particle motion, distinct from ideal crystalline matter involving particles interacting with approximately harmonic interactions and dilute gasses, as a dynamical consequence of strong interparticle interactions. Typically, these strong interactions arise in equilibrium materials at high densities or in particle systems exhibiting long range repulsive interactions (e.g., dusty plasmas [142], Wigner glasses [143,144]), but such strong interactions, and associated collective particle motion, also arise in non-equilibrium systems such as sheared fluids, fluids in temperature gradients and other fields, self-propelled particles, etc. Molecular glass-forming liquids are a prototypical strongly interacting fluids that exhibit collective particle motion [145] upon approaching the glass transition temperature T_g and corresponding exhibit large changes in their dynamic material properties associated with the emergent collective motion. We also view superionic crystalline materials [146], the grain boundaries [45] and free interfaces of crystalline materials approaching their melting temperatures [48,147], lipid membranes [136], folded proteins [123] and duplex DNA [148] to be strongly interacting particle systems. It is apparent from the discussion above that many real materials fall into this category.

A common physical feature of GF liquids is a strong driving force for local ordering, where the ordering process is "frustrated" by competing interactions, geometrical constraints or the kinetics of molecular reorganization, resulting in the formation of an amorphous solid state at sufficiently low temperatures, high densities or the presence of constraints, such as cross-linking polymer materials, geometrical confinement, etc., that ultimately do not allow the material to crystallize. Although some materials have shown a tendency for this packing frustration to be reflected in regions of high and low relative packing efficiency (quantified by the local relative density) and for these local density fluctuations to be correlated with local changes in molecular mobility (see Appendix B), no general correlation between local density and mobility seems to exist in condensed materials. [145,149–151]

Nonetheless, the occurrence of large fluctuations in local mobility in glass-forming liquids has been established by many experimental [152–156] and simulation [157–160] studies and continuing efforts are currently being made to quantify the origin, nature and form of these mobility fluctuations. These fluctuations have been investigated in particular detail in model polymeric glass-forming liquids since these fluids are single component fluids that are apparently not capable of crystallization, greatly simplifying the study of the equilibrium and dynamic properties of these materials under conditions of incipient glass-formation. [55,130]

We note that traditional models of the dynamics of glass-formation are of a mean field nature and inherently neglect dynamic heterogeneity in the form of mobile and immobile particle clusters, and we briefly mention some models of this kind as a point of reference to our discussion below where the significance and nature of fluid dynamic heterogeneity (i.e., fluctuations) is emphasized. There are defect diffusion models such as Glarum model [161] and its extensions [162] where high mobility regions are considered to arise from rare density fluctuations in viscous liquids that act like "defects" that diffuse through the material, facilitating material relaxation in a fashion similar to vacancies and interstitials in crystalline materials. [163,164] There are also mean field "free volume" models of glass-forming liquids [165,166] and various "caging" based models (e.g., mode-coupling theory [167,168]), preserving the essential spirit of the free volume models, that assume that the slowing of the dynamics of GF liquids arises solely from constraints on the motion of a typical particle moving in an average field of surrounding particles that progressively restricts particle motion as the fluid density is increased and the available space for particle motion becomes reduced. More recently, kinetic Ising models of glass-forming materials [169,170] have been introduced to consider the effect of defect clustering and cooperative motion induced by defect clustering on structural relaxation. While these are instructive toy models exhibiting dynamic heterogeneity, these models have not yet been developed to quantitatively describe molecular GF liquids.

There are interesting attempts in this direction, however. Angell and Moynihan [171] have developed an interesting phenomenological defect excitation model that emphasizes the interaction of defects and emergent cooperativity and attempts to address specific features of real glass-forming materials such as the origin of the Boson peak and two-level systems. Isobe et al. [172] have made an interesting attempt at describing glass-formation in hard sphere and hard disc liquids based on the 'facilitated' kinetic Ising model of Chandler and coworkers. [170] In our view, the development of a fundamental theory of GF liquids is still a work in progress. Berthier and Biroli [173] have reviewed various models of GF liquids, observations of spatially heterogeneous dynamics of these materials, describing the successes and failures the various approaches, and the reader is referred to this work and the experimental articles by Angell et al. [9] and Richert [174] for a perspective emphasizing an experimental perspective.

More recent modeling of GF liquids has emphasized the use of molecular dynamics simulation methods and methods of analyzing this data that stresses the importance of many-body interactions in GF liquids and other strongly interacting materials, and the associated emergence of dynamic heterogeneity (the appearance of particles having correlated mobility and collective motion). This type of modeling has a long history going back to Adam and Gibbs (AG) [36], and even earlier, but this approach has received significant impetus from recently simulation studies in which dynamic heterogeneity and collective motion of significance for the dynamics have been clearly identified by molecular dynamics simulation. For example, Starr et al. [55] have shown that dynamic clusters of both high and low mobility of polymer segments are formed in simulated cooled polymer melts where these mobility clusters that are largely uncorrelated in space with the chemically bonded polymers comprising these fluids. Dynamic clusters of mobile and immobile particles having a branched polymeric form coexist and interpenetrate, growing in a parallel fashion and forming percolating structures as the material is cooled towards the glass transition This interpenetrating network structure of particles of extreme mobility is phenomenologically associated with the emergence of the complex viscoelasticity and solid-like properties of the material, but there are many open questions about the precise structure property relations between these dynamic clusters and the observable properties of GF liquids.[55] Previous work has also established that the lifetimes of the mobile and immobile clusters correlate strongly with the characteristic times associated with diffusion and structural relaxation, respectively, and that these timescales become increasingly separated upon progressive cooling, providing a structural explanation of the "decoupling" phenomenon between the molecular diffusion coefficient *D* and structural relaxation time in terms of the relative persistence of these dynamic clusters as *T* is varied. It was also found that the mobile and immobile particle clusters exhibit highly similar geometric forms that are characteristic of the self-assembly of branched equilibrium polymers in terms of the fractal dimension, size distribution, etc.[55] (See discussion comparing mobile and immobile clusters to the formation of branched equilibrium polymers below.). Starr et al.[55] also found that the mobile particle clusters in model polymer liquids are comprised of sub-clusters of polymer segments exhibiting cooperative exchange motion where the average size of these clusters was found to quantitatively correlate with changes in the activation free energy for structural relaxation.[55] Xu et al.[71] later made an in-depth investigation of cooperative motion and dynamic heterogeneity in polymer melts under conditions where the pressure and cohesive interaction strength were varied over a large range to "tune" the fluid collective dynamics. The principal goal of the present work is to investigate dynamic heterogeneity in a range of model metallic glass materials to assess the generality of previous observations on dynamic heterogeneity in coarse-grained polymer melts.[55]

Given previous finding indicating that local "free volume" arguments cannot be applied generally to understanding the dynamics of GF liquids, [145,149–151] it is imperative to check the generality of the methods and results of Starr et al. for GF liquids before accepting the universality of the approach to the quantification of dynamic heterogeneity in GF liquids. In the present work, we address this issue by investigating metallic GF liquids that have completely different chemistry, and do not have a polymeric nature. If the same dynamic heterogeneity phenomenology arises in this family of glass-forming liquids, then we think it is safe to infer that this type of dynamic phenomenon is "universal". In our specific interest of metallic glass materials, this situation is illustrated by simulations of Cu-Zr metallic glasses, where some correlation with local packing efficiency and local mobility has been noted, [28,43] while the prevalence for locally preferred (icosahedral) packing in Pd-Si metallic is extremely limited [175] so that no general correlation between local preferred packing and mobility seems to exist. We also investigate Ni-Nb metallic glass materials in view of the increasing technological interest of this class of metallic glasses. [1,176,177] Wei et al. review recent attempts to correlate local structure to dynamics in Cu-Zr and other model atomic glass-forming fluids. [178] It is currently unclear whether any structural indicator exists that can predict changes in the local mobility in glass-forming liquids. The only thing that is certain at this point is that the popular "free volume" model, which assumes that local variations in the density are responsible for local variations in mobility, can be excluded.

Our simulations indicate that the dynamical heterogeneity phenomenon, and the quantitative relations between this heterogeneity and the dynamical properties of these fluids are remarkably similar in metallic and polymeric GF systems, confirming the generality of the dynamic heterogeneity of the phenomenon and the applicability of our methodologies for quantifying the dynamic heterogeneity. In particular, in all the metallic glass systems investigated, both the mobile and immobile particles exhibit geometric characteristics similar to branched equilibrium polymers upon cooling. [55] The characteristic timescale for mobile and immobile particles are directly related to diffusion and structural relaxation in all the systems of interest. In addition, four-point susceptibility suggests the growth of immobile cluster size is closely related to relaxation, which is similar to dynamics of a simulated polymer melt. [71]

Before proceeding to our analysis of our model metallic GF materials, we note that these materials have many special properties that independently merit the study of these materials as a class distinct from crystalline and metallic polycrystalline materials. Metallic glasses (MGs) have no crystalline defects such as vacancies, dislocations, and grain boundaries, the existence of amorphous structure makes MGs have high strength, exceeding about 3 GPa, and high resistance to corrosion in comparison to their crystalline counterparts.[179] MG are thus attractive candidate materials for applications that require high strength and corrosion resistance. Since metallic glasses share many dynamic properties with polymeric GF liquids, but they still have dramatically different chemistry and structure. [28] Metallic glasses are "amorphous" structurally, although they do exhibit some medium or short-range ordering. These are supercooled liquids in which the "amorphous" structure arises during non-equilibrium fast cooling process due to "packing frustration" between the different types of atomic species. In general, materials of this kind will crystallize after "aging" for sufficient times [180], explaining the designation "supercooled liquid". Polymeric glass-forming liquids, however, appear to have sufficient disorder, at least in some cases, so that these materials apparently may form an equilibrium glass state at low temperatures. From a computational perspective, however, it is reasonable to ignore this distinction between the equilibrium and non-equilibrium nature of these different types of GF materials given the long-lived nature of the supercooled liquid condition in metallic GF liquids. We are thus led to examining the dynamics of atomic and polymeric GF liquids regardless of the previous suggestion that the dynamics of these materials should be completely different. [181]

4.2 Simulation Methodology

MD simulations were performed to examine the dynamic behavior in Cu-Zr, Ni-Nb, and Pd-Si metallic glass systems. The MD simulations were carried out using LAMMPS, which was developed at the Sandia National Laboratories. [99] The atomic interaction in metallic glasses system was described by semi-empirical potentials optimized to reproduce the measured static structure factor and other equilibrium properties of Cu-Zr, Ni-Nb, and Pd-Si alloys. [58,182–184] Previous studies based on these potentials have established that these potentials provide a reasonably good description of both the structural and dynamic properties of these alloys. [175,182,185] In the present work, the representative alloy types and compositions were chosen ($Cu_{36}Zr_{64}$, $Cu_{50}Zr_{50}$, $Cu_{64}Zr_{36}$, $Ni_{50}Nb_{50}$, $Ni_{62}Nb_{38}$, and $Pd_{82}Si_{18}$) based on empirical rule that metallic alloys often form good metallic glasses near the eutectic points of the alloys. [186,187] We arrived at these alloy compositional choices based on published reports of the phase diagrams of different alloys [187,188] which are close to their eutectic points of the selected metallic glasses.

We next describe the simulation methods for molecular dynamics simulations of metallic glasses. First, taking $Cu_{64}Zr_{36}$ as an example, we start with a perfect Cu single crystal containing 13500 atoms with a simulation cell around (6.4 × 6.4 × 6.4) nm in X, Y, and Z-directions. Then, we randomly replace 36 % of Cu atoms by Zr. The mixture of Cu and Zr crystal was then heated from 300 K to 2000 K. After melting, the system was kept at 2000 K for 5 ns to allow relaxation to ensure the formation of a structurally homogeneous glass-forming liquid. Finally, the system was cooled down to 300 K with a cooling rate of 100 K/ns. During the entire procedure, NPT (constant number of atoms, constant pressure, and constant temperature) ensemble was employed with zero pressure and periodic boundary conditions. The constant pressure was controlled by the Parrinello-Rahman algorithm, [63] and temperature was maintained by the Nose-Hoover thermostat method. [61,62] Isothermal heating below melting point for an extended period of time would ensure the system to reach equilibrium, allowing us to probe kinetic processes. In order to obtain relatively stable supercooled [180] metallic glass-forming liquids, isothermal heating simulations were also performed from 700 K to 1400 K, with interval of 50 K. At every temperature, simulation lasts at least 5 ns and up to 30 ns, depending on the temperature. Atomic configurations were saved every 1 ps for further analyses.

4.3 Results and Discussion

4.3.1 Definition of Immobile Particles and their Clustering in Supercooled Liquids

In our previous work, we took Cu-Zr metallic glass alloys as model system to carefully examine the dynamic behavior of supercooled metallic liquids with a focus on mobile particles. [28] We found that some particles form locally preferred packing configurations, but a large portion of particles is left to “wander” with high energy and free volume (i.e., relatively low local density), and exhibit collective atomic motions that can be characterized using average string length. In particular, the change in average string length, L, can approximate the temperature dependence of diffusion coefficients D, viscosity, and the relaxation time, τ_{α}. The string theory of relaxation suggests that the relaxation time can be expressed using average string length, implying that the changes in the structural relaxation are dominated by the changes in the average length of string-like cooperative motions. [29,41] In Cu-Zr alloys, we found a linear relationship between activation free energy for diffusion $\Delta\mu\, L/kT$ and characteristic time for diffusion $ln\ (t^{*}/t_0)$, which means that the change in the activation free energy for diffusion is proportional to the change in the average string length. Since the correlation between relaxation time, τ_α and diffusion coefficient, D can be described by the "decoupling" power-law, the change in average string length simultaneously describes the change of the activation free energy for the structural relaxation time and D. [28] However, a true relationship between the structural relaxation time and well-packed clusters is not explicitly established in this work.

In the current work, we will pay more attention to the dynamics of immobile particles and its relationship with mobile particles. The first step is to define a unified way to distinguish particles of extreme mobility in cooled liquids and other forms of strongly interacting matter that is independent of the material composition and chemistry. Starr et al. [55] have established a robust measure to identify mobile and immobile particles in a model polymer melt and we first examine whether the same methodology can be applied for metallic glass materials. Since the goal is to establish a generality of the method of Starr et al. [55], we closely follow the methodology of this work to identify immobile particles. We will mainly focus on the $Cu_{64}Zr_{36}$ to illustrate the analysis involved, but sometimes we will refer to other systems if a special point is to be made.

In order to identify the immobile particles, the first step is first necessary to define a cage size. [55] Figure 4.1 shows a typical mean square atomic displacement $<r^2>$ as a function of simulation time at different temperatures in $Cu_{64}Zr_{36}$ alloy. The mean square atomic displacement $<r^2>$ exhibits a well-defined plateau after a particular decorrelation time characterizing the crossover from ballistic to caged atom motion and $<r^2>$ at long times is diffusive. Since the logarithmic derivative $d\left(\ln\langle r^2(t)\rangle\right)/d(\ln t)$ exhibits a minimum on the time scale of particle caging, t_{cage}, we can precisely define the cage size by $r_{\text{cage}} \equiv \langle r^2(t_{\text{cage}})\rangle^{\frac{1}{2}}$, as shown in Figure 4.1(b). The inset in Figure 4.1(b) shows the cage size as a function of temperature in $Cu_{64}Zr_{36}$ alloy. Apparently, the cage size decreases as temperature approaching glass transition temperature. Effectively, caged particles or "immobile" particles can be defined as those particles having a mean square displacement less than $\langle r^2_{\text{cage}}\rangle$.

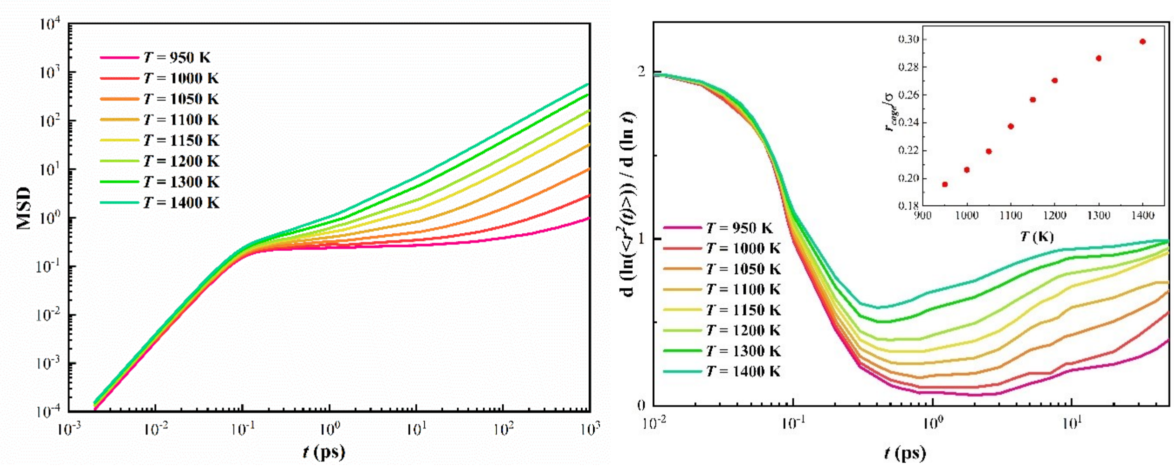

(a) (b)

Figure 4.1 (a) Mean square displacement of $Cu_{64}Zr_{36}$ alloy at different temperatures. (b) The logarithmic derivative of $<r^2>$ exhibits a minimum on the time scale of particle caging time, t_{cage}, which is on the order of a ps.

The cage size for other metallic alloys shows similar behaviour with temperature as found for $Cu_{64}Zr_{36}$ [See Appendix B] and a similar phenomenon has been discussed previously by Leporini and coworkers. [22] Although cage size found in polymer fluids has much weaker T dependence in polymer liquids than found so far in metallic GF materials, the algorithm used to identify immobile clusters is formally the same in polymer fluids and metallic GF alloys. Similarly to polymer fluids, the MSD of $Cu_{64}Zr_{36}$ (see Figure 4.1(b)) changes from ballistic-like motion [i.e., $d\left(\ln\langle r^2(t)\rangle\right)/d(\ln t) = 2$] to sub-diffusive motion when $d\left(\ln\langle r^2(t)\rangle\right)/d(\ln t) \approx 0.6$ [189], where the characteristic time at which this condition is met serves to define a "caging time".

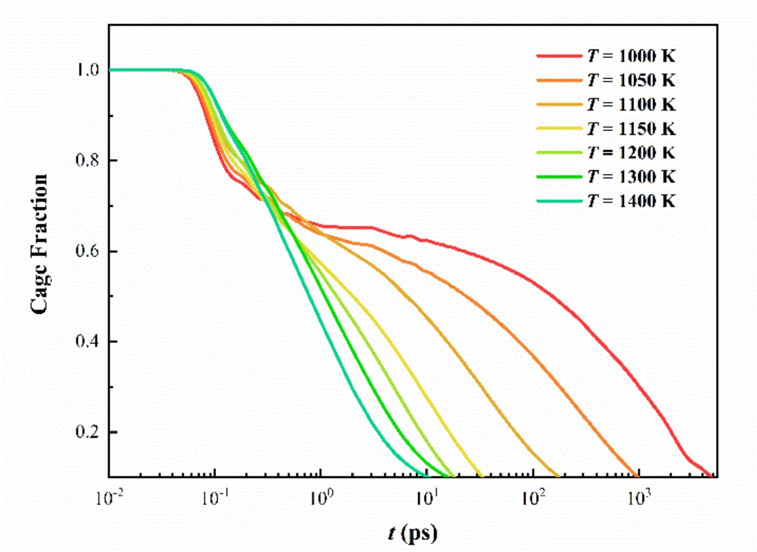

Figure 4.2 Dynamical fraction of caged particles as a function of time interval at different temperatures in $Cu_{64}Zr_{36}$ alloy.

Using this definition of cage size and caging time, we can identify how immobile particles persist in time and how they are clustered in space. In general, a cluster is defined as a group of particles of interest (either mobile or immobile) whose nearest-neighbour distance is less than the nearest-neighbour distance of the system. For instance, we choose nearest-neighbour distance to be 3.7 Å for $Cu_{64}Zr_{36}$ alloy based on the first minimum value in the radial distribution function. Next, we examine how the population of caged particles evolves as time interval increases at different temperatures. It is expected that the majority particles will be initially "caged", but as time passes particles will gradually escape from these cages so that the initial population of caged particles will decrease. Figure 4.2 shows the temporal evolution of the fraction of caged particles in the systems at different temperatures in $Cu_{64}Zr_{36}$ alloy. The same analyses for other metallic alloys are shown in the SI. As expected, the time in which the fraction of caged particles persists increases upon cooling.

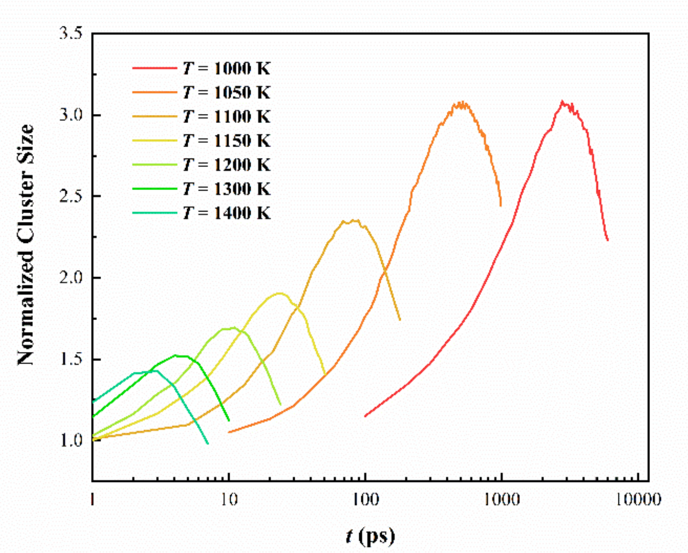

Figure 4.3 Normalized cluster size for caged particles in $Cu_{64}Zr_{36}$ alloy at different temperatures.

Once cage size has been identified, the next step is to study the dynamic behavior of caged particles. We study the average cluster size of these particles with low mobility to understand the spatially correlated tendency of these caged particles. Since the cluster size is greatly influenced by the number of caged particles, we normalize the cage particles size by the cluster size of randomly chosen particles to offset a trivial effect that clusters are larger at shorter time. Figure 4.3 shows the normalized cluster size of the caged particles as a function of time. There cluster size increases progressively in size and then a maximum that defines a characteristic time. The peak height and characteristic time increase sharply upon cooling, which is characteristic of the growing dynamic heterogeneity found in cooled liquids.

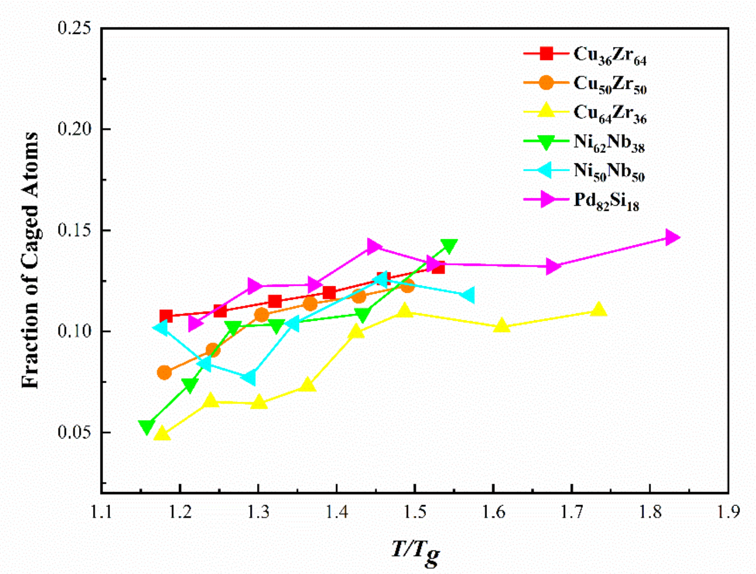

Figure 4.4 Fraction of the most immobile particles at a characteristic peak time (see Figure 4.3). For various alloy concentrations, the fraction of caged atoms exhibits similar tendency, varies from 0.05 to 0.15, however, Cu-Zr systems have larger fluctuations comparing to others. In high-temperature region, the fraction shows smaller fluctuation. For the Pd-Si alloy, the immobile particle fraction only varies from 0.13 to 0.15.

Further, we consider a more simplified version of this approach, which can still catch the characteristic peak time and amplitude of immobile clusters. The fraction of caged atoms at characteristic peak time is identified, which can be seen in Figure 4.4. The fractions are obtained by evaluating the displacements of atoms in the system at those characteristic times comparing the displacements with ${r_{\mathrm{cage}}}^2$. In general, this characteristic fraction of caged particles increases with temperature; however, this tendency becomes less distinct at higher temperatures. As the temperature increases, atoms tend to be more active, i.e., most of the atoms have jumped out of the cage and become mobile, or more liquid-like. Regardless of temperature and material type, the fraction of caged particles at characteristic time seems to be on the order of 10 % ± 5 %.

Next, we will recalculate the temporal evolution of cluster size for caged particles by only considering the fraction of the most immobile particles obtained at the characteristic peak time. At a given temperature, a fixed fraction of caged particles (see Figure 4.4) is used to calculate the immobile cluster size at any given time t. Following Starr et al. [55], we define the average immobile cluster size $\langle n_I(t)\rangle$ at time t, and mathematically as, $\langle n_I(t)\rangle = \frac{1}{N_C}\sum_{i=1}^{N_C} n_i(t)$, where N_C is the total number of immobile clusters and $n_i(t)$ is the cluster size of i^{th} immobile cluster at time t. Figure 4.5 shows the normalized average immobile particle cluster size as function of t for the $Cu_{64}Zr_{36}$ alloy. We see that $\langle n_I(t)\rangle$ peaks at a characteristic time t_I that increases upon cooling; the peak height also grows on cooling, indicating an increase in the positional correlations between the immobile particles.

Our previous study has shown that an apparent relationship between the immobile particle and atomic local structure in CuZr metallic glasses [28] based on a Voronoi tessellation of the liquid structure, a widely utilized framework for analyzing atomic local structure in metallic glasses and other liquids. In the SI, we performed a similar analysis (which is not the focus of the current work) to check the generality of a correlative relationship between dominant Voronoi cell types and the least mobile particles. Although there is some overlap in these particle populations, we conclude that there is no general relationship between Voronoi type and local mobility. The search for a structural indicator of local mobility thus continues.

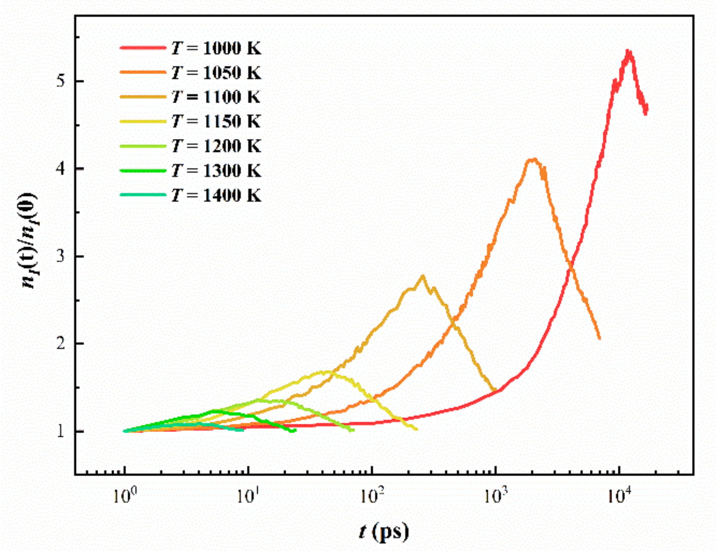

Figure 4.5 Dynamical cluster sizes for immobile particles $\langle n_I(t) \rangle$ at different temperatures for $Cu_{64}Zr_{36}$ alloy. The data are normalized by their value at $t = 0$.

4.3.2 Spatial and Size Distribution and Fractal Geometry of Mobile and Immobile Particles

Next, we will examine geometrical properties of immobile clusters and mobile particles in metallic glass alloys and make a comparison with polymeric glass-forming liquids. Based on our previous study, the mobile particles were identified by atomic displacement $a < \left| r_i(t^*) - r_i(0) \right| < b$ at t^* [the time at peak non-Gaussian parameter, $\alpha_2(\Delta t)$; See Eq. (2)], where the parameters a and b are determined from the second peak in the self-part van-Hove correlation function $G_s(r, t)$ at t^*. [50] (A brief description of how to determine the mobile particles using self-part van Hove correlation function has been provided in Appendix B). Atomic configurations of typical mobile and immobile clusters in $Cu_{64}Zr_{36}$ at 1000 K are shown in Figure 4.6(a) and 4.6(b).

Apparently, both mobile and immobile particle clusters grow quite extensively at this temperature. To further examine the geometrical structure of mobile and immobile particle clusters, we calculate the fractal dimension d_f using the relation, $n \sim R_g^{d_f}$, where n is the number of particle clusters and R_g is the radius of gyration of a given cluster. For a given cluster, the radius of gyration was defined as $R_g^2 = \frac{1}{2N}\sum_{i,j}(r_i - r_j)^2$, where N is the total number of particles in the cluster and r_i and r_j are the position of the i^{th} and j^{th} particles. The fractal dimension, d_f, varies between 2.5 and 2.8 in the temperature range we studied with an average number of $d_f \approx 2.7$ for both mobile and immobile clusters [see the inset of Figure 4.6(c) and 4.6(d)]. This fractal dimension value confirms that the mobile and immobile clusters are similar to values for randomly branched equilibrium polymer in 3D, which is also consistent with previous estimates of for the immobile particle clusters in polymeric GF liquids. [55]

The data point for the lowest temperature in the inset of Figure 4.6(d) is suggestive of a tendency of the fractal dimension d_f of the immobile particle clusters to approach 3 at low T. This uncertain trend potentially has significance in relation to the Random First Order Transition Theory (RFOT) [190], which predicts that the dynamic heterogeneity in the form of immobile particle clusters ("entropic droplets") should form "compact" clusters upon approaching the glass state, i.e., $d_f = 3$. However, a previous study of d_f of the immobile particles in polymer melts by Starr et al. [55] showed no tendency for d_f to approach 3 even at temperatures well below the crossover temperature of glass-formation, T_c, so that the tendency of the immobile particles to become compact at low temperatures does not appear to be general. Moreover, d_f estimates for both the immobile clusters (Figure B.7) and symmetric Voronoi cell clusters defined by locally preferred packing (Figure B.12) for other metallic glasses are shown in SI where a gradual increase in d_f is observed as in Figure 4.6(d) upon cooling, but where this data also shows no definite tendency for the immobile particles to form compact clusters over the T range simulated. Further studies of the shape of the immobile clusters based on a consideration of the radius gyration tensor of these clusters and their apparent d_f at low T would be of interest to determine if the immobile particles ultimately become compact at temperatures near T_g. We then conclude that while immobile particle clusters might ultimately become compact at very low temperatures, the experimental uncertainties are currently too large to make a definite conclusion about such a limiting structural form of the immobile particle clusters. On the other hand, we can definitely conclude that the immobile particle clusters are *not* generally compact for T somewhat below T_c. This observation has some significance since the RFOT model [190] predicts that the immobile particle clusters should become compact for $T < T_c$. Finally, we note that there seems to be *no evidence* that the mobile particles form compact clusters at low T.

We next considered the size distribution of the immobile particle clusters, a property expected to be important for understanding stress relaxation in glass-forming liquids. Previous studies of both polymeric and the Kob-Anderson model [110] have indicated that $P(n)$ appears to approach a power law at low T,

$$P(n) \sim n^{-\tau_F} \qquad 4.1$$

and more generally $P(n)$ can be described by a power-law times an exponential cut-off which makes a more prevalent contribution at higher temperatures where the clustering is limited. [55] The cluster size distribution of mobile and the least immobile particles in Cu-Zr system at different compositions and temperatures follows this rather standard pattern of behavior, as illustrated in Figure 4.7. Apparently, both the mobile and immobile particle distributions approach the same limiting power-law scaling at low temperatures, with a scaling exponent near $\tau_F \approx 1.8 \pm 0.5$. For the Ni-Nb and Pd-Si metallic glasses, we found the mass scaling exponent to equal, $\tau_F = 1.85$

(mobile or immobile particle clusters) and a scaling exponent near 1.8 has also been observed before for the mobile particle mass distribution in superheated crystalline. [50,55] We note that τ_F for the mobile particle clusters is also consistent with the estimate $\tau_F = 1.85 \pm 0.1$ found previously in a model polymeric material, although a somewhat larger exponent $\tau_F \approx 2.2$ was found for the immobile particle clusters. [55] (Notably, the immobile particle clusters had not grown to large size in the polymer melt simulations so that the estimate of τ_F for the immobile particles in the polymer fluid is rather uncertain.) We note that a mass-scaling exponent near 1.8 is characteristic of thermodynamic systems undergoing thermo-reversible association into branched polymers. [55,191,192] We conclude that the clustering of mobile and immobile particles in GF metallic and polymeric GF liquids is strikingly similar so the particle systems exhibiting self-assembly of branched polymers at equilibrium. We next confirm that this correspondence also holds for the fractal geometry of the mobile and immobile particle clusters.

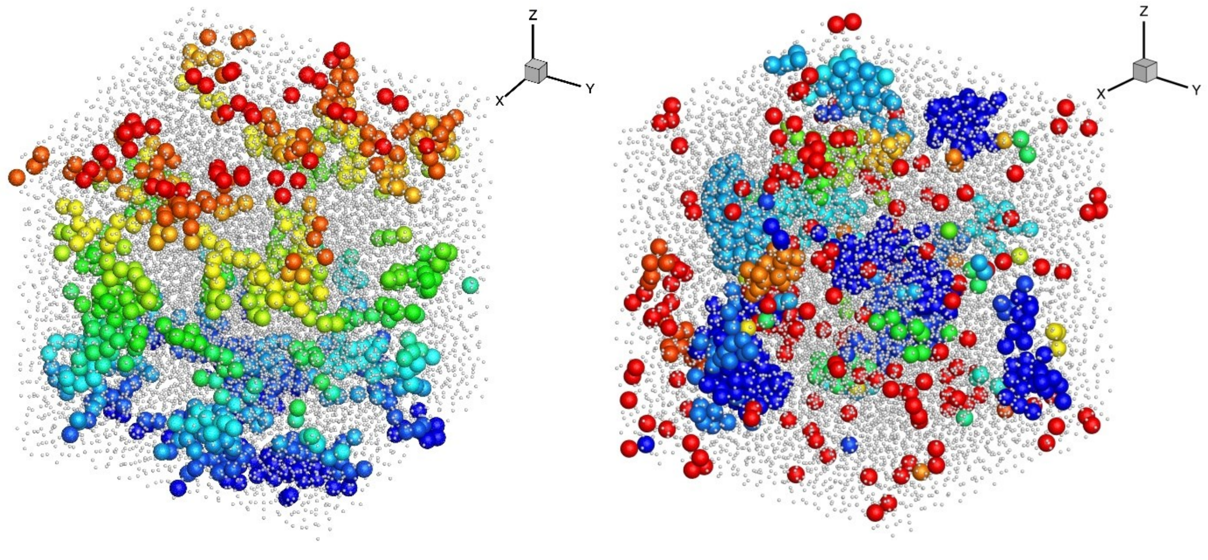

(a) (b)

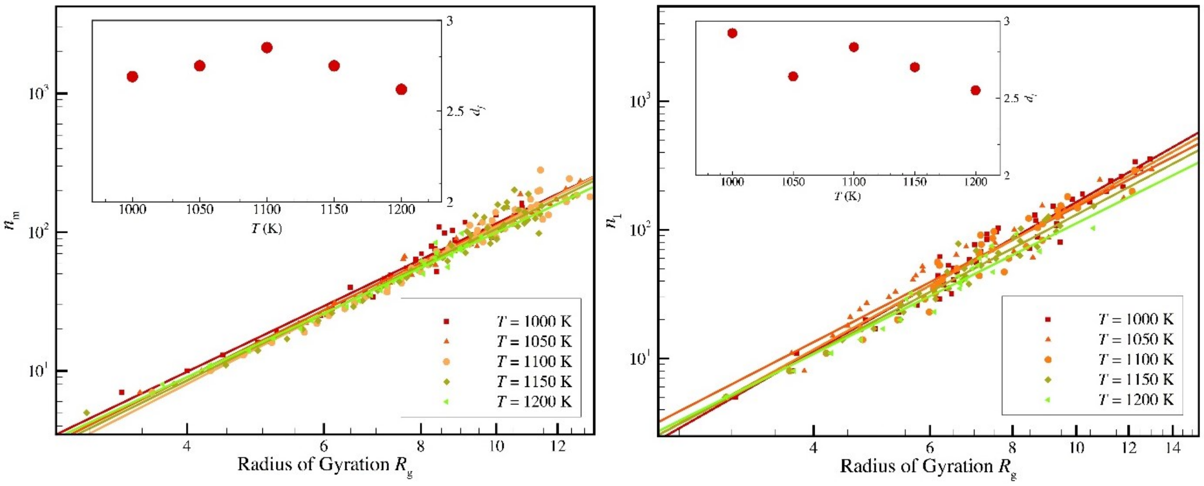

(c) (d)

Figure 4.6 Typical atomic configurations for mobile (a) and immobile (b) particles in $Cu_{64}Zr_{36}$ at 1000K. Different colors represent different clusters. Scaling of mobile (c) and immobile (d) cluster radius of gyration R_g with its mass n, $n \sim R_g^{d_f}$ in the $Cu_{64}Zr_{36}$ alloy. The inset shows that the fractal dimension, d_f, does not vary significantly with T, i.e., $d_f \approx 2.7$. This fractal dimension number confirms that the mobile and immobile clusters have a similar geometrical structure to randomly branched polymer in 3D, a finding consistent with previous observations on polymeric GF liquids. [55]

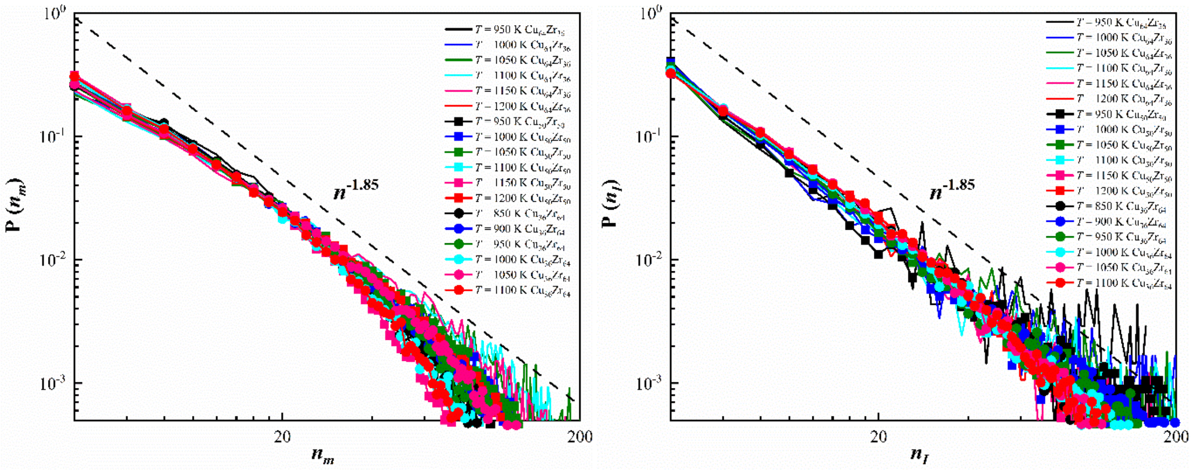

(a) (b)

Figure 4.7 The distributions of mobile (a) and immobile (b) particle cluster sizes $P(n)$. The distribution can be described by a power law. The dashed line indicates a characteristic power-law with τ_F = 1.85 and 1.8 in mobile and immobile particles, respectively.

4.3.3 Correlation between Relaxation and Dynamics Behavior of Immobile Particles

To investigate the correlation between relaxation and dynamic behaviour, first we calculate non-Gaussian parameter, α_2, which is a common analysis for mobility fluctuation in GF liquids. It can be mathematically expressed as, [67]

$$\alpha_2(\Delta t) = \frac{3\langle r^4(\Delta t)\rangle}{5\langle r^2(\Delta t)\rangle^2} - 1 \qquad 4.2$$

which is defined as the moments of particle displacement distance from their initial position at $t = 0$ after a time interval Δt. For simple Brownian motion, the non-Gaussian parameter α_2 equals zero and this quantity often serves as a basic measure of ‘dynamic heterogeneity’. We then obtain the peak time in non-Gaussian parameter, and denotes it by t^*, which is related to the diffusion of mobile particles, as we established in the previous work. [28] This characteristic time represents the time when the system is the most heterogeneous and it also indicates the "end" of β-relaxation regime and the beginning of the α-relaxation regime. [193]

An examination of the size of the mobile clusters as a function of time (the mobile particle counterpart to Figure 4.3 showing the size of the immobile particle clusters) allows for the definition of the "lifetime" t_M of such clusters by the time at which the cluster size peaks. In Figure 4.8(a), we show that t^* scales in proportion to t_M to a good approximation (Although we find a power-law 0.9, the uncertainty in our data does not allow us to discriminate our results from the approximate linear scaling between t^* and t_M previously reported by Starr et al. [55]) This approximately linear interrelationship between t^* and t_M is further supported by simulations of Xu et al. [71,130] for a coarse-grained polymer melt under constant volume and constant pressure, and for a wide range of polymer cohesive interaction and pressure variation where an apparent scaling exponent relating t^* and t_M was found to be slightly larger than 1. The approximate linear scaling relationship between t^* and t_M appears to be a robust. However, we note that the relation between t^* and t_M *does not* hold in materials having large mobility gradients, such as thin films and nanocomposites. [194] In such materials, t^* no longer provides a measure of dynamic heterogeneity, as evidenced by the fact that α_2 can deviate appreciably from 0 even in fluids in which the particles undergo ideal Brownian motion.

Mobile particles make a predominant contribution to molecular diffusion, giving rise to a *quantitative relation* between t^* and the diffusion coefficient of the component species of the fluid. [55] Douglas et al. [43] have shown that the average diffusion coefficient D and the individual atom species diffusion coefficients of the Cu-Zr can be quantitatively related to t^* and the t^* values of each atomic species, respectively (See Figure 5 of Douglas et al. [43]). Specifically, it was established by Douglas et al. that D_i / T scales inversely to t_i^*. and that D for the entire system is the concentration average of the component species. These results generalize earlier results showing this relationship for the Kob-Anderson model (see Figure 19 of Starr et al. [55]). These results indicate that we may interpret $t*$ as a "diffusive timescale. [43]

The lifetime of the mobile particle clusters becomes appreciably longer than the immobile particle in glass-forming liquids, indicating that the mobile and immobile particles correspond to two distinct types of dynamic heterogeneity. Following Starr et al. [55], we may show that these distinct dynamic heterogeneity timescales are nonetheless interrelated. Figure 4.8(b) shows the correlation between the immobile characteristic time t_I and the peak time t^* of non-Gaussian parameter for the studied alloy systems, which can be described by a power-law $t^* \sim t_I^{0.6}$. It is evident that t^* increases less rapidly than τ_α upon cooling for all alloys investigated, as found before in the simulations of Starr et al. of polymeric glass-forming liquids. Since t^* indicates a characteristic timescale associated with diffusion and mobility fluctuations t_I corresponds to the lifetime of immobile particles and the structural relaxation time (See below), we may expect t_I and t^* to exhibit a "decoupling" relationship. [121] Our previous work has shown that the characteristic timescales of diffusion and structural relaxation have a power-law relationship, $t^* \sim (\tau_\alpha)^{1-\zeta}$, where the "decoupling exponent" ζ quantifies the degree to which the Stokes-Einstein relationship ($\zeta = 1$) "breaks down" (Below we show that t_I and τ_α can be approximated in GF liquids. In the present case of Cu-Zr alloys, the decoupling exponent ζ was previously estimated to be in the range 0.26 to 0.32. [28,121] Previous simulations by Starr et al. on model glass-forming polymer liquids indicated a corresponding power-law scaling $t^* \sim (\tau_\alpha)^{2/3}$ or $\zeta \approx 1/3$. [72] Figure 4.8 then confirms that the same type of Fractional Stokes-Einstein power-law relationship exists in both metallic and polymeric GF liquids.

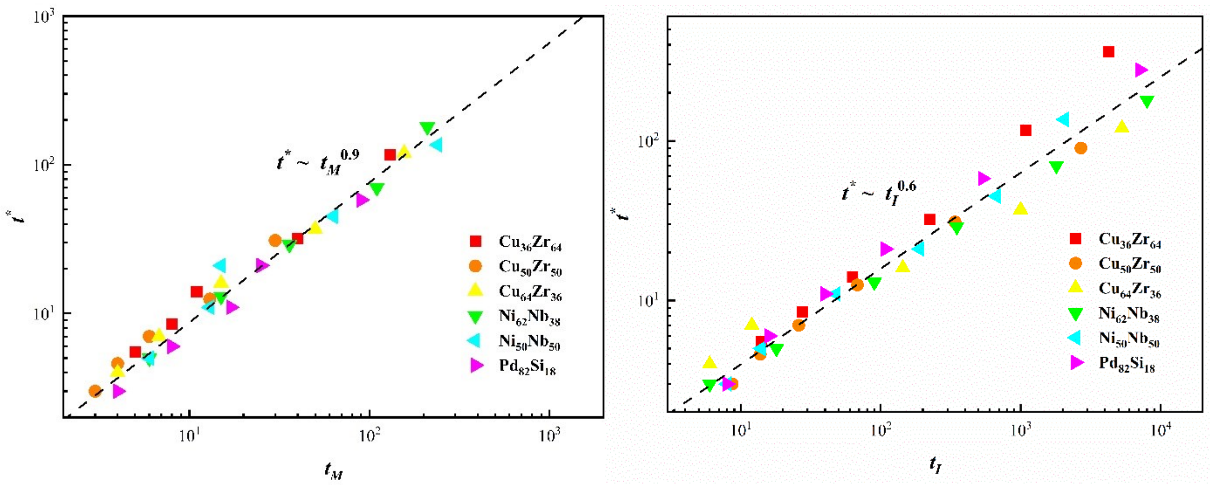

(a) (b)

Figure 4.8 (a) The correlation between the peak time of non-Gaussian parameter t^* and mobile cluster lifetime t_M. (a) Correlation between immobile characteristic time t_I and t^*. The dashed line represents the correlation can be described by $t^* \sim t_I^{0.6}$.

By performing Fourier transformation of the van Hove correlation function, the self-intermediate scattering function or "dynamic structural factor" is obtained as, [26]

$$F_s(q, t) = \langle \exp\{-iq[r_i(t) - r_i(0)]\}\rangle \qquad 4.3$$

$F_s(q, t)$ exhibits a two-stage decay, β-relaxation followed by α-relaxation. The "primary" or α-relaxation process associated with glass-formation can often be described by a stretched exponential functional form, [55]

$$F_s(q, t) \sim \exp\left[-(t/\tau_\alpha)^{\beta_s}\right] \qquad 4.4$$

where τ_α is the "structural relaxation time" and β_s is the "stretching exponent", $0 < \beta_s < 1$. In the present simulations on metallic GF liquids, β_s varies from 0.5 to 0.9 where its value gradually decreases upon lowering T. As shown in Figure 4.9, t_I is related τ_α by a power-law linking these timescales, $t_I \sim (\tau_\alpha)^\zeta$. In particular, we find $\zeta \approx 0.94$ for alloys with different composition over the entire T range simulated so that there is a roughly proportional scaling relation exists between the cluster lifetime and the structural relaxation time, $t_I \approx \tau_\alpha$.

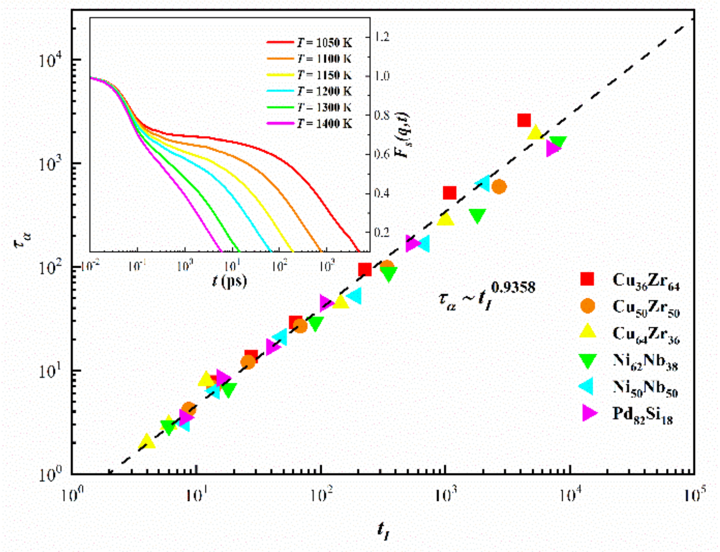

Figure 4.9 The characteristic time, t_I scales nearly linearly with structural relaxation time, τ_α. The inset shows the self-intermediate scattering function of $Ni_{62}Nb_{38}$. τ_α is obtained by fitting $F_s(q, t)$ to a stretched exponential decay, where the wave factor q is obtained from the first peak of the structure factor.

The immobile particle clusters can alternatively be quantified by an extension of the dynamic structure, the four-point susceptibility, χ_4. Starr et al. and Xu et al. [71,130,195] have shown that t_χ, the time at which t_χ peaks, and τ_α are highly correlated in polymeric glass-forming liquids, and we check whether this relation also holds in our model metallic glass-forming liquids. First, we define time-dependent self-overlap function $Q_s(t)$, [71]

$$Q_s(t) = \sum_{j=1}^{N} \omega\left(\left|r_j(t) - r_j(0)\right|\right) \qquad 4.5$$

when $\left|r_j(t) - r_j(0)\right| < 0.3\ \sigma$, $\omega = 1$, and when $\left|r_j(t) - r_j(0)\right| \geq 0.3\ \sigma$, $\omega = 0$, where σ is the average atomic spacing of a particular system and 0.3 is chosen as a typical amplitude of caged particles. This is a conventional choice of the cut-off parameter utilized before by Glotzer and coworkers in the context of discussing $Q_s(t)$ for the Kob-Anderson model, [195] and the motivation of choosing this cut-off scale for polymer liquids is discussed at length in Appendix B of Starr et al. [55] The cut-off value 0.3σ in the original work of Glotzer and coworkers [195] was chosen empirically because it maximized the peak height of $Q_s(t)$ and because this scale was consistent with cage size estimates from the root mean-square particle displacement $<u^2>^{1/2}$ at a caging time on the order of a ps. (See Starr et al. for further discussion on this point.). Notably, both Glotzer and coworkers [195] and Starr et al. [55] found that $Q_s(t)$ was relatively insensitive to the choice of cut-off when the range of cut-off values was chosen to be consistent with observed range of $<u^2>^{1/2}$ values. Despite all this discussion about the rationale for this choice of cut-off, we must admit that the fundamental reason for the choice of this "conventional" cut-off value is still somewhat obscure.

At present, we suggest that arguments by La Violette and Stillinger [196] give some physical insight into this phenomenological cut-off criterion. They note that a critical cage size approximately three times the Lindemann melting point value (typically in the range 0.1 σ to 0.15 σ depending on the potential type) should arise in liquids that should define an onset condition for liquid freezing where this critical cage size was argued to be related to the maximum basin size in the potential energy surface. We view this argument as providing a plausible physical argument for the origin of the cut-off scale. Correspondingly, we have previously defined "localized" or "Lindemann" particles by an atomic displacement cut-off of 0.27 σ in connection modeling melting of superheated crystalline Ni materials [50] and Jin et al. [197] previously estimated a somewhat smaller magnitude value 0.22 σ for particles interacting with a Lennard-Jones interaction. We then suggest a precise criterion for defining the cut-off of $Q_s(t)$ that is based on the perspective of La Violette and Stillinger [196] with adaption to glass-forming liquids; the cut-off may be defined by the value of $<u^2>^{1/2}$ at the onset temperature T_A of non-Arrhenius dynamics, a temperature often found to be near melting temperature in liquids that readily crystallize, but still well-defined in fluids [See Douglas et al. [43] for a discussion of T_A for Cu-Zr liquids based on the same potentials as in the present paper]. The basic idea here is that the cage first appears at T_A and the magnitude of $<u^2>^{1/2}$ at this temperature defines the maximum value of the caging scale. As a test of this hypothesis, we find that $<u^2>^{1/2}$ at T_A for $Cu_{64}Zr_{36}$ is 0.37 σ, which is a very plausible estimate in comparison to previous studies utilizing the heuristic criteria mentioned above. In the present paper, we utilize the *conventional value* of the cut-off 0.3 σ as a reasonable choice of cut-off, but this choice requires further consideration to understand the fundamental physical significance of this scale. We finally note that Cicerone and coworkers [198] have determined this caging scale from an experimental standpoint where a "loose cage scale" of comparable dimensions to our coarse-grained simulations was determined.

The mean-squared variance of $Q_s(t)$ then defines the (self-part) of χ_4, [58]

$$\chi_4 = \frac{V}{N^2}\left[\langle Q_s(t)^2\rangle - \langle Q_s(t)\rangle^2\right] \quad 4.6$$

In the inset of Figure 4.10, we observe a peak in $\chi_4(t)$, as observed before in the Kob-Anderson model of metallic glass liquids defined in terms of a mixture of Lennard-Jones particles [195]. We next establish that t_χ provides another method of estimating the lifetime of the 'immobile' particles.

For GF liquids, the relaxation time τ_α increases dramatically approaching to glass transition temperature, reflecting the growth of immobile clusters that persist on an increasing timescale. χ_4 provides a useful metric for quantifying this type of dynamic heterogeneity [173,199] and we illustrate the variation of this quantity as a function of time in the inset of Figure 4.10. Both the peak height of χ_4 and the time t_χ at which this peak occurs progressively increase upon cooling. A direct comparison of t_χ and τ_α for the example of a $Cu_{64}Zr_{36}$ alloy indicates an apparent power-law relationship, $t_\chi \sim (\tau_\alpha)^{\delta_\chi}$ where $\delta_\chi \approx 0.97$, which is close to the former apparent exponent estimates $\delta_\chi = 0.96$ to 0.97 for a model polymeric glass-forming liquid under a wide range of conditions. [71,130] We conclude that t_χ is proportional to τ_α within numerical uncertainty. Other metallic glass-forming liquids exhibit a similar proportional relationship, as illustrated in Figure 4.11(a). These results are to be expected from the previous observations of Glotzer and coworkers [195], who likewise found an approximate identity between t_χ and τ_α in their pioneering molecular dynamics study of t_χ for the Kob-Anderson model, and a more recent extensions of these calculations to lower temperatures and longer relaxation times by Berthier and Biroli [173] have provided further support for the robustness of this relationship between the "lifetime" of the immobile clusters (t_χ) and the structural relaxation time (τ_α). In every glass-forming liquid examined to date, τ_α and t_χ exhibit a nearly proportional relation, regardless of fluid chemistry, the presence of molecular bonding, and the temperature range considered.

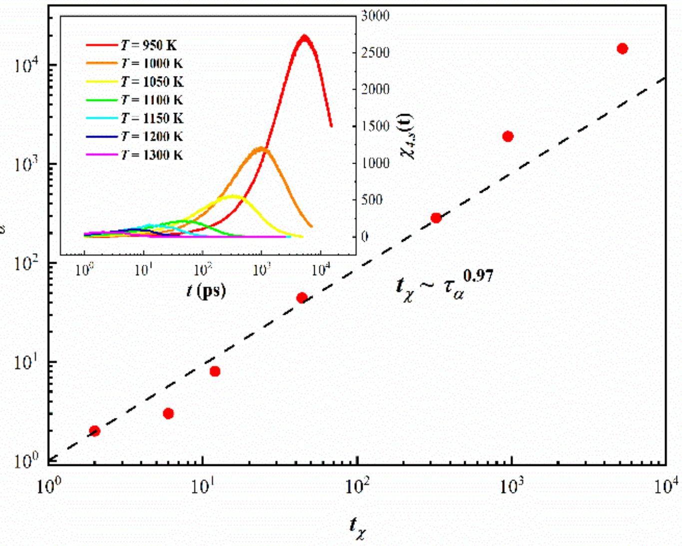

Figure 4.10 Correlation between the peak time t_χ of $\chi_4(t)$ and τ_α at different temperatures for $Cu_{64}Zr_{36}$. The line indicates that t_χ scales nearly linear with τ_α. The insect presents $\chi_4(t)$ as a function of temperature.

We also find that the immobile characteristic time t_I varies nearly proportionally to t_χ, as shown in Figure 4.11(b). This relationship is consistent with our former conclusion that the lifetime of the immobile clusters governs the structural relaxation time and with previous work [55] showing that t_χ, τ_α, and t_I correlate strongly with the lifetime of the immobile particle clusters in other materials. Evidently, the peak time of 4-point density autocorrelation function t_χ provides a convenient measure of the lifetime of the immobile clusters. We emphasize this dynamically heterogeneity timescale is quite distinct from the timescale t^* characteristic of mobile particle clusters. Glass-forming liquids exhibit multiple forms of dynamic heterogeneity which each form of heterogeneity has its own impact on the dynamics of GF liquids.

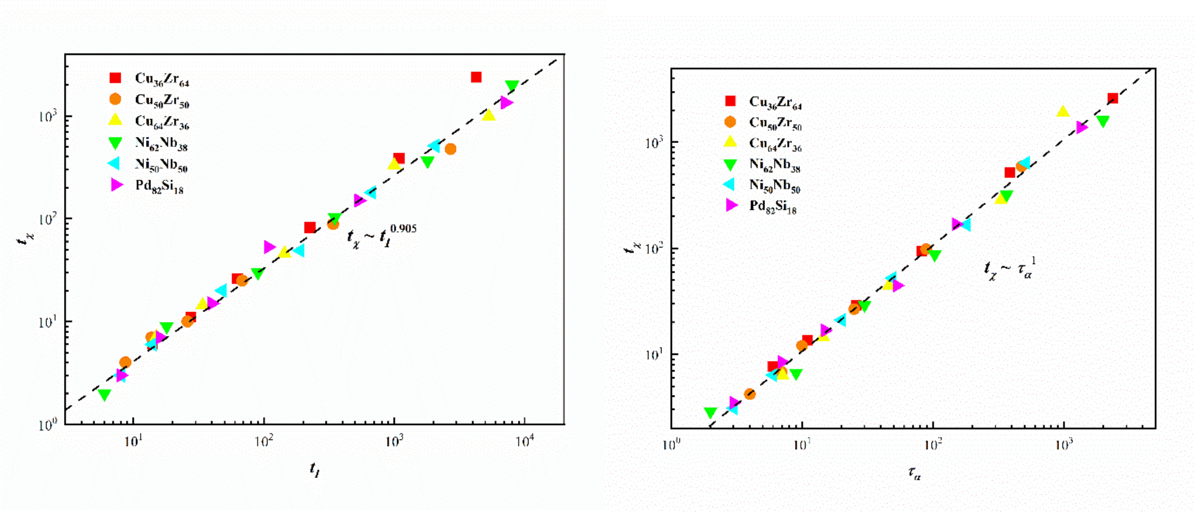

(a) (b)

Figure 4.11 Relationship between t_χ and τ_α (a), immobile particle characteristic lifetime time t_I and 4-point time t_χ (b) for systems studied in the present work.

4.4 Conclusions

We systematically examined the dynamic heterogeneity in model metallic glass-forming liquids and compared the results of our analysis with previous findings for a simulated polymeric glass-forming liquid in order to assess the nature and generality of the dynamic heterogeneity occurring in these chemically and topologically distinct molecular systems. Our primary goal was to assess the universality of the dynamic heterogeneity phenomenon and to better develop tools for enhanced quantification of dynamic heterogeneity. We summarize some of our specific findings and then make some general conclusions.

1. We utilized the algorithm developed by Starr et al. [55] to identify both mobile and immobile particles and clusters of these particles of extreme mobility in the metallic glass system and confirm this methodology can be used on different chemistry and compositions of metallic

glasses. The lifetimes t_M and t_I of the mobile and immobile particle clusters were found to increasingly separate upon cooling and to exhibit a power-law relation that mirrors the "decoupling" relation between the average atom diffusion coefficient (D) and the structural relaxation time (τ_α) of all the metallic fluids investigated. We independently showed that t^* and t_I are related to D and τ_α through the relations, $D / T \sim 1 / t^*$ and $\tau_\alpha \approx t_I$, proving insight into the origin of decoupling in glass-forming liquids. Decoupling arises from the presence of two distinct types of dynamic heterogeneity associated with mobile and immobile particle cluster formation. Notably, no decoupling (or stretched exponential relaxation) was observed in superheated crystalline Ni [50] where mobile particle clustering similar in form to glass-forming liquids and non-Arrhenius relaxation is present, but where immobile particle clusters of finite size do not exist. Together these results highlight that these distinct types of dynamic heterogeneity make different contributions to the collective properties of materials composed of strongly interacting particles.

2. We then examined the fractal dimension and the size distribution of immobile and mobile clusters. The size distributions of both types of dynamic heterogeneity exhibiting a mass scaling remarkably similar to that observed before for a model polymeric glass-forming liquids [55] and the fractal dimensions were found to be fully consistent between these chemically rather different materials. Moreover, these results for the size distribution and fractal dimension of these clusters, along with the temperature of these clusters are consistent with the known properties of particles clustering of particles to formed branched polymers at equilibrium. [55,191,192] These results support the existence of universality of the form of dynamic heterogeneity in glass-forming liquids, the primary question motivating the present study, and the previous suggestion that a self-assembly process underlies the glass-formation

process. [40,200,201]

3. We confirm previous observations indicating that the peak time t^* and t_χ for the non-Gaussian parameter $\alpha_2(t)$ and the 4-point density correlation function $\chi_4(t)$, respectively, correspond to the lifetimes of the mobile and immobile particles in our simulated glass-forming liquids. $\alpha_2(t)$ and $\chi_4(t)$ then inform on the different types of dynamic heterogeneity in the present paper. These findings support the existence of "universality" in the structure and dynamics of glass-forming liquids.
4. To better understand the origin of immobile particle clustering in terms of static fluid structure, we also examined locally preferred atomic packing in our metallic alloys based on a consideration of Voronoi cell analysis of the local geometry about all atoms in our system. We found clear evidence for atoms to adopt locally energetically preferred packing and for the close-packed Voronoi cells associated with these atoms to form branched polymeric clusters as found for the immobile particle clusters in our study, we unfortunately could not find any one-to-one relation between these populations of particles. Unfortunately, the attractive hypothesis that immobile particle clusters arise from the occurrence of locally preferred packing is simply not generally supported by our simulations. The goal of finding a relation between local static structure and dynamics in glass-forming liquids thus remains elusive.
5. Our comparison between the dynamics of polymeric and metallic glass-forming liquids also directly addresses the claim by Colmenero [181] that glass-formation in small molecule liquids is fundamentally different from small molecule glass-forming liquids. Contrary to this suggestion, we find that the dynamics of these structurally and chemically glass-forming liquids is remarkably similar.

The present paper has mainly emphasized immobile particles and the geometry and lifetime of the dynamic clusters of these particles, although we briefly consider mobile particle clusters and clusters of such particles to establish that this type of dynamic heterogeneity is distinct in nature and significance for the properties of glass-forming liquids from the immobile particle dynamic heterogeneity. Our previous simulations [28,55] have emphasized that the mobile particle clusters are themselves actually clusters of more primitive dynamical structures involving string-like collective exchange motion where the temperature-dependent average length of these "strings" is proportional to the change in the temperature-dependent activation energy for structural relaxation time, τ_α, a finding consistent with the identification of the strings with the 'cooperatively rearranging regions' of Adam and Gibbs. [36] This aspect of dynamic heterogeneity in glass-forming liquids has been established before both for Cu-Zr metallic glasses [28] and polymeric glass-forming liquids [55] so that this appears to be another general feature of glass-forming liquids.

It is our expectation that the immobile particle clusters can be decomposed, in a complementary fashion, into linear chain clusters that can support shear stress as suggested by Douglas and Hubbard [200,202] where such clusters were suggested to have great significance for understanding the universality of stress-relaxation relaxation in glass-forming liquids and the phenomenon of decoupling. [201] However, this expectation remains to be investigated by molecular dynamics simulation.

We should also mention that much of the interest in characterizing the immobile clusters in glass-forming liquids derives from the Random First Order Transition Theory prediction that the temperature dependent size of the immobile particle clusters should determine the temperature dependence of the activation free energy for relaxation and molecular diffusion in glass-forming liquids. In qualitative accord with this RFOT model prediction, Bauer et al. [203] and Flenner et al. [204] have provided, respectively, experimental and computational evidence in support of at least a qualitative relation between the growing activation energy of glass-forming liquids upon cooling and the size of the immobile particle clusters inferred from multiparticle density correlation function analyses. On the other hand, Wyart and Cates [205] have raised serious questions about the existence of any general quantitative relation between the immobile particle cluster size and the activation energy for transport in glass-forming liquids. We believe that the earlier finite system size study of Karmakar et al. [206] on a model binary Lennard-Jones glass-forming liquid provides essential insights into this proposed relationship between immobile particles and activation energy changes in glass-forming liquids that have not been sufficiently appreciated previously. In particular, Karmakar et al. found that the χ_4 function, which is heavily weighted by the immobile particle type of dynamic heterogeneity, shows large changes with system size, while τ_α exhibits a limited change in comparison to expectations for a direct relation between immobile particle size and the activation energy.

We also point out that the experimentally observed [29] change in the activation free energy of glass forming liquids usually involves a relatively small factor of about 4 ± 2 over the entire range of glass formation, while the average number of particles in either the mobile and immobile particle clusters has been found to range from a small number at elevated temperatures to a relatively large number (Clusters of mobile and immobile particles as large as 200 particles are often observed at low temperatures or high particle concentrations in the studies of glass-forming liquids; See Figure 4.7 for illustration of this phenomenon in the case of the present metallic glass simulations). This observation alone suffices to exclude either mobile or immobile particles as being identifiable with the “cooperatively rearranging regions” (CRR) of the Adam-Gibbs (AG) model. On the other hand, the average number of the mobile particles exhibiting string-like collective particle exchange motion ("strings") exhibits both a size variation with temperature, and an absolute size consistent with the observed activation free energy in simulated liquids. [29,55,128] Starr et al. [55] also observed that the average number of particles in the strings scales inversely to the configurational entropy estimated from inherent structure calculations to a good approximation, an observation again according with the heuristic AG model. The strings are the *only* form of dynamic heterogeneity identified so far that are consistent with the hypothetical CRRs of AG. In this interpretation of the hypothetical and rather ill-defined cooperative rearrangement motions that AG proposed to describe the temperature dependent activation free energy of cooled liquids is more specifically related to a sub-class of mobile particle clusters ('strings') that are characterized additionally by the simultaneous presence of particle exchange motion so that the mobile particles are clusters of more primitive clusters, strings. It is then evident from this discussion that the AG and RFOT models emphasize *qualitatively different* types of dynamic heterogeneity in glass-forming liquids so that these models cannot be considered to be basically "equivalent" entropy theories of glass-formation. We also point out that the strings show no tendency to form compact structures in liquids at low temperatures, but the existing evidence indicates that these dynamic structures tend to adopt a structure consistent with polydisperse flexible polymer chains formed by self-assembly, regardless of the chemical structure of the glass-forming liquid. [28,29,55,128] Thus, even if the immobile particles become ultimately compact at low temperatures, as suggested by the RFOT model, this would have no direct implication for the strings. Of course, the degree on the universality of the strings for other glass-forming liquids should be investigated further, along with the fundamental origin of this form of collective motion in the cooled liquids.

We conclude that glass-forming liquids evidently exhibit general characteristics that can be expected to explain the "universal" phenomenology of their material properties. Both metallic and polymer glass-forming materials exhibit a multiplicity of scales in the intermolecular interaction potential that frustrates crystallization and ordering by default takes the form of transient formation of particles into clusters in which the particles only exhibit local ordering. We expect this to be a universal property of glass-forming materials. The formation of locally well-packed and energetically preferred clusters leaves the surrounding particles in a relatively frustrated state that leads to collective motion [28], a situation akin to particles in the grain boundaries where atom motion likewise can be highly cooperative for the same reason. [45] We expect this is another general aspect of glass-forming liquids. Of course, chain connectivity, stiffness, and changes in the cohesive interaction and pressure, modulate the degree of packing frustration in these condensed materials, and thus the fragility of glass formation, and other specific aspects of glass-formation, are characteristic of polymeric fluids as a class, and we briefly comment on this aspect of glass-formation in molecular versus polymeric fluids.

Molecular bonding is a defining feature of polymeric materials that accounts for the relatively high fragility of many glass-forming liquids in comparison to metallic glass and small molecule liquids. Molecular bonding gives rise to the emergence of molecular rigidity, which, in turn, alters the efficiency of local molecular packing. The entropy theory of glass formation [207,208] allows for the quantification of these packing effects arising variations of molecular structure and rigidity, pressure etc. and their effect on the dynamics of glass-formation. In particular, increasing the relative rigidity of the chain backbone relative to the side-groups, or vice versa, leads to significant enhancements of the (segmental) fragility of glass-formation for polymers having the same van der Waals interaction strength under the same constant pressure conditions.[208] These general trends have been confirmed by the group of Sokolov and coworkers.[209] Chemical bonding and the control of the topological structure of the polymer[210] modulate molecular rigidity and packing efficiency in the melt, allowing for the *tuning* of the glass transition temperature and fragility over a large range, a phenomenon that accounts for many of the unique properties of polymer materials. In metallic glasses, the packing frustration and fragility can be tuned through varying metallic composition, but the range of fragility variation tends to be much more limited and these materials also exhibit an inherent tendency towards phase separation and crystallization processes.

5. The Initiation of Shear Band Formation in Deformed Metallic Glasses from Soft Localized Domains

5.1 Introduction

MGs have been intensively researched as a promising new class of materials for many applications, but the inherent brittleness of these materials, and other technical problems have limited their development [211–214]. In particular, MGs tend to readily undergo catastrophic fracture following the formation of highly localized SB in the material in which deformation becomes highly localized, precipitating material failure [211–213]. Given the practical importance of SBs in MGs, the process and mechanisms of SB formation have been extensively studied by both experimental and computational methods [215–218]. Experimental methods of studying SBs normally cannot resolve many aspects of SB formation and evolution because the nanoscale width and rapid evolution of these structures make measurements extremely challenging, and the long computational timescales required, and the inherently low temperatures characteristic of MG materials make the problem of studying SB formation and evolution also extremely difficult from a simulation standpoint. Since the timescale of the process is extremely short, and the length-scale is initially on the order of nm, we try to gain insights in SB formation and evolution through MD simulation since this method at least has the requisite time and spatial resolution for studying this phenomenon.

Shear bands form spontaneously in MG materials at temperatures well below their glass transition temperature T_g where molecular diffusion is unmeasurably slow by simulation, yet the formation of shear bands hints at the emergence of appreciable mobility in the material under deformation. The nature of 'mobility', and how to quantify it, under conditions where one cannot normally estimate the rate of molecular diffusion are clearly basic issues that need to be addressed. There is also a universal geometrical character to the SBs themselves that invites theoretical explanation. SBs in diverse materials take the form of ribbon-like thin regions that arise from the emergence of localized layer-like regions of the material in which relatively large strains arise, hence the term 'shear band'. This is the primary deformation mode of metallic glasses [219] that is of recognized critical importance for the mechanical properties of these materials in relation to their performance in applications. There is a general view in the MG community that if the mechanism of shear localization could be understood, along with the subsequent formation of mature SBs, then this knowledge might be used to engineer tougher MG materials that are less prone to this elastic instability. It is this ultimate goal of developing design rules for making metallic glasses for many applications that animate our work. It is notable that many aspects of SB formation in glass materials are remarkably insensitive to the chemical nature of the material. For example, the observations of Argon et al. [220] on shear banding in polystyrene in its glass state are remarkably similar to those for metallic glasses and the similarity between shear banding in polymeric and metallic glass materials has also been emphasized by Shavit and Riggleman [221]. This commonality in the phenomenology of shear band formation in such different materials gives us hope that there are general principles to be discovered about SB formation and yield in glassy materials that are invariant to the material substance.

Our own approach to this problem is heavily informed by ideas and computational tools derived from quantifying mobility fluctuations and collective motion arising in GF liquids as these materials approach their glass transition from *above*. It is initially seemed reasonable to us to suppose that these dynamical structures, and atomic clustering associated with these mobility fluctuations, become kinetically trapped in the glass state. In the previous simulations, we and others have found [28,49] that the atoms of MGs and other model GF liquids tend to form string-like clusters of atoms corresponding to locally energetically preferred configurations and that the particles in these clusters tend to be relatively immobile in the fluid state under conditions in which the diffusion coefficients of different types of atoms in the material can be quantified by simulation. Ma [222] has recently provided a detailed review of locally preferred packing in metallic glass materials and Ding et al. [223] discuss this local packing geometry for the specific MG material studied in the present work. Many simulations have also shown that these relatively well-packed particles having an energetically preferred spatial configuration can be identified by a Voronoi analysis of the local environment of the atoms where it is found that the Voronoi cells are organized in highly correlated polymer-like structures in space. This is clearly a kind of topological 'ordering' process, as evidenced by the corresponding parallel drop in the fluid entropy in polymerizing systems and GF liquids [40], so that the material structure is not really 'random'. Of course, not all the atoms can participate in this locally preferred packing, and the atoms in the not so well-packed regions are energetically frustrated [222] in a fashion highly analogous to the 'amorphous regions' in polycrystalline materials [45]. We have found in our previous simulations that the dynamics of both metallic and polymeric GF liquids exhibit dynamic interpenetrating structures in which particle mobility is excessively high and low in these regions, respectively, and, in the liquid state the particles undergo a constant exchange between these dynamical states. We may then expect some remnants of this dynamical and structural heterogeneity of the liquid state to persist in the glass state below the glass transition temperature, T_g. Under deformation conditions, where mechanical rather than thermal energy should 'activate' particle motion, and we also expect active dynamic heterogeneity to re-emerge upon increasing stress until the material locally 'melts'. The present work pursues how 'dynamic heterogeneity' might influence SB formation in a model Zr-Cu metallic glass material. We naturally bring the tools that we previously brought to studying metallic GF liquids to study the dynamics of our simulated MG in its glass state. We note recent work has shown that deforming glass-forming materials leads to changes roughly equivalent to increasing T [224] and another goal of our work is check this possibility.

The concept of dynamical heterogeneities has independently been introduced into phenomenological descriptions of the dynamics of MG and other glass materials. In particular, shear transformation zones (STZs) have been invoked to model the deformation processes of MG, these proposed structures being roughly the 'defect' counterpart of dislocations in deformed crystalline materials in their significance of the mechanical properties such as strain hardening, etc. The basic 'function' of the proposed STZs is to enable localized deformation in the material that allows macroscopically deformation through the action of numerous hypothetical regions of this kind spread throughout the material. Extensive research on metallic glasses has revealed that the relaxation process obtained from fitting models of the mechanics, with local properties assumed for STZs to mechanical measurements, [225] has indicated that the activation energy of the STZs is thermally activated where the thermal activation energy is highly correlated in general with the JG relaxation process. It is widely appreciated that this relaxation process is the dominant relaxation process in mechanical and dielectric measurements of materials in their glass state [226]. This is highly encouraging from the standpoint of the present study because we have recently found that the JG relaxation process in model Al-Sm metallic glass materials can be quantitatively described by collective motions that have been observed in GF liquids [227,228]. There would then appear to be some prospect of obtaining a more fundamental understanding and precise specification of the rather abstract STZs. Recent works [229–231] have indicated that well-defined elastic heterogeneities in the stress field develop in deformed metallic glasses and we may expect the heterogeneities that we tentatively identify with the STZs to likewise exhibit stress multipole interactions. We hope to consider this problem in future work in simulations dedicated to elucidating this hypothesis.

Recently, Cao et al. quantified the network of icosahedral clustering mentioned and suggested its important role in the initiation of shear band formation [225]. This work reminds us that it is the organization of the locally well-packed particles in the material that is ultimately responsible for the 'strength' (shear modulus) of the material and the alteration of these structures under deformation can be expected to be an important contribution to the deformation dependence of material properties, in addition to alterations of the less well-packed regions exhibiting relatively high local deformability. Evidence of the importance of the deformation of these immobile particle clusters was emphasized in the magnitude of deformation-induced acceleration of structural relaxation in glass-forming liquids under steady shear conditions [224]. Both classes of 'dynamic heterogeneity', highly mobile and immobile particle clusters, can be expected to contribute to changes of materials properties under deformation.

One of the general trends that arises in liquids as they are cooled towards their glass-transition is a general increase in the scale of collective motion as the shear rigidity tends to increase [128] and this tendency at fixed T can be expected to be contravened by material deformation. This tight interrelationship between cooperative motion and rigidity makes measures of rigidity particularly useful in the quantification of the dynamics of condensed materials. Since shear bands arise locally in the material, we are interested in local measures of rigidity that lend themselves to measurement and quantitative determination by simulation. The Debye-Waller factor, $\langle u^2 \rangle$ has been proposed as a measure of local material stiffness that has a highly predictive value in relation to understanding the material dynamics. This quantity is defined as the mean square displacement $<r^2>$ after a fixed 'caging' or decorrelation time t_0 characterizing the crossover from ballistic to caged atomic motion in the liquid dynamics [43]. $<u^2>$ is considered a 'fast dynamics' property since t_0 is typically on the order of a ps in molecular and atomic fluids. Remarkably, this dynamical property defined on this very short timescale has shown great value in estimating the structural relaxation time τ_α on the timescale at the glass transition temperature T_g where τ_α is typically on the order of a min. This type of interrelationship has been explored in a range of materials and thus has some generality [224,232–236]. We note that previous studies have focussed on $<r^2>$ and various measures of local effective shear modulus in connection with the quantification of the onset of SB formation [237,238], but we are not aware of any previous study based on $<u^2>$.

In an early simulation study of $<u^2>$ in relation to relaxation in GF liquids, Starr et al. established a near proportionality between $<u^2>^{3/2}$ and 'rattle free volume' $<v_f>$, defined by the volume explored by the particle rattling about in a cage defined by the surrounding particles in the material [2,239]. Note that the inertial energy of the particles is a significant contributor to this type of free volume so that this quantity is quite different, even qualitatively in some cases, from estimates of 'free volume' based on material 'structure', e.g., estimates based on Voronoi volume, etc. We may expect $<u^2>$, which provides a useful local measure of stiffness, as a well as local mobility in terms of the mean amplitude of motion ('dynamic free volume'), to provide a useful metric for studying the emergence of local soft spots in deformed materials and the coalescence of soft regions into a shear band. Our previous studies of GF liquids have repeatedly shown that $<u^2>$ can inform on local mobility gradients that are not apparent structurally [145]. Previous work has shown that the magnitude of $<u^2>$ is often dominated by the motion of a relatively small fraction of particles in the system exhibiting string-like collective motion [6], and these dynamic structures are candidate structures for describing the STZs noted above. We may then expect to gain some important new insights in the formation and evolution of shear bands in deformed MGs by simply observing the evolution of the field of values of $<u^2>$. We find that this is indeed the case.

In the current paper, we examine the initiation and evolution of the formation of SB in $Cu_{64}Zr_{36}$ MG materials under uniaxial tensile loading with different sizes and temperatures. First, using commonly used local von Mises strain measure, we observed numerous areas with relatively large local strain spontaneously arises as the stress increases. Those areas grow and coalescence in particular band upon the stress approaching the critical value for the formation of SB, phenomenologically resembling early and late stage of spinodal decomposition. We then examined whether the common dynamic heterogeneity types found in the cooled GF liquid approaching the glass transition from above also exist in the glass state. Since the systems do not have pre-existing regions with stress concentration, we found that regions with relatively large $<u^2>$ first appeared simultaneously at many places within the material, but these regions evolved in their organization into a shear band become concentrated into a band-like domain. We find that when the SB has fully formed, almost all the particles inside these regions are 'interfacial-like' (i.e., atomic mobility is equivalent to the atomic mobility in the interfacial region at the undeformed state), which enables the relatively facile deformation of these regions. We then define a precise local measure of material stiffness to investigate the initiation of shear band formation. The local stiffness distribution in the SB region and the whole system both approach to the distribution of the interfacial region at the undeformed state. In particular, as the material strain increased, the fraction of mobile particles progressively grew at relatively random positions within the incipient shear band region. In addition, we found that the van Hove function describing atomic displacement in a highly deformed metallic glass exhibits rather typical behaviour for the type of elastically turbulent system observed during the formation of SB.

5.2 Simulation Methodology

Molecular dynamics simulations were implemented to examine the formation of shear band in $Cu_{64}Zr_{36}$ metallic glass systems. The MD simulations were carried out using Large-scale Atomic/Molecular Massively Parallel Simulator (LAMMPS), developed by the Sandia National Laboratories [99]. The atomic interaction in metallic glasses systems was described by semi-empirical potentials optimized to reproduce the measured static structure factor and other equilibrium properties of Cu-Zr alloys [58]. It has been demonstrated in previous studies that this potential provided reliable descriptions of both structural and dynamic properties. In the present study, the representative alloys $Cu_{64}Zr_{36}$ were chosen based on extensive research and studies show that this alloy possesses good glass-forming ability near the eutectic points of the alloys.

Next, we describe the simulation methods for MD simulations of metallic glasses. First, we chose four different length scales of $Cu_{64}Zr_{36}$ alloys: (180 × 30 × 30) Å (≈ 10, 125 atoms), (180 × 90 × 30) Å (≈ 30 375 atoms), (300 × 150 × 30) Å (≈ 84 375 atoms), and (600 × 300 × 60) Å (≈ 675, 000 atoms) in X, Y, and Z directions. For the latter three simulation cells, the dimension in X and Y was chosen to keep the aspect ratio constant. Taking (600 × 300 × 60) Å as an example, we begin with a perfect Cu single crystal containing 675 000 atoms. Then 36 % of the Cu atoms are randomly replaced by Zr atoms. The mixture was then heated from 300 K to 2000 K and kept at 2000 K for 5 ns to achieve a structural homogeneous glass-forming liquid. After that, the system was cooled down to 50 K in 19.5 ns, given a cooling rate of 100 K/ns.

During this process, NPT (constant number of atoms, constant pressure, and constant temperature) ensemble was implemented with zero pressure and periodic boundary conditions. The constant pressure was controlled by the Parrinello-Rahman algorithm [63], and temperature was kept constant using Nose-Hoover thermostat method [61,62]. After obtaining the metallic glass sample, 30 Å vacuum spaces were added on both sides along the Y-axis.

The deformation of the sample was achieved by loading the sample under uniaxial tensile loading along X-axis using a constant strain rate of 1×10^7 / s to 15 %. Periodic boundary condition was applied on the X and Z-axis, while the free surface condition was applied on the Y-axis. The simulations were first carried out at 50 K to guarantee the formation of the shear band. To examine the temperature influence on the deformation, three more temperatures at 200 K, 300 K and 400 K were carried out on the system with h = 300 Å. Same strain rate was applied with different temperatures. Atomic configurations were saved every 1 ps for future analysis.

5.3 Results and Discussion

5.3.1 Uniaxial Tension Test on $Cu_{64}Zr_{36}$ Materials Having a Range of Thicknesses

Figure 5.1 (a) shows stress-strain curves of $Cu_{64}Zr_{36}$ with four different thicknesses h = 30 Å, 90 Å, 150 Å, and 300 Å. For h = 90 Å, 150 Å, and 300 Å, stress overshot and dramatic drop have been observed after roughly strain at 7 %, which is known as a characteristic feature of localized deformation, similar to the findings in other literature [225,240,241]. After the stress drops, fluctuations in the stress-strain curves become noticeable. We find below that this phenomenon is related to an intermittent softening and stiffening of the shear band region. These soft areas have been identified as shear transformation zones in other literature [242]. Eventually, one dominant SB formed and led to a catastrophic failure in the sample.

The atomic shear strain η^{Mises} was implemented to monitor the formation of the shear band, which was calculated using the equation[243]:

$$\eta^{Mises} = \sqrt{{\varepsilon_{xy}}^2 + {\varepsilon_{xz}}^2 + {\varepsilon_{yz}}^2 + \frac{\left(\varepsilon_{xx} - \varepsilon_{yy}\right)^2 + (\varepsilon_{xx} - \varepsilon_{zz})^2 + \left(\varepsilon_{yy} - \varepsilon_{zz}\right)^2}{6}} \qquad 5.1$$

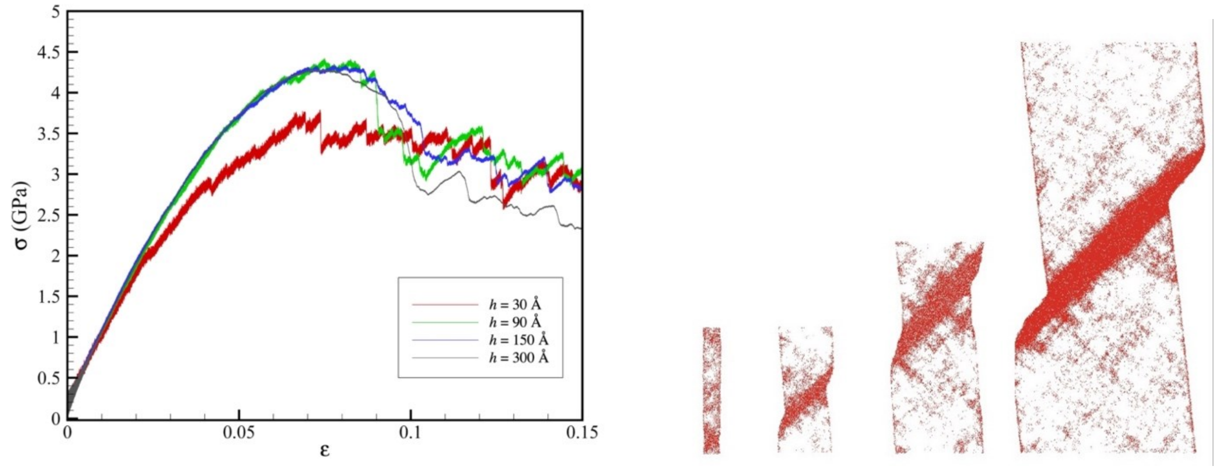

(a) (b)

Figure 5.1 Stress-strain curves (a) for $Cu_{64}Zr_{36}$ metallic glass materials under uniaxial extension at 50 K for films having a range of thicknesses and the onset of shear band formation. (b) Deformation maps of $Cu_{64}Zr_{36}$ with different thicknesses at $\varepsilon = 15$ %. The red atoms are those with the von Mises local strain higher than 0.2. Corresponding from left to right: thickness h = 30 Å, 90 Å, 150 Å, and 300 Å. The characteristic angle of the shear band near 45° corresponds to the direction in which the resolved shear stresses are maximum in this mode of deformation based on Schmid's law [244].

As shown in Figure 5.1 (b), atoms with the atomic shear strain larger than 0.2 have been marked as red to identify the deformation mode. Also, a non-localized deformation has been observed in the deformation map with $h = 30$ Å, as well as in the stress-strain curves having no overshoot. This confirmed with the critical thickness $t_c = (3.33 \pm 0.20)$ nm (note the variation was estimated based on multiple simulations) for $Cu_{64}Zr_{36}$ alloys proposed by Zhong et al. [240,241] that systems with smaller dimensions than the critical thickness exhibited a deformation transition mode from localized deformation to non-localized stress-induced uniform flow.

A series of snapshots of local von Mises strain directly demonstrating the formation of shear band is shown in Figure 5.2. The sample was under uniaxial tensile loading without a stress concentrator. Von Mises local η^{Mises} defined in eq. (5.1) were implemented to monitor the formation of shear band. The cut-off radius for von Mises strain calculation was chosen as the first minimum of the pair distribution function. As observed by Cao et al., systems without pre-existing stress concentrations tend to show multiple areas that undergo larger local deformation [225]. The shear band does not seem to initiate its growth from the surface, and then propagate along a 45° direction (maximum resolved shear stress direction) from this interface as we initially anticipated. (Below, we show that the dynamics of the interfacial region does have an impact on the onset of SB formation.) Instead, the SB gradually evidently builds up from a gradual accumulation of soft regions within the SB region. Once the band has fully formed in this way, it begins to widen and further soften, a pattern of growth that superficially resembles early and late stage of spinodal decomposition where local density or composition fluctuations first form spontaneously in local regions of the material, and this structure coarsens in time in a later coarsening stage. We see below, however, that the softness of the interior of the SBs closely matches the boundary of the material, and that the critical condition for SB formation is apparently related to a ‘critical’ condition at which this confluence of $<u^2>$ values occur. Thus, even if the SB is not 'nucleated' from the boundary the mechanical properties of the boundary and interfacial dynamics of the material appear to be highly relevant to the development of SBs.

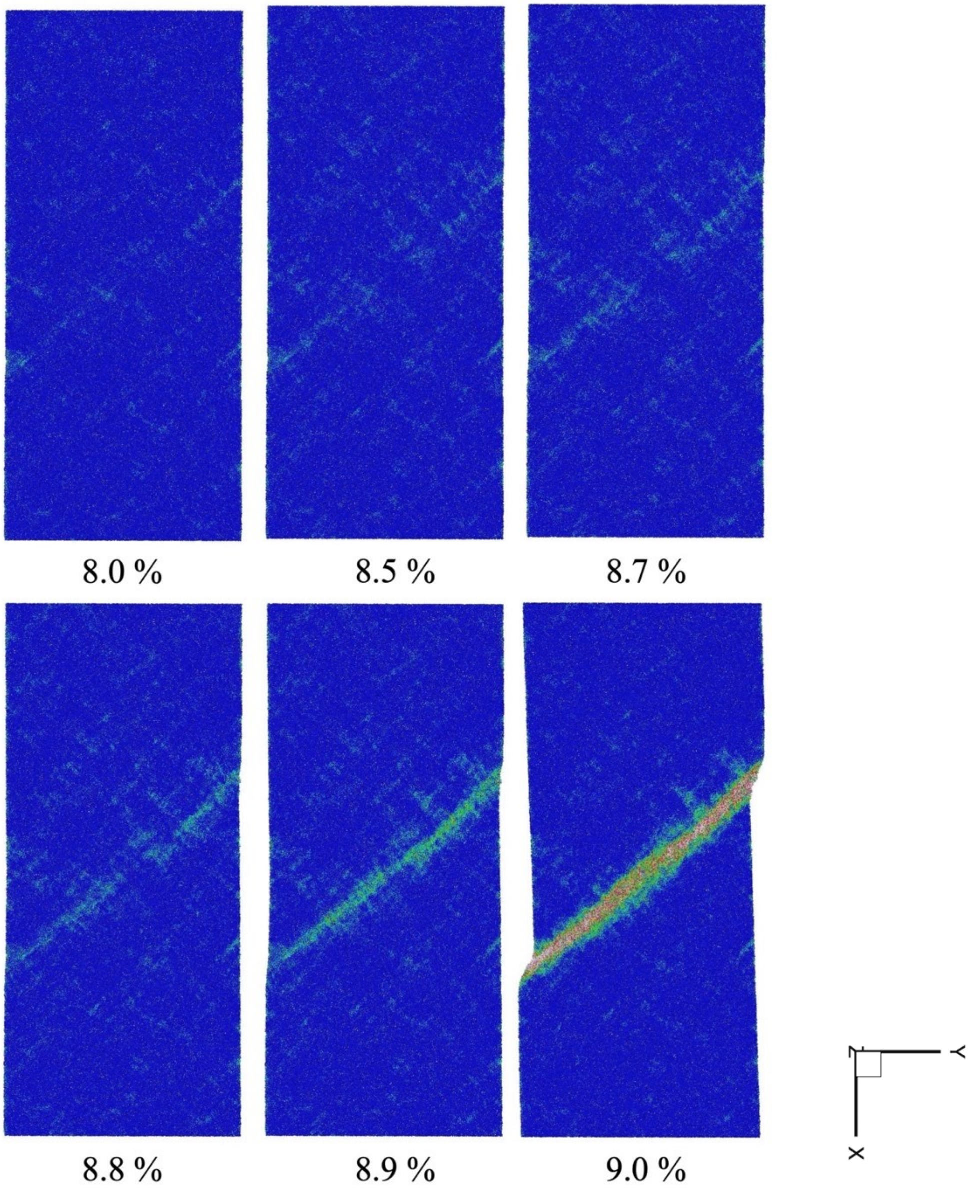

Figure 5.2 Snapshots of von Mises strain showing the formation of the shear band. Corresponding to strain ε = 8.0 %, 8.5 %, 8.7 %, 8.8 %, 8.9 %, and 9.0 %.

Based on Griffith's theory, the propagation of shear band only succeeds when the elastic strain energy causing by the propagation is larger than the formation energy of the two free surfaces [245,246]. While the samples possess no pre-existing stress concentrator, fluctuations have been observed in terms of local strain. When the strain equals $\varepsilon = 8.0$ %, multiple areas with relatively large von Mises strain appeared within the sample. We believe that these areas are mainly responsible for mediating plastic deformation. When we increased the strain, these areas would soften or harden during the process. Eventually, one dominant shear band develops in which deformation becomes predominantly localized.

5.3.2 Quantification of Local 'Mobility' and Relaxation in the Glass State

At low temperatures in the metallic glass state, atomic diffusion is extremely slow and other mechanisms can be expected to mediate the structural relaxation process. The nature of these processes was not a priori clear to us when we started our investigation, so we first examined the dynamics of single particle displacement and collective atomic motion to determine what features are common to the cooled liquid regime approaching the glass transition from above or whether any entirely new modes of motion arise in the glass state. It is also seemed relevant to determine how the dynamics in the MG state depended on *T* or whether the material properties strongly depended on the history of material preparation. The tentative answers to these questions guide how we analyze the onset and dynamics of shear banding when the material is subjected to deformation at low *T*.

We begin our analysis by considering the average MSD $<r^2(t)>$ of all atoms in our system as a function of time *t* for different temperatures in Figure 5.3(a). The MSD is defined as $\frac{1}{N}\sum_{i=1}^{N}\{[x_i(t)-x_i(0)]^2+[y_i(t)-y_i(0)]^2+[z_i(t)-z_i(0)]^2\}$, where $\left(x_i(0),y_i(0),z_i(0)\right)$ and

$(x_i(t), y_i(t), z_i(t))$ are particle i's initial and final positions after time t, respectively, and N is the number of atoms. Notice the drift motion of all atoms due to the elastic deformation upon loading is subtracted. The $<r^2(t)>$ at a later time was calculated using the atomic position at ε = 1 % as a reference and calculated up to ε = 2.9 % (or equivalently 1.9 ns based on the current strain rate). It is ideal to use the configuration at ε = 0 % as the initial position for MSD calculation. Due to some unknown reason, the material exhibits stress exhibits fluctuations near 0 % strain. In order to avoid uncertainty in the calculation of MSD due to stress fluctuation, we instead choose the configuration at ε = 1%, where we believe it does not significantly change our conclusion. We believe that the stress fluctuation at low strain region was mainly a result of significant residual stresses at the low temperature due to the quench process of our metallic glasses. We have found that is possible to almost entirely remove these stress fluctuations by first applying small prestress to the material to presumably relax the residual stresses and we describe this pre-stress procedure in Appendix C. Our observations strikingly resemble those of a crystal at low temperatures in that there is a fast, inertial motion in which the particles move ballistically, followed by caging after a timescale on the order of 0.1 ps in these materials [50]. At very long times, there is the hint that the particles are entering a regime in which they are no longer localized after the material has been sufficiently deformed, but this time regime is difficult to access by simulation at low strain values (We return to a consideration of this long-time regime below.). Importantly, $<r^2(t)>$ plateaus after the 'caging time' t_{cage}, a time that defines the Debye-Waller parameter, $<r^2((t_{cage})> \equiv <u^2>$. In the inset of Figure 5.3(a), we see that this quantity varies linearly with T in the glass state, as normally observed for $<u^2>$ in crystalline materials at T much lower than the melting temperature [45]. The mobility of the particles in the metallic glass, defined by the mean amplitude of atomic motion, clearly depends on T in a similar fashion in both crystalline and glass 'solids'. Corresponding to the plateau in $<r^2(t)>$, there is a plateau in the self-intermediate scattering function $F_s(q,t)$ having indefinite persistence in the time in the absence of deformation, signaling that the metallic glass is in a *non-ergodic state* (i.e., the density-density autocorrelation function does not decay to zero at long times). Appropriately, the magnitude of the plateau in $F_s(q,t)$ is often termed the 'non-ergodic parameter', which provides a quantitative measure of the 'degree of relaxation' that can occur in the glass state. As we shall discuss below, the α-relaxation time τ_α, which is characteristic relaxation time of cooled liquids can be taken to be *infinite*. Upon sufficient deformation, this relaxation process re-emerges so that $F_s(q,t)$ appears to decay as in a cooled liquid. We investigate this long time regime briefly below.

To quantify this transition in the dynamics, we examine how $<r^2(t)>$ is altered by a large deformation of the material. In Figure 5.3(b), we apply a range of strains up to $\varepsilon = 8.9$ % for material with $h = 300$ Å at $T = 50$ K, with each curve calculated within $\varepsilon \approx 2$ % strain interval. The dynamics is unaffected in the short time regime, which is completely controlled by the particle kinetic energy, but at long times we observe a transition to delocalized behaviour at a progressively shorter time with increasing strain. The trend is again very much like what we would expect to see in crystalline materials at low T and cooled liquids upon raising T, although it is not clear that the dynamics is diffusive beyond the caged regime in the strained material. We briefly discuss this longer time dynamics below.

While the plateau value of $<r^2(t)>$ does not change greatly with strain in Figure 5.3(b), a small variation in $<u^2>$ with ε can be seen upon enlarging the scale in the inset of Figure 5.3(b). The change of $<u^2>$ relative to its value at vanishing strain $<u^2(\varepsilon = 0)>$ and normalized by the square of the average particle distance, σ, $\delta<u^2> \equiv (<u^2> - <u^2(\varepsilon = 0)>) / \sigma^2$, increases nearly linearly with ε over the large range of strain considered in our simulations. The magnitude of $<u^2>$ then depends on both a thermodynamic contribution $<u^2(\varepsilon = 0)>$ and a contribution arising from the applied strain, $\delta<u^2>$.

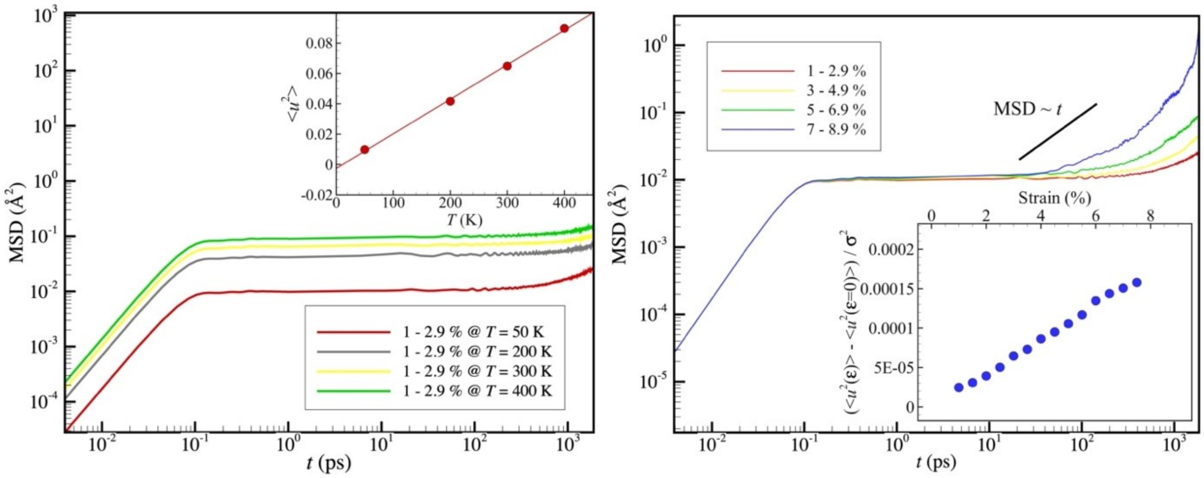

(a) (b)

Figure 5.3 Qunatification of atomic displacement in the glass state and particle caging. (a) Average mean square displacement $<r^2(t)>$ of all the atoms at different temperatures in the elastic regime. Inset shows that $<u^2>$ exhibits a linear relationship with T. (b) Average mean square displacement $<r^2(t)>$ of all the atoms at different strain levels. Inset shows the normalized $<u^2>$ as a function of applied strain.

In a previous study of shear in GF liquids [224], it was found that the structural relaxation time from the intermediate scattering function $F_s(q, t)$ approaches the caging time t_{cage} at high rates of deformation and it is natural to consider whether a similar trend applies when the metallic glass is deformed. One difficulty in pursuing this question is that the definition of 'relaxation time' is not obvious in the metallic glass state. In experimental studies of metallic glasses, the Johari-Goldstein relaxation process is widely recognized as being the primary relaxation process in the glass state, but the direct investigation of this relaxation process involves the simulation or measurement investigation of mechanical relaxation processes at very low temperatures. In recent simulation studies of an Al-Sm metallic glass [227,228], however, we have shown that the Johari-Goldstein relaxation process essentially coincides with a specific measure of dynamic heterogeneity, the average lifetime τ_M of mobile particle clusters. This is a quantity more readily investigated by simulation and, conveniently, does not require the computation of mechanical properties of the material such as the stress autocorrelation function. We have previously investigated the distribution of the 'mobile particle clusters' in Zr-Cu metallic glass-forming liquids in the liquid regime, [43,247] and we next consider whether τ_M exists in the glass state and whether this quantity can serve as a relaxation time in the glass state, as in the Al-Sm system.

We should note here that the emergence of particle clusters having excessively high and low mobility in relation to expectations of Brownian motion is a general feature of GF liquids and this aspect of GF liquids, along with methodologies for identifying such particles, their distribution of size, average size, fractal geometry, lifetime, etc. have been discussed at length in previous publications on both metallic glass and polymeric GF liquids. [247,55] The reader is referred to this previous works devoted to this topic for the requisite technical discussion of these 'mobile' and 'immobile' particle clusters, which together define the dynamically heterogeneous nature of GF liquids. We find the same clusters arise in the glass state.

In Figure 5.4, we examine the average mass of the mobile particle clusters as a function of time *t* using the same method of defining the mobile particles as described before [228] except that we consider a range of strain values between 3.0 % to 8.0 % in the glass state rather than a range of temperatures in liquid state. In the present analysis, we define 'mobile particles' as corresponding to the top 2.75 % the most mobile particles of the system at any point of time (see Appendix C for the details on how we uniquely determine this cut-off value following the suggestion of Starr et al. [55]) As in our previous simulations in the 'liquid' regime above T_g [247], the average mass of the mobile clusters generally exhibits a maximum at a characteristic time, τ_M, which defines the 'mobile cluster lifetime'. We further see that increasing strain significantly decreases τ_M, but the cluster size *increases*. In our previous study of τ_M in the liquid regime, we also found that τ_M was approximately equal the non-Gaussian parameter, a common measure of dynamic heterogeneity. The non-Gaussian parameter, $\alpha_2(t) = \frac{3<r^4(t)>}{5<r^2(t)>^2} - 1$, measures the deviation of the displacement dynamics from a Gaussian, i.e., $\alpha_2(t)$ is defined to equals zero if the displacement distribution is Gaussian. The particle displacement distribution is Gaussian in fluids where the fluid dynamics is highly chaotic and the theory of Brownian motion applies, but this distribution also arises in crystalline materials at low temperatures where the particles are perfectly localized in their potential wells. The distribution function also becomes Gaussian in the short time inertial dynamics regime as a consequence of the Maxwell-Boltzmann distribution of the particle velocities for materials in equilibrium and the near ballistic nature of the particle motion in this short time regime. The magnitude of this distribution can thus provide information about whether the system is in at least local equilibrium or whether particle motion is localized, or a diffusion process reasonably modeled by Brownian motion. Correspondingly, we show the variation of $\alpha_2(t)$ as a function of time in Figure 5.5(a) for a range of strains, and in the inset of this figure we see that τ_M exhibits a nearly linear relationship with t^* (the time at which the non-Gaussian parameter peaks) in the glass state. Recently, Puosi et al. also suggest a strong correlation between the peak time in the non-Gaussian parameter t^* and JG β-relaxation in a model polymer glass-forming liquid using molecular dynamics simulation [248] so that this relation seems to have some generality, even if it is not universal. This suggests that this measure of 'dynamic heterogeneity' is common to both cooled liquids and the glass states and derives from the existence of mobile particle clusters. We note that mobile particle clusters having a lifetime τ_M also arise in heated crystalline materials [50] so this definition should apply just as well for crystalline materials both under quiescent or deformation conditions.

We have previously shown that the dynamics of the mobile particle clusters and the JG relaxation process in an Al-Sm metallic glass involves an intermittent particle 'jump' process. By 'intermittent', we mean that the jumping events can be described by a universal distribution with a power-law tail. Relaxation processes exhibiting this type of temporal heterogeneity exhibit non-exponential relaxation and the application of a renewal theory to relaxation in material systems indicates that relaxation in systems with this type of intermittency should generally be described by the Mittag-Leffler family of functions, which in the frequency domain is known as the Cole-Cole relaxation function [200,249]. This type of relaxation is commonly observed for the JG β-relaxation process in glasses [250,251], including metallic glasses when the alpha and beta relaxation processes are well-separated [252]. Mittag-Leffler relaxation leads to power-law stress relaxation at long times rather than the exponential or stretched exponential function (or the Havriliak-Negami function in the frequency domain [200,249]), characteristic of the alpha relaxation in the liquid regime or to power-law creep deformation under applied constant stress [253].

We suggest that the Cole-Cole relaxation function is *universal* for the Johari-Goldstein β-relaxation process observed in mechanical and dielectric measurements in glass materials. Power-law creep is a nearly universal property of diverse solid materials, encompassing glass, polycrystalline and crystalline materials having many different types of chemical composition (polymeric, metallic and ionic materials) [254–263]. The 'creep exponent' describing the progressive power-law change in the material dimensions under constant applied stress is often observed to be near 1/3 (‘Andrade creep’), a value that Douglas and Hubbard have interpreted before as arising from polymeric chains of locally icosahedrally-packed particles in many glass-forming materials[200].

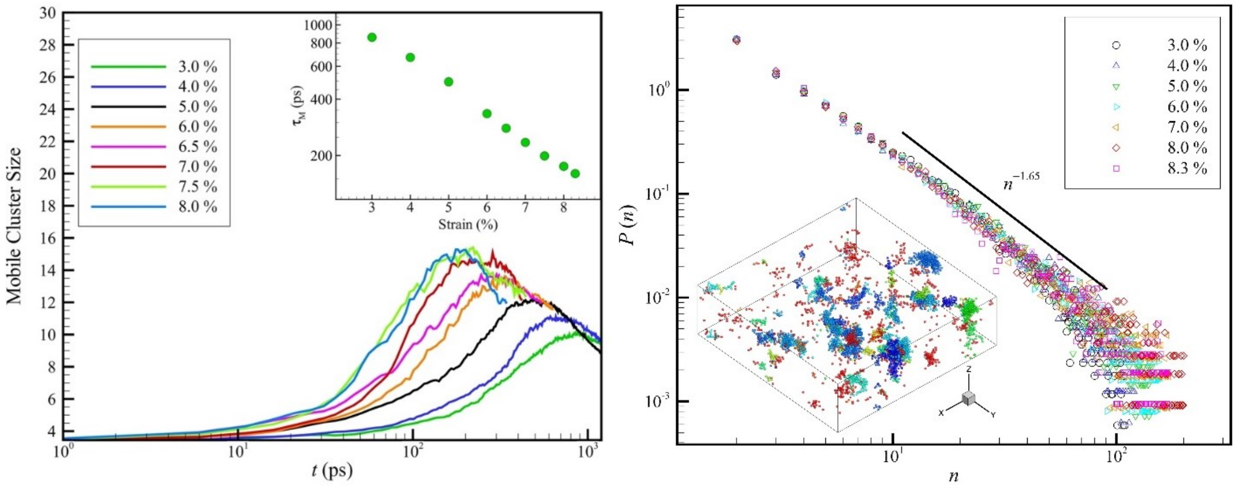

(a) (b)

Figure 5.4 Evolution of mass of mobile particle clusters in time, their lifetime with strain and their size distribution. (a) Mobile cluster size as a function of time at different strain levels for T = 50 K and h = 300 Å. (b) The mobile particle probability distribution function at different strains. The inset shows the mobile cluster configuration at 7.0 % with a size of 20 × 20 × 6 nm.

The evolution of the average size of the mobile particles and their size distribution is evidently similar to previous observations in the liquid regime, but strain clearly alters their size and average ‘lifetime’, determined by the time at which their average mass peaks. The size distribution of the mobile particles is nearly the same in the interior and interfacial regions, and the fractal geometry of the clusters in these two regions are almost identical, so there is apparently no essential difference in the geometry of the clusters in these regions. We have included a comparison of these distributions in Appendix B, along with a quantification of the dynamic clusters, which are a good candidate for 'shear transformation zones'.

Although the α-relaxation process is inaccessible in simulations of both crystalline and glass materials at low temperatures because of its extremely long timescale or complete lack of existence, we may consider whether τ_M may serve as a 'relaxation time' appropriate for the glass state. We show in Figure 5.5(b) that the strain dependence of τ_M can be brought into an apparent universal reduced form in which τ_M approaches t_{cage} corresponding to the limit of a nearly 'perfect fluid' as the strain is increased. In particular, τ_M is well-described by the scaling relation,

$$(\tau_M - t_{cage})/t_{cage} \sim A[(\varepsilon_c - \varepsilon)/\varepsilon_c]^{\delta} \qquad 5.2$$

A = 7.0, δ = 1.37, where the 'critical' strain, ε_c = 8.3% at which this limit is achieved corresponding to the point of shear band formation. This scaling mirrors the approach of τ_α to t_{cage} in the liquid regime for liquids subjected to increasing deformation [224].

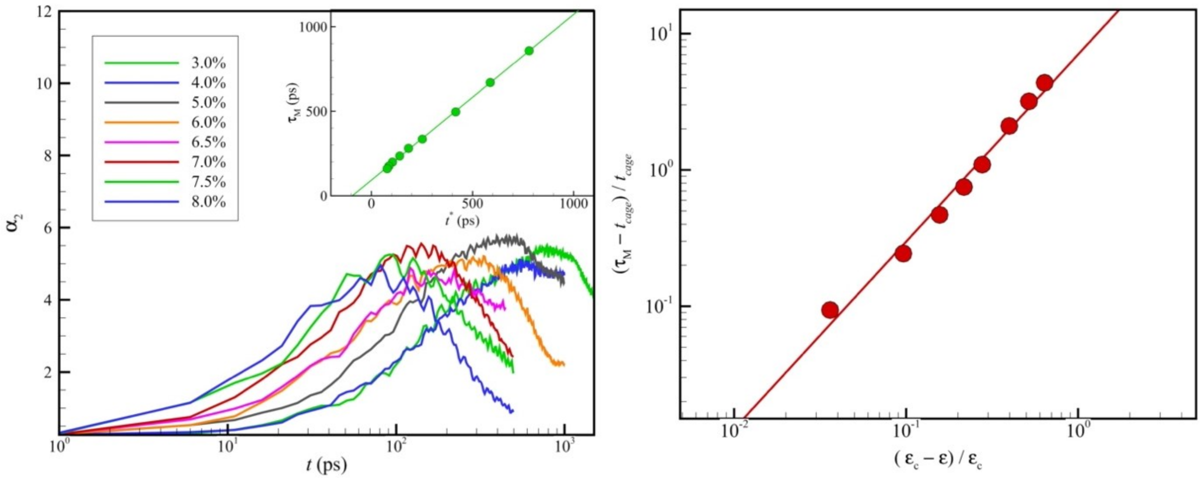

(a) (b)

Figure 5.5 Quantification of non-Gaussian parameter and its relation between its peak value and τ_M. (a) Non-Gaussian parameter as a function of time at different strain levels. The inset shows the time t^* at peak in non-Gaussian parameter exhibits a linear relationship with mobile particle lifetime τ_M at different strain levels. (b) Scaling relation between mobile particle lifetime τ_M and strain.

Recently, Giuntoli et al. [224] have emphasized that the approach of the relaxation time τ_α of the fluid to t_{cage} corresponds to the point at which the α-relaxation time merges with the fast β-relaxation time and that this condition corresponds to a flow instability condition because this condition implies that relaxation of the fluid by momentum diffusion (More precisely, the kinematic viscosity ν, the ratio of the shear viscosity to the fluid density, is the momentum diffusion coefficient in hydrodynamic theory, but under the normal condensed fluid conditions in which the fluid density is nearly constant we may think of the shear viscosity as being proportional to the momentum diffusion coefficient.) becomes essentially suppressed at this point, i.e., the fluid can be viewed as roughly equivalent to an inviscid fluid from a modeling standpoint. 'Turbulent' or 'chaotic' flow is common observed in fluid flow having such exceptionally low viscosities [264], and, although there is no generally accepted theory of the transition to turbulent fluid flow, this tendency can be qualitatively understood from recent computational investigations of particle motion in idealized inviscid fluids, where it has been observed that the motion of a solid body through an incompressible, inviscid fluid, moving irrotationally, and otherwise at rest, is inherently chaotic [265]. It is notable that such turbulent motion has been observed in flowing polymeric liquids even under conditions in which the inertial energy of the fluid flow, as quantified by the Reynolds number, is small [266–268].

Simulations have recently shown that shear band formation after sufficiently large deformation of our metallic glass leads to the onset of hierarchical vortex formation, transient super diffusive motion, and other features common turbulent fluids (see discussion below.) This phenomenon in glass materials appears to be another variety of ‘elastic turbulence’. Taylor [269] long ago stressed the analogy between turbulent flow in liquids and the heterogeneous flow expected to arise in association with the deformation of polycrystalline materials. Our results below support this intuition.

In order to quantify the emergent dynamic heterogeneity in our strained MG material, we next consider an apparently general relation between $<u^2>$ and the glassy shear modulus G of the material obtained for the stress-strain relation in the limit of linear deformation. This relation will enable us to relate the shear modulus of the material over the entire accessible temperature range (200 K $< T <$ 1000 K) to $<u^2>$ of the material as a whole, and this also allows us to make a map of the local stiffness as a function of strain that will enable us to gain significant insight into the pre-transitional softening of the MG material leading up to the formation of SBs.

Our neglect of any consideration of α-relaxation in our simulations at T well below the glass transition temperature, estimated to be T_g = 817 K for the present metallic glass [43], deserves some explanation. In previous work on the same MG based on the same potential as in the present paper, we found that we could predict the α-relaxation time τ_α without free parameters from simulation estimates of $<u^2>$ in the liquid state regime above T_g. In particular, the structural relaxation in the viscous liquid regime is predicted by the localization model to equal,

$$\tau_\alpha(T) = \tau_\alpha(T_A) exp\left[(\langle u^2(T_A)\rangle \,/\, \langle u^2(T)\rangle)^{3/2} - 1\right] \tag{5.3}$$

where T_A is an onset temperature for non-Arrhenius dynamics in the structural relaxation time and the rate of atomic diffusion. We also found in this former work that $<u^2>$ varied nearly linearly with T at low temperatures below the crossover temperature T_c = 1055 K, separating high and low temperature regimes of the glass-forming liquid [43,207].

The temperature variation of $<u^2>$ also serves to define two well-defined temperature regimes governing the glass state. In particular, $<u^2>$ estimates in the liquid regime formally extrapolate to 0 at a finite temperature T_o = 711 K, the *same* temperature at which the structural relaxation time τ_α diverges in corresponding fits of the Vogel-Fulcher-Tammann [270] estimates of τ_α [43] (We emphasize that this extrapolation does not mean that the relaxation time actually diverges at T_o). The T regime well below the glass transition, defines the 'low temperature glass state', the T regime that is the focus of the present paper. Our estimates above of $<u^2>$ in the low T glass state indicate that this quantity is positive, but τ_α can nonetheless be reasonably taken as being 'infinite' for all practical purposes. Specifically, the localization model [43] for τ_α that quantitatively describes in the T range above T_g indicates that the value $<u^2>$ = 0.0098 Å^2 found at T = 50 K for our metallic glass implies a value of τ_α ~ (10^{1153} years), which is quite large even in comparison with the estimated lifetime of the universe τ_{univ} indicated by the Lambda-CDM Concordance model [271], i.e., the time elapsed since the Big Bang, τ_{univ} ~ O(1.4 x 10^9 years). It seems safe to conclude that 'viscous relaxation' and τ_α are not relevant to describing relaxation in low temperature glasses, and, by default, we define the relaxation time in terms of the Johari-Goldstein relaxation process, which we have found can be estimated from the lifetime of the mobile particles τ_M and t^*, as we discuss above.

In our previous paper, we found that diffusion still exists in the glass state, albeit its magnitude is relatively small, and that the diffusion coefficient D scales as, $D / T \sim 1/ \tau_M$ [227,228] so that the rate of diffusion in the glass state is directly linked to τ_M. Unfortunately, the determination of D in the glass regime in the low regime that we study requires prohibitively long simulations. The rapid growth of τ_α to astronomical time at low T means that the plateau in Figure 5.3 persists to essentially 'infinite' time in the low temperature glass state and there is evidence from both experiment [272] and simulation [273–275] that a true finite equilibrium (zero frequency) shear modulus can emerge in the glass state. Note that this analysis suggests that there is a separate high temperature glass regime for $T_o < T < T_g$ in which the Zr-Cu alloy exhibits a solid-like response over an appreciable timescale, but the material still exhibits a finite τ_α so that the material exhibits viscoelastic response that is similar to a fluid over long timescales. This is the viscous 'plastic deformation' domain [276]. We have also argued that the relationship between the relaxation time τ_α and $<u^2>$ derives from the weakly chaotic nature of GF and complex fluids in which this relation holds. Correspondingly, we may anticipate by this same reasoning that this relation to *breakdown completely* at low T as the material undergoes an ergodic to non-ergodic transition upon cooling into the low temperature glass state. [277,278]

The decay of the intermediate scattering function to a plateau at long times as in a crystal at finite temperature, also implies that the material should exhibit a corresponding plateau in the shear stress relaxation function G_p corresponding to a finite zero frequency shear modulus. The emergence of a finite 'equilibrium shear modulus' G in the glass state has been discussed in numerous recent simulations, theoretical and experimental studies of glass-forming materials. [272–274,279–283] The localization of particles by surrounding particles is also signaled by a drop in the communal entropy of the fluid, a phenomenon observed in both materials that solidify into crystalline and non-crystalline solids. [284] This type of transition has been discussed as a characteristic feature of jamming transitions [285] and the same arguments seem to apply to the onset of the glass state. Apart from the breakdown of Eq. (5.3) relating τ_α to $<u^2>$, and the lack of even the existence of a measurable τ_α, [286,287] this transition also implies the breakdown of ordinary thermodynamics. While the material still explores its phase space in a limited way in the 'glass' regime, we may expect the emergence of a generalized non-extensive thermodynamics under these circumstances, as illustrated by model computations dynamical systems at the edge of chaotic behavior [288,289]. In particular, we may expect new limit theorems associated with non-extensive thermodynamics to emerge under these conditions [290], corresponding to a distribution function for particle displacements that greatly differs from the Gaussian functional form, which arises in the liquid regime along with a mean square displacement increasing linearly in time, as consequence of the limit theorem associated with the strongly chaotic nature of the fluid dynamics at elevated temperatures. We indeed see evidence of transient super-diffusion and a highly non-Gaussian distribution function for atomic displacement probability emerge that is consistent with Tsallis statistics [290], features that are observed in a wide variety of 'turbulent' systems. This type of highly non-Gaussian displacement distribution has been observed before phenomenologically in simulations of creep in a Zr-Cu metallic glass material in its glass state [291].

5.3.3 $<u^2>$ as a Measure of Bulk and Local Material Stiffness

To address the question of local elasticity evolution with time, position and strain, an appropriate and computationally feasible measure of local material 'stiffness' is required. In addition to being a measure of 'mobility', we argue below that $<u^2>$ can also be interpreted physically as a measure of material stiffness. The Debye-Waller parameter $<u^2>$ has the dual advantage of being defined at an atomic scale and of being readily measurable by X-ray, inelastic neutron scattering, and other scattering techniques [292–294], although spatially resolved measurements at a nanoscale are not currently possible. Simulation studies on both polymeric GF liquids [128] and metallic GF liquids [43], have established a linear scaling relationship between shear modulus G and $k_B T / \langle u^2 \rangle$, where $k_B T$ is the thermal energy and we consider the validity of this relation in the present material, first in the bulk material and then as providing a measure of local material stiffness.

To test this scaling relation linking G and $\langle u^2 \rangle$ in the glass state in which our shear banding simulations are performed, we first determined G by applying constant shear rate along one direction on $Cu_{64}Zr_{36}$ alloy bulk samples at different T ranging from 200 K to 1000 K, and calculated stress-strain curves at different T in Figure 5.6 (a) to obtain the estimates of G as a function of T shown in Figure 5.6 (b). The inset to Figure 5.6 (b) shows the linear correlation between G and $k_B T / \langle u^2 \rangle$ in $Cu_{64}Zr_{36}$ previously observed by Douglas et al. [43] at room temperature. This type of relation, although the specific functional form is somewhat different, has been discussed for many systems previously by Leporini and coworkers [235,236]. The relationship motivates defining $k_B T / \langle u^2 \rangle$ as a measure of *local* 'stiffness' that we will then consider in connection with the onset of shear band formation.

Before making a local 'map' of material stiffness based on $\langle u^2 \rangle$, we discuss the motivation for applying this scaling relation between G and $\langle u^2 \rangle$ locally within the material and the limitations of this 'correspondence'. First, we note that the shear modulus G is defined in the thermodynamic limit and that there is no obvious unique local counterpart of this material property. This situation provides us with some latitude with defining a local measure of material 'stiffness' that is consistent with the definition of G in the thermodynamic limit. Under the circumstances, we think that it is best not to identify this local measure of 'stiffness' as being *exactly* the local shear modulus, however. Accordingly, we define the local stiffness $\boldsymbol{S}$ by the relation,

$$\mathbf{S} \approx \mathbf{S}_0 + \mathbf{S}_1 \, (k_B \, T) / \langle u^2 \rangle \, l \tag{5.4}$$

where $\boldsymbol{S}_o$ and $\boldsymbol{S}_1$ are fitted constants defined by the *macroscopic* scaling relation, and $\boldsymbol{S}$ exactly reduces to the glassy modulus G. Leporini and coworkers [235,236] have discussed this phenomenological equation at length and have tried to interpret G_0, and the mysterious length scale l arises in Eq (5.4) by dimensional consistency. A full understanding of $\boldsymbol{S}_o$ and $\boldsymbol{S}_1$ and l remain an outstanding question that we do not concern ourselves here where we are interested only in obtaining a qualitative stiffness measure.

Notably, this same relation between 'stiffness' and $k_B \, T / <u^2>$ has often been reported to apply at an *atomic scale* in the interpretation of neutron and x-ray scattering measurements [295–303]. The motivation for taking $<u^2>$ as a measure of local molecular rigidity derives from the harmonic oscillator model, a molecular model of 'elasticity' in which the harmonic oscillator force constant k_h equals $k_B \, T \, / \, <u^2>$ (see Appendix B of Ref. [[304]]). At an intermediate scale between atoms and bulk materials, this type of scaling relationship has also been tested affirmatively in molecular dynamics simulations of the shear rigidity of semi-flexible polymers where the effective polymer rigidity inferred from the persistence length, along with well-known estimates of the dependence of the persistence length of worm-like chains as a function of shear rigidity, again conforming with Eq. (5.4) (See Appendix B of [[304]]). We collectively infer from these numerous observations that we might quite reasonably interpret $k_B \, T \, / \, <u^2>$ as a local measure of material 'stiffness', although the literal identification of this quantity with a local shear modulus is questionable. To further establish the physical basis of this local 'stiffness metric', we consider an alternative measure of local stiffness and compare to the $<u^2>$ derived measure.

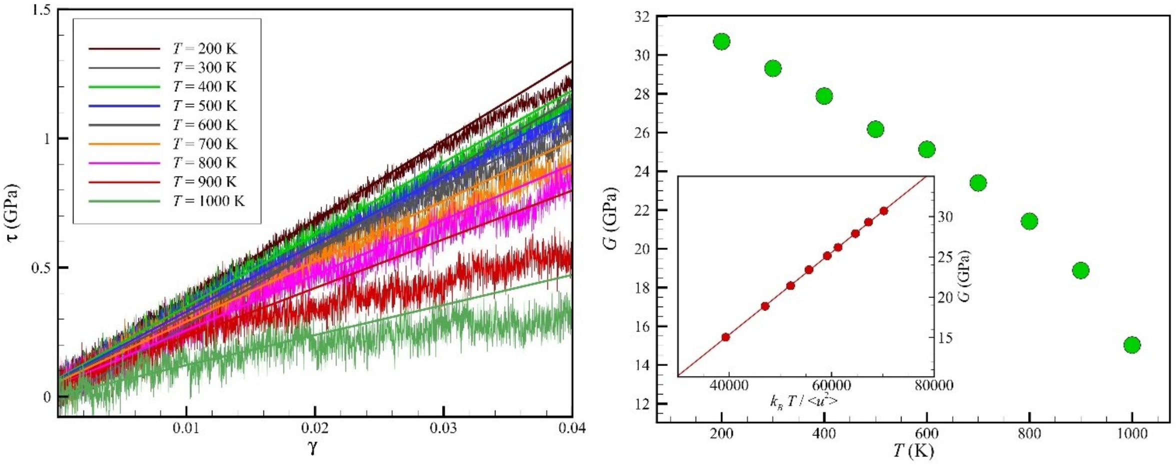

(a) (b)

Figure 5.6 Estimation of shear modulus as a function of temperature from deformation in the near elastic regime. (a) Stress-strain curve for $Cu_{64}Zr_{36}$ over a range of T under shear deformation. (b) Shear modulus G versus T for the bulk material. Inset shows a linear relationship between G and $k_B T / <u^2>$ for the bulk $Cu_{64}Zr_{36}$ metallic glass material.

As an alternative to taking k_B T / $<u^2>$ as a measure of local stiffness, we may independently estimate local material stiffness based on a consideration of *local* stresses and strains in the material at the atomic scale. In particular, we may define the 'local elastic constant' by a formal extension of its macroscopic definition as, $C_{11,i} = \Delta\sigma_i/\varepsilon_i$, where $\Delta\sigma_i$ has been taken as the von Mises stress on each particle i, and ε_i is the von Mises strain of each particle [303,305]. Figure 5.7 shows the contour maps of the local elastic constant and local stiffness measure k_B T / $<u^2>$ for a $\varepsilon = 2.0$ % strain. In general, the correspondence between the colormaps describing the magnitudes of C_{11} and k_B T / $<u^2>$ is reasonable, but not perfectly isomorphic. The average scale and variance of the fluctuations in these stiffness measures seem to hold very well, however. We take this as further evidence that it is reasonable to consider both $k_B T / \langle u^2 \rangle$ and C_{11} as local stiffness measures, although we again emphasize that we must refrain from exactly identifying either C_{11} or $k_B T / \langle u^2 \rangle$ with a local shear modulus.

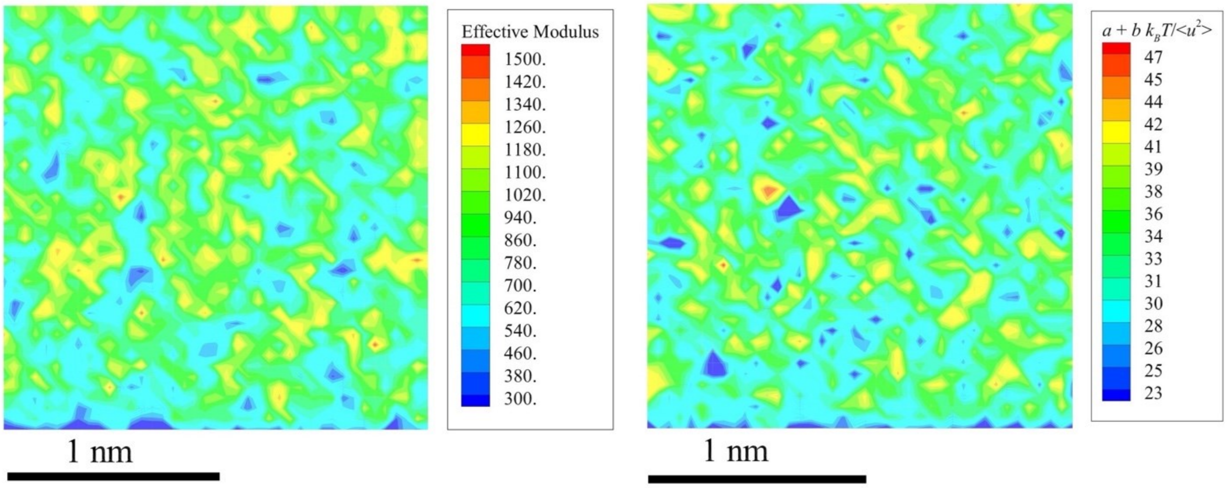

Figure 5.7 Contour maps of the local elastic constants (C_{11}) and local shear modulus ($k_B T / \langle u^2 \rangle$) at $\varepsilon = 2.0$ % of a 200 Å x 200 Å x 5 Å slab.

5.3.4 Local 'Softness' Evolution During Shear Band Formation

As emphasized in the Introduction, It has long been suggested that the initiation of shear band formation should initiate in soft spots in the material in which large non-affine deformations are concentrated [306–309] and it is for this evident reason that we have defined a precise local measure of material stiffness to test this hypothesis.

If this interpretation of the mechanism underlying SB formation holds, then we may expect that the stiffness of the region forming the SB to be rather distinct from regions that remain in an ordinary glass state that is more similar to the undeformed bulk material than the SB region. The material also has an interfacial region in which the dynamics of the SB and bulk regions of the MG material are distinct from the material interior (See Figure 5.8(a)) [232]. The SB interfacial regions are defined by the atoms located in the upper and lower surfaces area with a thickness of 15 Å and these regions are marked in Figure 5.8(a). The following analysis is based on the sample with h = 300 Å.

We then analyze how the stiffness $\boldsymbol{S}$ in the defined regions of Figure 5.8 (a) evolves as the material is deformed. In particular, we define ζ as the ratio of the number of atoms having a value of $k_B\, T\, /\, \langle u^2 \rangle$ less than the critical value to the total number of atoms in the designated region. In our analysis, the critical value of $k_B\, T\, /\, \langle u^2 \rangle$ is taken to be specifically 33 KJ/m^2, which corresponds to this stiffness measure at the crossover temperature T_c at which previous molecular dynamics studies have established the onset of highly anharmonic 'liquid-like' motions in the interfacial regions of both crystalline and metallic glass materials [232]. The crossover temperature T_c separates the high and low T regimes of the glass-formation [43].

The black line in Figure 5.8(b) corresponds to the stress-strain curves for ε between 7 % to 11 % and the sharp change in ζ indicates there is a critical strain region at which shear banding initiates. Apparently, the fractions of atoms in SB and bulk regions are almost identically near, but below the stress maximum defining the 'yield' of the material (see Figure 5.1), i.e., a strain of 7.6 % at this T. Beyond this point, the soft regions in the SB apparently mediate the plastic deformation localized to the SB. A similar behaviour, but greatly amplified, is observed in the interfacial regions where the fluctuations in ζ are especially large. We next consider how the distribution of local stiffness, defined in terms of $\langle u^2 \rangle$, varies with deformation both deep within the MG material and in the interfacial region, where we find that the onset of SB formation corresponds to a 'critical' condition in which the stiffness within the material becomes equal to its value in the interfacial region in the absence of deformation. This instability condition was completely unanticipated.

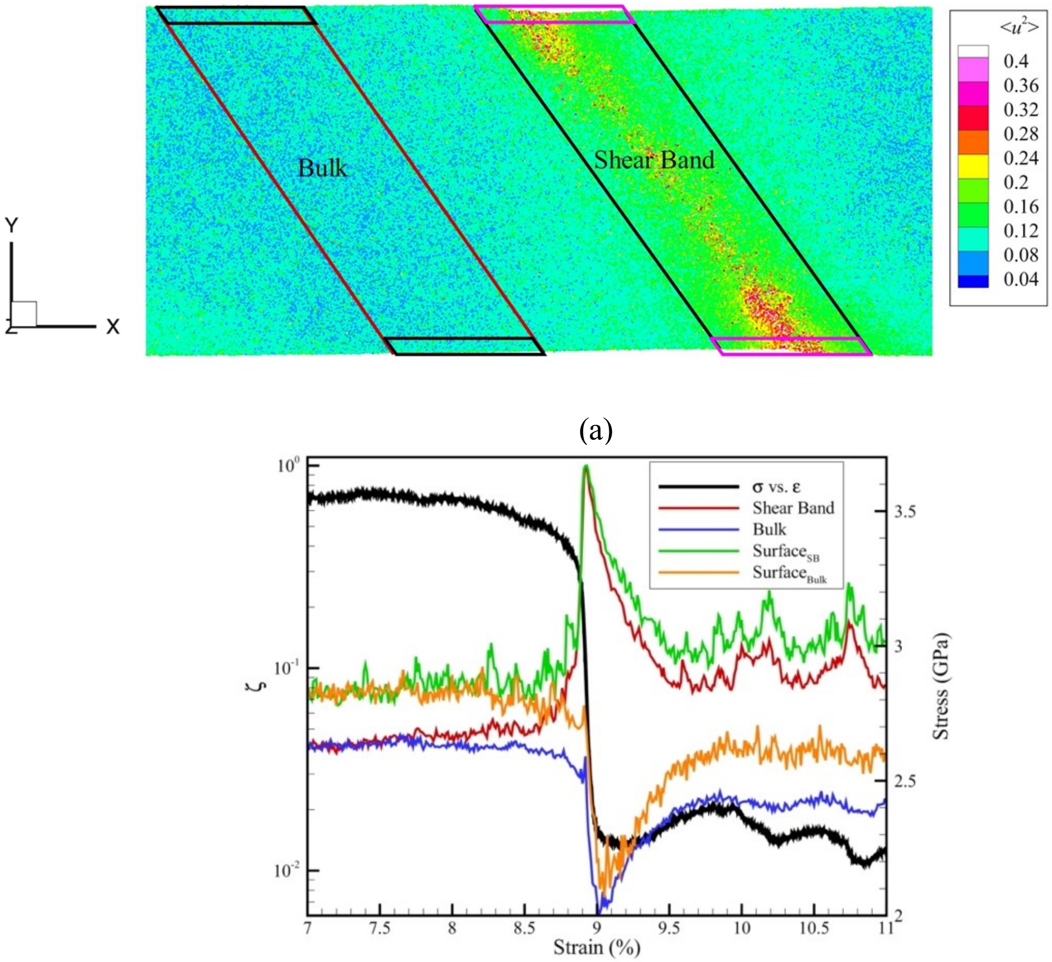

(a)

(b)

Figure 5.8 Shear band and bulk regions are defined in terms of local 'stiffness' and the evolution of stiffness under strain. (a) Distribution of $<u^2>$ in the sample, showing the shear band and bulk regions, as defined in the text. Interfacial SB and bulk regions having a thickness of approximately of 15 Å are indicated for both regions [310]. (b) The evolution of the fraction of softness in the strain range of 7.0 % to 11 %. Four areas were tested, SB region, bulk region, surfaces of SB region, and surfaces of the bulk region. The corresponding stress-strain curves are presented as the black line.

5.3.5 Shear Band Formation as Emerging Interface within the Metallic Glass Material

The full development of a SB has one of its implications as emergence of an interface within the material, and we may therefore expect that the dynamics within the incipient SB region to progressively become similar to the dynamics of interfacial region of the material. We have recently quantified the interfacial dynamics of both metallic glass and crystalline materials based on modelling that emphasizes the gradient in $<u^2>$ in the interfacial region of these materials [232] so that the current analysis is a natural extension of this previous work. We first show that this approach of the elastic fluctuations in the interior of the incipient SB indeed approach that of the interfacial region and we follow this analysis by introducing a measure of the degree to which the atoms in incipient SB have been converted into a dynamical state consistent with the interfacial dynamics of the material.

Figure 5.9(a) shows the local stiffness $\boldsymbol{S}$ distribution of the entire sample (h = 300 Å) at different strains before the maximum stress, with distribution on surface and interior as reference. The overall probability distribution of $\boldsymbol{S}$ for the interior of the material evidently progressively approaches the distribution of $\boldsymbol{S}$ of the interfacial region in the absence of strain as ε increases from zero to the critical strain for SB formation. Similar behaviour has been observed in systems with h = 90 Å, 150 Å.

We note that the average magnitude of $<u^2>$ within the region that ultimately forms a shear band changes from $<u^2> = 0.0098$ Å^2 to a value $<u^2> =0.0109$ Å^2 at the onset of shear band formation. This change in $<u^2>$ allows us to estimate the change in the relative stiffness of SB region compared to the undeformed material, $\delta G \equiv [G(\mathrm{SB}) - G(\varepsilon = 0)] / G(\varepsilon = 0)$. For the h = 300 Å film at T = 50 K, we find $\delta G = -0.12$. The shear band regions are inherently softer than the undeformed material. A softening in the SB region has been reported experimentally in indentation studies of metallic glass materials [311].

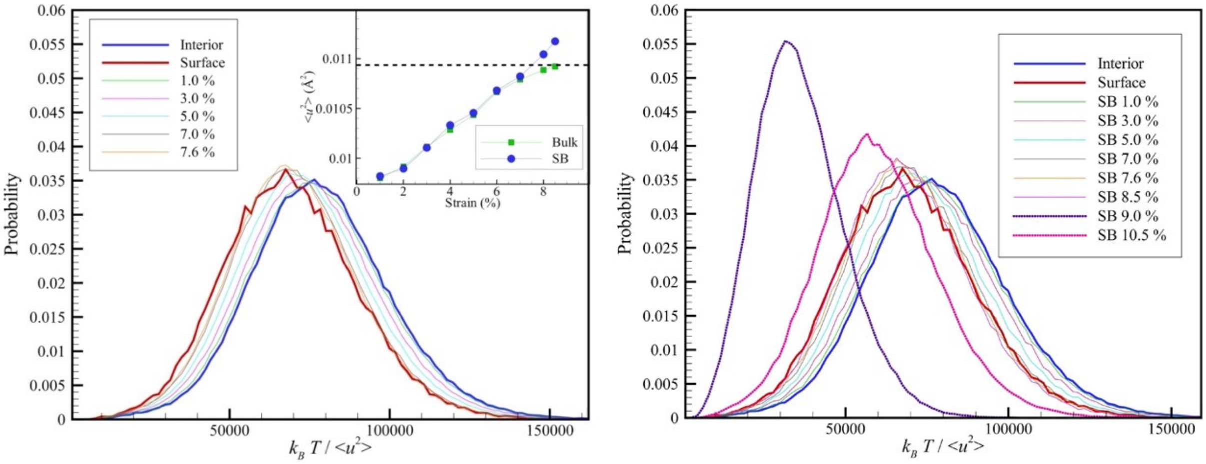

(a) (b)

Figure 5.9 Distribution of the effective stiffness distribution in the interfacial regime and with the metallic glass material in the deformed and undeformed states for h = 300 Å film at T = 50 K. (a) Comparison of shear modulus distribution of entire sample at different strain rates before reaching maximum stress. Blue and red lines are the reference distribution at center and surface at zero strain. The dashed line in the inset is the $\langle u^2 \rangle$ of the interfacial region at the undeformed state. Apparently, the $\langle u^2 \rangle$ of the bulk and shear band approaches the value of $\langle u^2 \rangle$ at the interfacial in the absence of deformation, this convergence effect is illustrated in the inset figure. (b) Comparison of the estimated stiffness distribution within shear band at different degrees of strain with the stiffness distribution in the interfacial region ('surface') and the interior of the MG material ('interior') in the absence of strain.

We next examine the distribution of ***S*** in the SB region in Figure 5.9. As the strain approaches the 'yield' value of ε = 7.6 %, at which a maximum in stress or 'yield' (see Figure 5.1) occurs, the SB starts to form and the local stiffness (***S***) distribution essentially *coincides* with the interfacial ***S*** distribution near the point of yield. The significance of the relative value of $<u^2>$ in the interior of the material to that on the boundary under undeformed conditions is even more apparent in the inset of Figure 5.9 (a), where the magnitude of $<u^2>$ in the SB and the rest of the interior of MG material ('bulk') are nearly equal all the way up to the point of SB formation and yield. There is a clear suggestion from these observations that SB formation in our material reflects an instability in which the interior of the material has softened under deformation to such a degree that the stiffness is similar to the stiffness of the material prior to deformation. It apparently becomes energetically favorable for SBs to form when it becomes energetically favorable for the formation of interfaces within the material through local deformations arising within the material. As a practical implication, we note that the interfacial properties of metallic glass and other glass materials can be expected to greatly depend on how the material was fabricated so that the actual value of the critical deformation required for SB formation can then be expected to depend on exactly how the material was fabricated, especially with regard to fabrication processes what influence the interfacial properties of the material. This sensitivity of SB formation and yield to the surface 'states' has been demonstrated in recent studies of metallic glasses [312–314], consistent with our general finding that $<u^2>$ in the boundary of the MG material plays a crucial role in determining the onset condition for SB formation. Ivancic and Riggleman [315] have recently observed in a strong sensitivity of shear banding to defects in the interfacial region in simulations of a coarse-grained polymer material in conjunction with machine learning methods to analyze their data.

We point out that recent measurements on glass-forming liquids have indicated the dynamics of the interfacial region is largely 'decoupled' from the interior of the material [316] so that we expect the interfacial value of $<u^2>$ defining the onset of SB instability to be rather insensitive to film thickness. This expectation remains to be checked by simulation and measurement.

This instability condition reminds us of another interfacial instability condition seen in connection with the interfacial dynamics and the dynamics within both crystalline and glass-forming materials. Even in the absence of material deformation, the average value of $<u^2>$ in the interfacial region and interior of both crystalline and glass-forming materials extrapolate to a common value, defining the 'Tammann temperature' at which the interfacial region starts to acquire a greatly enhanced mobility, and interestingly, this temperature appears to correlate strongly with the glass transition of the material [233]. Notably, this convergence of $<u^2>$ values within the material occurs near T_g and T_m in glass-forming materials (See Figure 2b of Mahmud et al. [232]) and the relevance of this phenomenon to the low temperature non-ergodic glass state is an open question.

Since we think that this condition is a related phenomenon to the SB instability that we observe, we found $<u^2>$ in the interfacial region and the interior of the material are seen to converge around 24 K. This is similar to our previous observations in the same metallic glass-forming liquids above T_g, where $<u^2>$ in the interfacial region and the interior of the material converge at a temperature close to glass transition temperature [232]. This 'premelting' or 'softening' would appear to be another interfacial instability associated with the lowered energetic cost of creating interfaces within the material and this instability appears to be of a very general nature.

The occurrence of the Tammann temperature in both crystalline and glass materials also makes us wonder whether a corresponding interfacial instability might arise in connection with the plastic deformation of crystalline materials. This is not the topic of the present paper, but we briefly note that both shear banding [317] and yield [318] are likewise observed in crystalline materials and the importance of interfacial mobility in the plastic deformation of small scale crystalline materials has also been emphasized [319–323]. In particular, the Zhu et al. [324] have noticed empirically that the barrier height for dislocation nucleation vanishes at a 'surface disordering temperature' (This temperature is typically about (1/2 to 2/3) T_g and thus quite distinct from T_g.), and characteristic temperature is consistent with our definition of the Tammann temperature. It has also been noted [325] that the brittle-ductile transition for dislocation free crystals follows the empirical rule (2/3) T_m., which further supports the potential relevance of the Tammann temperature for the plasticity of crystalline materials.

The obvious implication of these observations is that it should be possible to engineer the surfaces of both crystalline and glass materials to impact their plastic deformation. This possibility was suggested for crystalline materials by Zhu et al. [324] and recently realized in practice by Shin et al.[326] by modifying the surfaces with coating the material using atomic layer deposition. Recently there has been great interest in the strengthening of glass materials by modifying their interfaces, so-called "chemical strengthening" [327] and there would appear to be great scope for interfacial engineering the properties of materials based on the material processing changes that impact interfacial mobility.

One of the interesting implications of the occurrence of a Tammann temperature in crystalline and amorphous solid materials is its effect on material yield (see Figure 5.1). As T approaches this characteristic temperature at which $<u^2>$ in the interfacial region approaches $<u^2>$ deep within the material interior we may expect the material to become inherently unstable to plastic deformation ('flow' in the colloquial sense) without any appearance of 'yield'. Consistent with this argument, many experimental studies on both metallic and polymeric glass-forming liquids have indicated a general tendency for the yield stress to approach 0 as the T approaches the glass transition temperature of the material, a temperature that coincides closely with the Tammann temperature [276,328–330]. The same trend is observed in semi-crystalline polymers where the onset temperature is well below the melting temperature at which significant mobility emerges in these complex polycrystalline materials [276]. We remind the reader that this reasoning does not necessarily extend to the phenomenon of shear banding region since α-relaxation remains prevalent for an appreciable temperature range below T_g. It is not clear that shear banding accompanies yield in this *high temperature glass regime*, i.e., $T_o \leq T \leq T_g$ where we interpret T_o to be an ideal glass transition temperature at which the loss of ergodicity occurs. We may estimate T_o as the temperature by extrapolating $<u^2>$ of the material to 0 at low temperatures and in the present MG material this characteristic temperature was estimated[43] to equal, $T_o = 711$ K.

The formation of SB is not the end of the story. Upon increasing the strain further there is another distinct region beyond material 'yield' in which the SB regions undergo various transformations and in which the dynamics within the SB region changes greatly from the undeformed material. Viewed from a stiffness map perspective, regions rich in 'soft' particles at $\varepsilon = 9.0$ % to regions rich in 'stiff' particles for $\varepsilon = 10.5$ % so that a kind of strain hardening apparently occurs in the SB region under post-yield conditions. The probability distribution of $\boldsymbol{S}$ also appears to move towards larger $\boldsymbol{S}$ values when ε is progressively increased from $\varepsilon = 9.0$ % to $\varepsilon = 10.5$ %. After shear band formation initiates near $\varepsilon = 7.6$ %, there are non-trivial 'jerky' fluctuations in the stress-strain curve that arise from stress-induced particle movements that mediate large scale plastic deformation of the material. The local stiffness in the SB fluctuates greatly until the SB spreads throughout the sample. Below, we analyze this regime, where we find that the dynamics exhibits features similar to fluids undergoing a transition to turbulent flow, evidently corresponding to a kind of 'elastic turbulence'. The dynamics of this regime becomes much richer in this regime than before SB formation. Before briefly discussing this regime, however, we provide some further quantification of SB formation from a local stiffness perspective.

5.3.6 Brief Discussion of the Dynamics in the Shear Band Region Beyond the Yield Condition

As might be expected from the discussion above, the dynamics of the MG material becomes much more complicated beyond the point of yield and associated SB formation. An examination of the particle motions in this regime indicates the occurrence of complex vortex motions that are reminiscent of turbulent fluids [331–334]. A contour map of local shear modulus $k_BT/\langle u^2\rangle$ near shear band and displacement vector in the corresponding region exhibiting 'turbulent' were shown in Appendix C. This vortex state is a highly complex phenomenon with important ramifications for the dynamics of strongly deformed amorphous solid materials and we briefly address some of the conspicuous features of this dynamical state based again on a dynamic heterogeneity perspective.

One interesting phenomenon occurring in turbulent media, such as the earth's atmosphere, is that the average particle displacement from an initial position has often been observed to occur in a super-ballistic fashion over appreciable space and time scales [335–337]. In particular, the mean square displacement has often been observed to increase as t^3 compared to t^2 of ballistic motion and t for Brownian motion [337]. While there is still no rigorous hydrodynamic theory explaining this phenomenon, it is generally appreciated that this super-ballistic transport derives from highly correlated velocity fluctuations in the atmosphere that drive the particle motion. Above we noted the existence of vortex-like fluctuations in the shear band regions that are highly developed in the SB region beyond yield, and we correspondingly examined the t dependence of the mean square atomic displacement $<r^2>$ for atoms in the 'turbulent' SB region.

We find that $<r^2>$ increases very sharply with t in this unstable regime with an apparent power that is very large, as illustrated in Figure 5.10. It is probably best to think of this stress-driven transport as reflecting the macroscopic deformation within the SB associated with incipient 'fracture' (See Figure 1 b of Shrivastav et al. [238] where it is shown that there is a crossover back to diffusion at still longer times in their simulations of SB formation.) This type of crossover also arises at long times in passively driven particle displacement in turbulent fluids [337]. These brief observations offer only a small hint of the complexity of the dynamics within fully developed SBs.

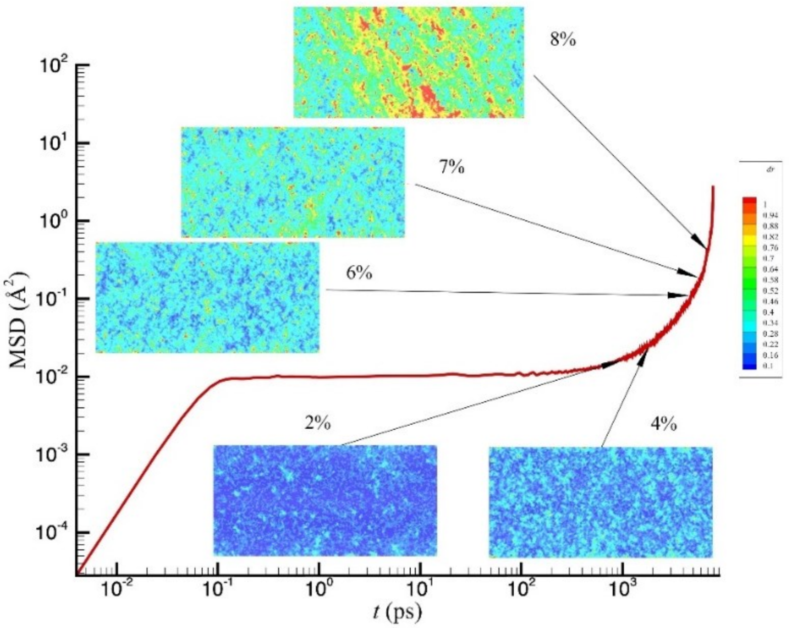

Figure 5.10 Atomic displacement and the evolution of stiffness heterogeneity. Mean squared displacement (compared with the initial state at ε = 1%) in the sample with h = 300 Å at T = 50 K. Displacement distributions at ε = (2, 4, 6, 7 and 8) % are shown in the graph. At 2 %, the sample shows non-localized displacement, but beyond about ε = 6 %, areas with higher displacement marked with red color start to appear and areas apparently trigger relaxation in the surrounding environment.

We note that superficially similar vortex excitations, ‘turbulence’ and transient super-diffusion ‘driven’ by the vortices occur in a wide range of systems beyond ordinary turbulence and the elastic turbulence of flowing polymer melts and deformed metallic glass materials. This type of phenomenon is observed in flowing granular media [338–342], dusty plasmas [343,344], the movement of cells in living tissues [345–347] and ‘active matter’ in the form of living bacterial and alga suspensions [348–351]. Recently, there has been intense interest in understanding this generalized turbulence phenomenon [352]. Oyama and coworkers [341] and others [353,354] have shown in the context of flowing granular fluids that the vortices are comprised of clusters of particles moving in a string-like fashion and Liu et al. [310] have also shown this type of relationship between string-like motion and the vortices formed in deformed metallic glasses. We have confirmed that this hierarchical structure of the large-scale vortex patterns is composed of a finer structure involving cooperative atom exchange events and we will report our findings on this complex phenomenon in a separate paper devoted to this topic. This type of hierarchical structure has also been observed in GF liquids [6].

It should be apparent by now that glasses, GF liquids, and highly deformed materials generally, exhibit a rich dynamic that reflects the dynamic heterogeneity intrinsic to these materials, even in highly deformed crystalline materials [317,318,355], which embody arguably most forms of condensed matter. The dynamic formation and disintegration of structures in these materials (intermittency) imply that the material properties correspondingly exhibit large fluctuations, offering valuable information about the scale and geometry of the self-assembly processes underlying this spontaneous clustering arising from many-body dynamics. In practical terms, this means that basic properties such as potential energy become highly 'noisy' [355–357], and exhibit long range correlations in the form of colored noise and stress fluctuations and particle displacements exhibiting quake-like events having an exponential distribution in intensities and power-law distribution of occurrence are naturally observed in this type of system, even under equilibrium conditions. We have discussed this phenomenon at length in connection to the dynamics of the mobile particle clusters and Johari-Goldstein relaxation process in our previous work focussing on a Al-Sm metallic glass [227] and we have investigated this same rather generic phenomena in a variety of other materials such as interfacial dynamics of Ni nanoparticles [49], the interfacial dynamics of bulk crystalline Ni and ice [13,119,147] and internal dynamics of proteins [295].

Many others have studied this type of 'quake' phenomenon in deformed glass materials, [358,359] where clusters with geometric properties consistent with our mobile particle clusters were inferred to be the origin of this phenomenon. We also leave this interesting aspect of the highly deformed glass state for a future investigation. Here we point out that studies of noise offer much valuable information about the dynamic heterogeneity in this class of materials and this noise itself is of intrinsic interest in biology and various fields of material science where it is functional in relation to biological sensing and the catastrophic failure of materials [360–365].

Many studies have previously shown that the large fluctuations in the various types of systems exhibiting turbulent dynamics lead to transient anomalous diffusion in which the fluctuations accelerate the movement of particles in the system. We next show that the van Hove function describing atomic displacement in a highly deformed metallic glass exhibits rather typical behavior for this type of elastically turbulent system in the regime in which shear bands have formed. Given the potential practical importance of this phenomenon and the lack of previous quantification of this phenomenon in deformed metallic glass materials, we consider the particle has displaced a distance r from its initial position (taken at the origin) at time t, i.e., the van correlation function $G_s(r,t)$ in liquid state dynamics jargon in Figure 5.11 at the caging time at which $<u^2>$ is defined and at the time τ_M at which the mobile particles are defined, a time that also essentially coincides in our material with the peak time of the non-Gaussian parameter. The displacement at the caging time is nearly exactly described by a Gaussian function (see inset to Figure 5.11) where $<u^2>$ defines the atomic displacement on a ps timescale defining the caging time, but $G_s(r,t)$ at τ_M is clearly highly non-Gaussian. The 'fat tail' describing the particle displacement on intermediate is a rather universal characteristic of systems exhibiting the highly collective dynamics, as observed in the present material, and 'turbulent' systems broadly [366]. The long tail in this type of distribution has often been described by stretched exponential distributions [366,367], as in Richardson's original model of passive transport of particles in a turbulent medium [334,335], and sometimes this distribution is approximated as being exponential for simplicity. [349,368,369]

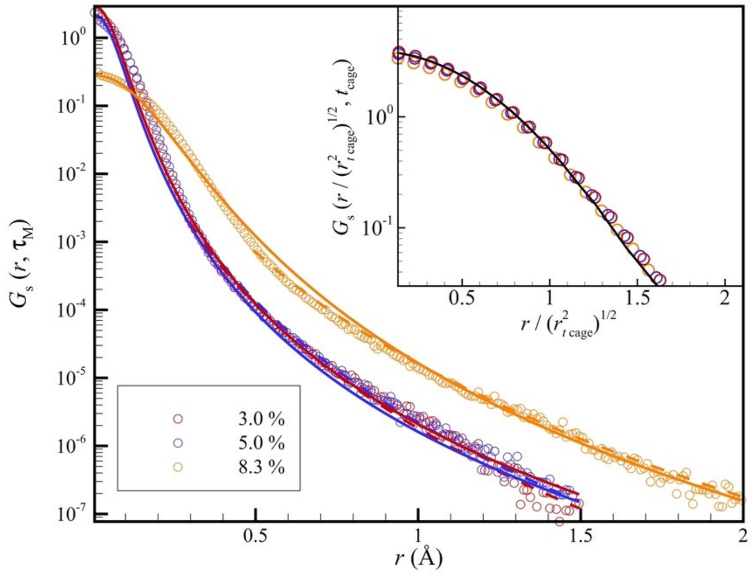

Figure 5.11 Van Hove correlation function with τ_M at $\varepsilon = 3.0$ %, 5.0%, and 8.3 %. The tail of the van Hove function is fit to the generalized Tsallis distribution [290,367] (solid lines), $G_s\ (r,t) \sim [1 - \beta\ (1 - q)\ r^{\delta}]^{1/(1-q)}$ where $q = 1.39$ and $\delta = 2.31$ for $\varepsilon = 3.0$ % and 5.0%, and $q = 1.32$ and $\delta = 2.2$ for $\varepsilon = 8.3$ %, respectively. The dashed curves indicate the apparent 'stretched exponential' tails of $G_s\ (r,t)$ where the stretching exponent β values are noted in the text. The inset shows the van Hove function at the same strains at the caging time, 1 ps where we have introduced a reduced displacement distance, $r / \langle u^2 \rangle^{1/2}$, and where the solid line is a Gaussian function. The particle displacements at this short time are remarkably similar to those found in perfect crystals at low temperatures and are typical generally for materials in equilibrium.

As noted before, we may expect the deformed metallic glass to be in a non-equilibrium state in which ordinary equilibrium thermodynamics does not necessarily apply. As in the case of ordinary turbulence, we follow precedent in this type of situation and fit $G_s(r,t)$ to a form expected from non-extensive thermodynamics, the thermodynamics appropriate in which the system is not quite ergodic, but not really periodic or regular in its dynamics either [288,289,340]. The solid line in Figure 5.12 shows a fit to the general Tsallis distribution, as prescribed by Eq. (15) of Beck [290]. We see that this distribution function, which has been shown to fit probability distribution functions for turbulent fluids and a variety of non-equilibrium systems, is rather well. The Tsallis theory [290,370] does not provide a specific prediction of the characteristic exponents describing the non-Gaussian distribution from first principles, but we may conclude again that the basic phenomenology that we observe for SB region is typical of 'turbulent' materials.

We note that the tail of $G_s(r,t)$ can also be reasonably well-described phenomenologically by a stretched exponential of index β, which jumps in its value from about $\beta = 0.2$ below the regime of SB formation to a value $\beta = 0.25$ near the point of SB formation, a phenomenon that reflects the sharp transition to a turbulent state in which the generation of a hierarchy of vortices that greatly influences the transport of particles on intermediate time and space scales. At very long timescales, we expect $G_s(r,t)$ for particle displacement to return to a Gaussian form, as seen also in ordinary turbulent, granular fluids, and nearly jammed fluids [337,338,371,372], and also observed in the context of simulations of deformed metallic glasses by Shrivastav et al. [238]

5.4 Conclusions

In the current study, we investigated the deformation mode in $Cu_{64}Zr_{36}$ alloys with different thicknesses and under different temperatures. A different deformation mode has been observed in these systems, which leads to a question: How to characterize the localized and non-localized deformation? Von Mises strains were implemented to monitor the formation of shear band. We found that the shear band gradually builds up inside the system and undergoes soften and harden process as we increase the strain. Eventually, one dominant shear band develops when the localized deformation mode occurs. Since the temperature when the deformation happens is relatively low, atomic diffusion is extremely slow and other processes should be expected to happen to influence the structural relaxation.

1. We first considered the average mean square displacement of our metallic glass deep in the glass state and found that dynamics in this regime seemed to greatly resemble that of crystalline materials at a temperature well below their meting point. In particular, the mean square particle displacement $<u^2>$ after a well-defined caging time, the 'Debye-Waller factor', is relatively small and increases nearly linearly with temperature. No detectable evolution of $<u^2>$ was observed in our metallic glass material, but we cannot exclude such a possibility on timescales longer than we could simulate.
2. The intermediate scattering function does not decay from the plateau determined by $<u^2>$ so no finite α-relaxation time appears to exist in the glass state. Experimental studies have established that the Johari-Goldstein relaxation time (τ_{JG}) exists in the glass state, however, and adopt criteria developed in previous papers investigating the Johari-Goldstein relaxation process in which the Johari-Goldstein relaxation time is identified with the mobile particle lifetime, τ_M), a well-defined form of dynamic heterogeneity [55] that exists both in the cooled liquid state above T_g and in the glass state well below T_g. This puts us in a position to investigate relaxation in the metallic glass and how relaxation is altered by material deformation. In the low temperature non-ergodic glass

state. In the glass-forming liquids, it was previously observed that the α-structural relaxation time (τ_α) from the long-time decay of the intermediate scattering function $F_s(q, t)$ seems to approach the caging time t_{cage} at high rates of deformation and correspondingly we investigated whether a similar trend might apply for the corresponding relaxation time τ_{JG} of the deformed metallic glass. We found that τ_{JG} indeed seems to approach the caging time in the limit of large deformation.

3. The local values of $<u^2>$ have long been interpreted physically as a measure of material local 'stiffness' in relation to the shear modulus of the material and at the scale of chemical bonds when values of $<u^2>$ at an atomic scale are estimated. This suggested the general use of $<u^2>$ as a measure of stiffness at any scale, although this usage of the term means that we may not think of this quantity as directly a measure of shear modulus. We first showed a strong correlation between the macroscopic elastic constant C_{11} as determined from the stress resulting from a low amplitude strain of the metallic glass material and the 'stiffness' measure $k_B T / <u^2>$. We then have firm evidence that $<u^2>$ provides good estimate of the shear stiffness of the material over a large temperature range, encompassing remarkably even the low temperature non-ergodic regime. We also considered estimates of local estimates of stiffness based on $<u^2>$ and local variations of stress and strain and an associated 'local elastic constant' $C_{11,i}$. Again, we found good consistency between the $<u^2>$ stiffness estimate of stiffness and the elasticity motivated definition, but, in this case, we can only claim qualitative a correlation since there is no unique way to define a local shear modulus in materials. By its very definition, $<u^2>$ is a good measure of stiffness at a molecular scale so the use of $<u^2>$ as general measure of stiffness on any length scale seems to be well-supported in our metallic glass system.

4. It has long been thought that SB formation in amorphous solids initiates from relatively 'soft' regions in the material at which large scale non-affine deformations become localized. The test of this hypothesis requires an effective means of identifying 'soft' regions and their evolution as the material is deformed to varying degrees, where the metric of 'softness' must also account for the effect of temperature on local material stiffness. We defined a precise local measure, of 'softness' ζ, defined in terms of material stiffness and find a sharp change in ζ at a critical strain value at which shear banding initiates. In particular, we find that the critical strain condition for SB formation occurs when the softness ($<u^2>$) distribution within the emerging soft regions approaches that of the interfacial region in its undeformed state, initiating an instability. Correspondingly, no SBs arise when the material is so thin that the entire material can be approximately described as being 'interfacial' in nature.
5. The development of a SB, as in the case of crack formation, involves the emergence of an interface within the material. Correspondingly, we found that the dynamics within the incipient SB region is similar to the free interfacial region of the material, again supporting the existence of an interfacial instability.
6. Based on an observed relationship between the mobile particle cluster lifetime [227] and many observations correlating the JG relaxation process to hypothetical shear transformation zones in glass materials [226], we make the tentative hypothesis that the mobile particle clusters provide well-defined realization of the hypothetical STZs. This identification remains to be tested to validate other attributes of the STZs that have been suggested by recent studies, such as a multipole stress field that plays a large role in the organization of the shear bands. [229,230]

7. We briefly examined the dynamics in the deformation range beyond the onset of shear band formation and find that the structure and dynamics of the material becomes very complex in this region, and we plan to discuss this regime in some detail in a subsequent paper. In the present work, however, we emphasize some significant changes in the nature of the atomic displacement distribution as one undergoes shear band formation. In particular, we find that at large deformations, particle displacement becomes *super-diffusive* beyond a caging regime and the atoms remain localized and nearly Gaussian in a fashion similar to crystalline materials in the caging regime at shorter times. The fully formed shear band regions become highly dynamically heterogeneous (a phenomenon quantified by researchers before us [317,318,355]) and here we focus on the change in the probability of particle displacement, the so called Van Hove function $G_s(r,t)$, as one passes through the SB transition. We find that $G_s(r,t)$ develops an extended 'fat tail' near the yield stain at which shear bands emerge where this extended tail quantifies the greatly enhanced probability for the atoms in the shear band to exhibit jumps to large distances. We interpret this 'fat tail' to arise from the particles being convicted along by the movement of large-scale vortices in the shear band region, as in diverse other fluids exhibiting 'turbulence'. Since the shear band state corresponds to non-equilibrium state similar in some ways to turbulent fluids, we fit $G_s(r,t)$ to a general functional form ($[1 - \beta (1 - q) r^{\delta}]^{1/(1-q)}$ [290] that commonly arises in probability distributions in turbulent systems and we find that this type of functional form fits our $G_s(r,t)$ very well, but as in turbulent fluids where the same type of fitting has often been made previously, the physical meaning of the fitting parameters is not clear. These observations nonetheless hint at some sort of 'universality' in the atomic dynamics in the shear band state and provide

insights into the thermodynamic nature of the non-ergodic glass state. We look forward to further quantifying this novel form of ‘elastic turbulence’ in the future. Our findings seem to confirm the suggestion made long ago by Taylor [269] that the heterogeneities of turbulent liquids and the formation of heterogeneous structures (“aggregates’) in the deformation of polycrystalline materials should have much in common. Our observations also appear complementary to those of Dauchet and Bertin [373] who have recently emphasized the strong analogies between glass-formation and the transition to turbulence in fluids at high Reynolds number based on a combination of phenomenology, energy landscape and dynamical systems ideas.

6. Conclusions and Suggestions for Future Work

Throughout the work, we have studied dynamic heterogeneity existed in the interfacial region of ice, metallic GF liquids over a wide range of temperatures and metallic glasses under uniaxial deformation with different thicknesses.

The string-like cooperative motion and self-diffusion on ice $(11\bar{2}0)$ free surface was examined in Chapter 3. And the dynamics of the interfacial were quantified using the tools drawn from the GF liquids. For the wide range of T studied, we found that the amplitude of atomic motion in the interfacial region exhibited significantly larger than in the interior, explicating the "premelting" phenomenon and the initiation of heterogeneous nucleation of crystal melting. Utilizing non-Gaussian parameter, the self-part of van Hove correlation functions, surface diffusion coefficients, and self-intermediate scattering function of the interfacial atoms. A similar trend has been observed before in the (110) interfacial region of Ni. The interfacial dynamics of ice certainly resemble the characteristic dynamics of GF liquids in many ways. In all the GF liquids that we have investigated before, string-like cooperative motion has proved to be a universal feature.

The dynamic heterogeneity has been systematically examined in model metallic GF liquids, and the results have been compared with previous findings in a simulated polymeric GF liquid. We utilized algorithm developed by Starr et al.[55] to identify mobile and immobile particles and clusters with extreme mobility to prove the universality of the methodology on different chemistry and compositions of metallic glasses. The "decoupling" relation between the diffusion coefficient and the structural relaxation time has been examined in all the studied metallic fluids. We concluded that GF liquids evidently share general characteristics in the structural and chemical dynamics.

The deformation mode in $Cu_{64}Zr_{36}$ alloys with different thicknesses and under different temperatures have been investigated. A different deformation mode has been observed in these systems. Von Mises strains were utilized to track the formation of shear band. And we concluded that before one dominant band eventually penetrates the sample the shear band constantly changes and undergoes soften and harden processes as the strain increases. Then the factors could influence the relaxation process have been explored. Similar to crystalline and metallic GF liquids at finite temperatures a defined 'caging' time can be identified by observing the variation in the Debye-Waller factor $<u^2>$. We have interpreted $<u^2>$ as a measure of material local stiffness and confirm its applicability by comparing the local elastic constant with the proposed parameter $k_B\ T\ /\ <u^2>$. Based on the common understanding on the SB formation in amorphous solid, we have proposed a local measure of 'softness' and observed a clear percolation transition in the SB region. The increase in the strain leads to the drop in the mobile cluster lifetime and growth in the cluster size. The fully formed shear band shows dynamic heterogeneity.

Since we have observed that the structure and dynamics of the deformed metallic GF liquids become very complex in the SB region, further investigation and discussion on the changes in structural and dynamical properties need to be done. From a macroscopic aspect, the deformation of MG is highly correlated with strain rate and temperature. In the currant work, low temperatures and relatively high strain rate has been applied and resulted in the formation of SB. At higher temperatures, homogeneous deformation mode occurs within the supercooled liquid regions. [374] The deformation mechanisms still have unsolved matters. In crystalline materials, deformation mechanism and mechanical properties can be interpreted using atomic structures like dislocations, defects and other electronic structures. However, in MGs the lack of long-range order and amorphous structure have hindered the way to fully understand the ultimate mechanical failure i.e., the formation of shear band. On a microscopic level, Shear band transformation zone involving hundreds of atoms mediating the plastic deformation has been proposed to explain the deformation mode. [374] In the current work we have established the findings that shear band usually initiate at soft spots, but how do these soft spots evolve into shear band? What is the activation mechanism underlying this phenomenon? These considerable complex and various fundamental questions about the deformation mechanism remain open and await answers.

String-like cooperative motion plays an important role in the relaxation above glass-transition temperature, and we wonder whether this mode is similarly important in materials under large deformation and temperature well below glass-transition temperature. It has been established that string-like cooperative motion is associated with diffusion and structural relaxation. However, diffusion in the glass state is generally limited, then we suspect that the large strain may act as the source. Based on the STZ model proposed by Argon [375], shear deformation happens accompanied by small clusters going through the spontaneous and collective rearranging motion. In the study of structural relaxation of Cu-Zr alloys, Zhang et al. establish that dynamic heterogeneity essentially originates from packing fluctuation when some particles localize into preferred packing configurations with lower free energy and leaving a large position of mobile atoms with high free energy. The atomic motion of such a large fraction of "wandering" particles are often highly collective. [28] Since the cooperative nature of atomic displacements inside STZs, it is reasonable to correlate these soft regions with string-like cooperative motion. Further examinations will focus on this correlation.

Debye-Waller factor $<u^2>$ as the mean squared atomic displacement after a fix decorrelation time characterizing the transfer from ballistic motion to caged atomic motion has been interpreted as local material stiffness in the current work. It also provides a very simple method to estimate the characteristic temperatures during the glass transition. Hall and Wolynes have developed the relation between τ_α and $<u^2>$, $\tau_\alpha \sim exp(u_0/\langle u^2 \rangle)$, based on the framework of RFOT theory. [145,376] It has become appreciated that extrapolation of $<u^2>$ could predict several characteristic temperatures such as glass-transition temperature, crossover temperature, and onset temperatures. [28] Usually a more complex calculation would be required for such estimation, but $<u^2>$ provides a remarkable and straightforward method and empowers greater confidence in the estimation of these fundamental and important timescales. In the future work, I plan to explore the applicability of the Debye-Waller factor as a measure of local stiffness in different metallic GF liquids with different compositions, glass-forming abilities.

References

[1] L. Xia, W.H. Li, S.S. Fang, B.C. Wei, and Y.D. Dong, J. Appl. Phys. **99**, 26103 (2006).

[2] Y.Q. Cheng and E. Ma, Prog. Mater. Sci. **56**, 379 (2011).

[3] P. Jenniskens and D.F. Blake, Science (80-.). **265**, 753 (1994).

[4] A.A. Reka, B. Pavlovski, K. Lisichkov, A. Jashari, B. Boev, I. Boev, M. Lazarova, V. Eskizeybek, A. Oral, and P. Makreski, Geol. Croat. **72**, 215 (2019).

[5] R. Busch, J. Schroers, and W.H. Wang, Mrs Bull. **32**, 620 (2007).

[6] B.A. Pazmiño Betancourt, F.W. Starr, and J.F. Douglas, J. Chem. Phys. **148**, 104508 (2018).

[7] K.L. Ngai, *Relaxation and Diffusion in Complex Systems* (Springer Science & Business Media, 2011).

[8] P.G. Debenedetti and F.H. Stillinger, Nature **410**, 259 (2001).

[9] C.A. Angell, K.L. Ngai, G.B. McKenna, P.F. McMillan, and S.W. Martin, J. Appl. Phys. **88**, 3113 (2000).

[10] F. Faupel, W. Frank, M.-P. Macht, H. Mehrer, V. Naundorf, K. Rätzke, H.R. Schober, S.K. Sharma, and H. Teichler, Rev. Mod. Phys. **75**, 237 (2003).

[11] S. Capaccioli, M. Paluch, D. Prevosto, L.-M. Wang, and K.L. Ngai, J. Phys. Chem. Lett. **3**, 735 (2012).

[12] R.C. Zeller and R.O. Pohl, Phys. Rev. B **4**, 2029 (1971).

[13] H. Zhang and J.F. Douglas, Soft Matter **9**, 1254 (2013).

[14] P.W. Anderson, B.I. Halperin, and C.M. Varma, Philos. Mag. **25**, 1 (1972).

[15] W.A. Phillips, J. Low Temp. Phys. **11**, 757 (1973).

[16] H.-B. Yu, K. Samwer, Y. Wu, and W.H. Wang, Phys. Rev. Lett. **109**, 95508 (2012).

[17] K. Binder and W. Kob, *Glassy Materials and Disordered Solids: An Introduction to Their Statistical Mechanics* (World scientific, 2011).

[18] R.A. Riggleman, J.F. Douglas, and J.J. de Pablo, Phys. Rev. E **76**, 11504 (2007).

[19] Y. Cohen, S. Karmakar, I. Procaccia, and K. Samwer, EPL (Europhysics Lett. **100**, 36003 (2012).

[20] J.S. Tse, D.D. Klug, C.A. Tulk, E.C. Svensson, I. Swainson, V.P. Shpakov, and V.R. Belosludov, Phys. Rev. Lett. **85**, 3185 (2000).

[21] M. Russina, F. Mezei, R. Lechner, S. Longeville, and B. Urban, Phys. Rev. Lett. **84**, 3630 (2000).

[22] L. Larini, A. Ottochian, C. De Michele, and D. Leporini, Nat. Phys. **4**, 42 (2007).

[23] K.L. Ngai, Phys. Rev. E **57**, 7346 (1998).

[24] K.L. Ngai and S. Capaccioli, Phys. Rev. E **69**, 31501 (2004).

[25] G.P. Johari and M. Goldstein, J. Chem. Phys. **53**, 2372 (1970).

[26] W. Kob and H.C. Andersen, Phys. Rev. E **52**, 4134 (1995).

[27] M.S. Shell, P.G. Debenedetti, and F.H. Stillinger, J. Phys. Condens. Matter **17**, S4035 (2005).

[28] H. Zhang, C. Zhong, J.F. Douglas, X. Wang, Q. Cao, D. Zhang, and J.-Z. Jiang, J. Chem. Phys. **142**, 164506 (2015).

[29] B.A.P. Betancourt, J.F. Douglas, and F.W. Starr, J. Chem. Phys. **140**, 204509 (2014).

[30] A.S. Keys, A.R. Abate, S.C. Glotzer, and D.J. Durian, Nat. Phys. **3**, 260 (2007).

[31] E.R. Weeks, J.C. Crocker, A.C. Levitt, A. Schofield, and D.A. Weitz, Science (80-.). **287**, 627 (2000).

[32] S. Gokhale, K.H. Nagamanasa, R. Ganapathy, and A.K. Sood, Nat. Commun. **5**, 1 (2014).

[33] M.H. Cohen and D. Turnbull, J. Chem. Phys. **31**, 1164 (1959).

[34] E. Leutheusser, Phys. Rev. A **29**, 2765 (1984).

[35] U. Bengtzelius, W. Gotze, and A. Sjolander, J. Phys. C Solid State Phys. **17**, 5915 (1984).

[36] G. Adam and J.H. Gibbs, J. Chem. Phys. **43**, 139 (1965).

[37] T.R. Kirkpatrick, D. Thirumalai, and P.G. Wolynes, Phys. Rev. A **40**, 1045 (1989).

[38] V. Lubchenko and P.G. Wolynes, Annu. Rev. Phys. Chem. **58**, 235 (2007).

[39] J.-P. Bouchaud and G. Biroli, J. Chem. Phys. **121**, 7347 (2004).

[40] J.F. Douglas, J. Dudowicz, and K.F. Freed, J. Chem. Phys. **125**, 144907 (2006).

[41] P.Z. Hanakata, B.A.P. Betancourt, J.F. Douglas, and F.W. Starr, J. Chem. Phys. **142**, 234907 (2015).

[42] P.Z. Hanakata, J.F. Douglas, and F.W. Starr, Nat. Commun. **5**, 4163 (2014).

[43] J.F. Douglas, B.A.P. Betancourt, X. Tong, and H. Zhang, J. Stat. Mech. Theory Exp. **2016**, 54048 (2016).

[44] T. Rouxel, J. Am. Ceram. Soc. **90**, 3019 (2007).

[45] H. Zhang, D.J. Srolovitz, J.F. Douglas, and J.A. Warren, Proc. Natl. Acad. Sci. **106**, 7735 (2009).

[46] R.A. Riggleman, K. Yoshimoto, J.F. Douglas, and J.J. de Pablo, Phys. Rev. Lett. **97**, 45502 (2006).

[47] H. Zhang, D.J. Srolovitz, J.F. Douglas, and J.A. Warren, Acta Mater. **55**, 4527 (2007).

[48] H. Zhang, Y. Yang, and J.F. Douglas, J. Chem. Phys. **142**, 84704 (2015).

[49] H. Zhang, P. Kalvapalle, and J.F. Douglas, Soft Matter **6**, 5944 (2010).

[50] H. Zhang, M. Khalkhali, Q. Liu, and J.F. Douglas, J. Chem. Phys. **138**, 12A538 (2013).

[51] H.R. Schober, C. Oligschleger, and B.B. Laird, J. Non. Cryst. Solids **156**, 965 (1993).

[52] C. Oligschleger and H.R. Schober, Phys. Rev. B **59**, 811 (1999).

[53] N. Giovambattista, S. V Buldyrev, F.W. Starr, and H.E. Stanley, Phys. Rev. Lett. **90**, 85506 (2003).

[54] L. Xu, F. Mallamace, Z. Yan, F.W. Starr, S. V Buldyrev, and H.E. Stanley, Nat. Phys. **5**, 565 (2009).

[55] F.W. Starr, J.F. Douglas, and S. Sastry, J. Chem. Phys. **138**, 12A541 (2013).

[56] W.C. Swope, H.C. Andersen, P.H. Berens, and K.R. Wilson, J. Chem. Phys. **76**, 637 (1982).

[57] L. Verlet, Phys. Rev. **159**, 98 (1967).

[58] M.I. Mendelev, M.J. Kramer, R.T. Ott, D.J. Sordelet, D. Yagodin, and P. Popel, Philos. Mag. **89**, 967 (2009).

[59] M.S. Daw, S.M. Foiles, and M.I. Baskes, Mater. Sci. Reports **9**, 251 (1993).

[60] M.P. Allen and D.J. Tildesley, *Computer Simulation of Liquids* (Oxford university press, 2017).

[61] W.G. Hoover, Phys. Rev. A **31**, 1695 (1985).

[62] S. Nosé, J. Chem. Phys. **81**, 511 (1984).

[63] M. Parrinello and A. Rahman, J. Appl. Phys. **52**, 7182 (1981).

[64] H.C. Andersen, J. Chem. Phys. **72**, 2384 (1980).

[65] G.J. Martyna, D.J. Tobias, and M.L. Klein, J. Chem. Phys. **101**, 4177 (1994).

[66] U.R. Pedersen, (2009).

[67] W. Kob and H.C. Andersen, Phys. Rev. E **51**, 4626 (1995).

[68] C. Donati, J.F. Douglas, W. Kob, S.J. Plimpton, P.H. Poole, and S.C. Glotzer, Phys. Rev. Lett. **80**, 2338 (1998).

[69] A. Rahman, K.S. Singwi, and A. Sjölander, Phys. Rev. **126**, 986 (1962).

[70] T. Kanaya, I. Tsukushi, and K. Kaji, Prog. Theor. Phys. Suppl. **126**, 133 (1997).

[71] W.S. Xu, J.F. Douglas, and K.F. Freed, Macromolecules **49**, 8355 (2016).

[72] B.A.P. Betancourt, J.F. Douglas, and F.W. Starr, Soft Matter **9**, 241 (2013).

[73] L. Berthier, Phys. Rev. Lett. **91**, 55701 (2003).

[74] L. Berthier, G. Biroli, J.-P. Bouchaud, and R.L. Jack, Dyn. Heterog. Glas. Colloids, Granul. Media **150**, 68 (2011).

[75] G.H.J.A. Tammann, *Lehrbuch Der Metallkunde; Chemie Und Physik Der Metalle Und Ihrer Legierungen* (1932).

[76] R. Merkle and J. Maier, Z. Anorg. Allg. Chem. **631**, 1163 (2005).

[77] S.E. Golunski, Platin. Met. Rev. **51**, 162 (2007).

[78] J.G. Dash, A.W. Rempel, and J.S. Wettlaufer, Rev. Mod. Phys. **78**, 695 (2006).

[79] J.G. Dash, H.Y. Fu, and J.S. Wettlaufer, Rep. Prog. Phys. **58**, 115 (1995).

[80] R. Rosenberg, Phys. Today **58**, 50 (2005).

[81] Y. Li and G.A. Somorjai, J. Phys. Chem. C **111**, 9631 (2007).

[82] M.J. Molina, Angew. Chem., Int. Ed. Engl. **35**, 1778 (1996).

[83] J.S. Wettlaufer and J.G. Dash, Sci. Am. **282**, 50 (2000).

[84] M. Faraday, Philos. Mag. **17**, 162 (1859).

[85] M. Faraday, The Athenaeum 640 (1850).

[86] H. Bluhm, D.F. Ogletree, C.S. Fadley, Z. Hussain, and N. Salmeron, J. Phys. Condens. Matter **14**, L227 (2002).

[87] M.A. Sanchez, Proc. Natl. Acad. Sci. U. S. A. **114**, 227 (2017).

[88] C. Vega, J.L.F. Abascal, M.M. Conde, and J.L. Aragones, Faraday Discuss. **141**, 251 (2009).

[89] J.L.F. Abascal and C. Vega, J. Chem. Phys. **123**, 234505 (2005).

[90] M.M. Conde, C. Vega, and A. Patrykiejew, J. Chem. Phys. **129**, 14702 (2008).

[91] M. Watkins, D. Pan, E.G. Wang, A. Michaelides, J. VandeVondele, and B. Slater, Nat. Mater. **10**, 794 (2011).

[92] L. Ojamae, Nat. Mater. **10**, 725 (2011).

[93] D.T. Limmer and D. Chandler, J. Chem. Phys. **141**, 18C505 (2014).

[94] W.J. Smit and H.J. Bakker, Angew. Chem., Int. Ed. **56**, 1 (2017).

[95] C. Vega and J.L.F. Abascal, Phys. Chem. Chem. Phys. **13**, 19663 (2011).

[96] C. Vega, M. Martin-Conde, and A. Patrykiejew, Mol. Phys. **104**, 3583 (2006).

[97] E. Guillaud, S. Merabia, D. de Ligny, and L. Joly, Phys. Chem. Chem. Phys. **19**, 2124 (2017).

[98] S.A. Nose, J. Chem. Phys. **81**, 511 (1984).

[99] S. Plimpton, J. Comput. Phys. **117**, 1 (1995).

[100] W. Pfalzgraff, S. Neshyba, and M. Roeselova, J. Phys. Chem. A **115**, 6184 (2011).

[101] A.M. Alsayed, M.F. Islam, J. Zhang, P.J. Collings, and A.G. Yodh, Science (80-.). **309**, 1207 (2005).

[102] F. Klameth and M. Vogel, J. Chem. Phys. **138**, 134503 (2013).

[103] I. Golecki and C. Jaccard, J. Phys. C Solid State Phys. **11**, 4229 (1978).

[104] M.T. Suter, P.U. Andersson, and J.B.C. Pettersson, J. Chem. Phys. **125**, 174704 (2006).

[105] T. Ikeda-Fukazawa and K. Kawamura, J. Chem. Phys. **120**, 1395 (2004).

[106] L. Van Hove, Phys. Rev. **95**, 249 (1954).

[107] P. Hopkins, A. Fortini, A.J. Archer, and M. Schmidt, J. Chem. Phys. **133**, 224505 (2010).

[108] J.P. Hansen and I.R. McDonald, *Theory of Simple Liquids* (1986).

[109] R. Zangi and S.A. Rice, Phys. Rev. Lett. **92**, 35502 (2004).

[110] C. Donati, S.C. Glotzer, P.H. Poole, W. Kob, and S.J. Plimpton, Phys. Rev. E **60**, 3107 (1999).

[111] T.O.E. Skinner, D. Aarts, and R.P.A. Dullens, J. Chem. Phys. **135**, 5 (2011).

[112] K.H. Nagamanasa, R. Ganapathy, S. Gokhale, and A.K. Sood, Proc. Natl. Acad. Sci. U. S. A. **108**, 11323 (2011).

[113] Y. Yang, H. Zhang, and J.F. Douglas, ACS Nano **8**, 7465 (2014).

[114] N. Giovambattista, M.G. Mazza, S. V Buldyrev, F.W. Starr, and H.E. Stanley, J. Phys. Chem. B **108**, 6655 (2004).

[115] N. Giovambattista, S. V Buldyrev, H.E. Stanley, and F.W. Starr, Phys. Rev. E **72**, 11202 (2005).

[116] H.P. Bonzel and E.E. Latta, Surf. Sci. **76**, 275 (1978).

[117] H.P. Bonzel, Surf. Sci. **21**, 45 (1970).

[118] E.G. Seebauer and C.E. Allen, Prog. Surf. Sci. **49**, 265 (1995).

[119] H. Zhang and J.F. Douglas, Soft Matter **9**, 1266 (2013).

[120] P. Henritzi, A. Bormuth, F. Klameth, and M. Vogel, J. Chem. Phys. **143**, 164502 (2015).

[121] J.F. Douglas and D. Leporini, J. Non-Cryst. Solids **235**, 137 (1998).

[122] H. Zhang, P. Kalvapalle, and J.F. Douglas, J. Phys. Chem. B **115**, 14068 (2011).

[123] E.J. Haddadian, H. Zhang, K.F. Freed, and J.F. Douglas, Sci. Rep. **7**, 41671 (2017).

[124] C. Reichhardt and C.J.O. Reichhardt, Phys. Rev. Lett. **93**, 176405 (2004).

[125] C. Reichhardt and C.J.O. Reichhardt, Phys. Rev. Lett. **90**, 95504 (2003).

[126] D.L. Turcotte, *Fractals and Chaos in Geology and Geophysics* (1997).

[127] F.W. Starr and J.F. Douglas, Phys. Rev. Lett. **106**, 115702 (2011).

[128] B.A.P. Betancourt, P.Z. Hanakata, F.W. Starr, and J.F. Douglas, Proc. Natl. Acad. Sci. **112**, 2966 (2015).

[129] W.S. Xu, J.F. Douglas, and K.F. Freed, ACS Macro Lett. **5**, 1375 (2016).

[130] W.S. Xu, J.F. Douglas, and K.F. Freed, Macromolecules **50**, 2585 (2017).

[131] W.S. Xu, J.F. Douglas, and K.F. Freed, J. Chem. Phys. **145**, 234509 (2016).

[132] R.H. Doremus, J. Appl. Phys. **92**, 7619 (2002).

[133] J. Zhao, S.L. Simon, and G.B. McKenna, Nat. Commun. **4**, 1783 (2013).

[134] G. Foffi, G. Savin, S. Bucciarelli, N. Dorsaz, G.M. Thurston, A. Stradner, and P. Schurtenberger, Proc. Natl. Acad. Sci. U. S. A. **111**, 16748 (2014).

[135] F.W. Starr, B. Hartmann, and J.F. Douglas, Soft Matter **10**, 3036 (2014).

[136] N. Shafique, K.E. Kennedy, J.F. Douglas, and F.W. Starr, J. Phys. Chem. B **120**, 5172 (2016).

[137] W. Luo, B. Johansson, O. Eriksson, S. Arapan, P. Souvatzis, M.I. Katsnelson, and R. Ahuja, Proc. Natl. Acad. Sci. U. S. A. **107**, 9962 (2010).

[138] A.B. Belonoshko, T. Lukinov, J. Fu, J.J. Zhao, S. Davis, and S.I. Simak, Nat. Geosci. **10**, 312 (2017).

[139] L. Vocadlo, D. Alfe, M.J. Gillan, I.G. Wood, J.P. Brodholt, and G.D. Price, Nature **424**, 536 (2003).

[140] M. Matsui and G.D. Price, Nature **351**, 735 (1991).

[141] M. Okeeffe and J.O. Bovin, Science (80-.). **206**, 599 (1979).

[142] L. I, W.T. Juan, C.H. Chiang, and J.H. Chu, Science (80-.). **272**, 1626 (1996).

[143] H. Kang, T.R. Kirkpatrick, and D. Thirumalai, Phys. Rev. E **88**, 42308 (2013).

[144] P. Gadige, D. Saha, S.K. Behera, and R. Bandyopadhyay, Sci. Rep. **7**, 8017 (2017).

[145] F.W. Starr, S. Sastry, J.F. Douglas, and S.C. Glotzer, Phys. Rev. Lett. **89**, 125501 (2002).

[146] H. Zhang, X.Y. Wang, A. Chremos, and J.F. Douglas, J. Chem. Phys. **150**, 174506 (2019).

[147] X. Wang, X. Tong, H. Zhang, and J.F. Douglas, J. Chem. Phys. **147**, 194508 (2017).

[148] M. Peyrard, Acta. Phys. Pol., B **25**, 955 (1994).

[149] A. Widmer-Cooper and P. Harrowell, J. Non-Cryst. Solids **352**, 5098 (2006).

[150] S. Bernini, F. Puosi, and D. Leporini, J. Non-Cryst. Solids **407**, 29 (2015).

[151] S. Bernini, F. Puosi, and D. Leporini, J. Chem. Phys. **142**, 124504 (2015).

[152] Y. Liu, D. Wang, K. Nakajima, W. Zhang, A. Hirata, T. Nishi, A. Inoue, and M. Chen, Phys. Rev. Lett. **106**, 125504 (2011).

[153] P. Tsai, K. Kranjc, and K.M. Flores, Acta Mater. **139**, 11 (2017).

[154] N. Wang, J. Ding, P. Luo, Y. Liu, L. Li, and F. Yan, Mater. Res. Lett. **6**, 655 (2018).

[155] H.B. Yu, W.H. Wang, H.Y. Bai, and K. Samwer, Natl. Sci. Rev. **1**, 429 (2014).

[156] F. Zhu, H. Nguyen, S. Song, D.P. Aji, A. Hirata, H. Wang, K. Nakajima, and M. Chen, Nat. Commun. **7**, 11516 (2016).

[157] A. Argon, Acta Met. **27**, 47 (1979).

[158] J. Ding, Y.-Q. Cheng, H. Sheng, M. Asta, R.O. Ritchie, and E. Ma, Nat. Commun. **7**, 13733 (2016).

[159] T. Egami, Prog. Mater. Sci. **56**, 637 (2011).

[160] F. Spaepen, Acta Met. **25**, 407 (1977).

[161] S.H. Glarum, J. Chem. Phys. **33**, 639 (1960).

[162] J.T. Bendler and M.F. Shlesinger, J. Mol. Liq. **36**, 37 (1987).

[163] C.A. Angell and K.J. Rao, J. Chem. Phys. **57**, 470 (1972).

[164] A. V Granato and V.A. Khonik, Phys. Rev. Lett. **93**, 155502 (2004).

[165] G.S. Grest and M.H. Cohen, Adv. Chem. Phys. **48**, 455 (1981).

[166] J.D. Ferry, *Viscoelastic Properties of Polymers* (1980).

[167] J. Bosse, W. Gotze, and M. Lucke, Phys. Rev. A **17**, 434 (1978).

[168] W. Gotze, Condens. Matter Phys. **4**, 873 (1998).

[169] G.H. Fredrickson and H.C. Andersen, Phys. Rev. Lett. **53**, 1244 (1984).

[170] Y. Jung, J.P. Garrahan, and D. Chandler, J. Chem. Phys. **123**, 84509 (2005).

[171] C.A. Angell and C.T. Moynihan, Met. Mater. Trans. B **31**, 587 (2000).

[172] M. Isobe, A.S. Keys, D. Chandler, and J.P. Garrahan, Phys. Rev. Lett. **117**, 145701 (2016).

[173] L. Berthier and G. Biroli, Rev. Mod. Phys. **83**, 587 (2011).

[174] R. Richert, J. Phys. Condens. Matter **14**, R703 (2002).

[175] Y. Deng, D. Wen, Y. Li, J. Liu, and P. Peng, Philos. Mag. **98**, 2861 (2018).

[176] R.C. Ruhl, B.C. Giessen, M. Cohen, and N.J. Grant, Acta Met. **15**, 1693 (1967).

[177] M. Leonhardt, W. Loser, and H.G. Lindenkreuz, Acta Mater. **47**, 2961 (1999).

[178] D. Wei, J. Yang, M.-Q. Jiang, L.-H. Dai, Y.-J. Wang, J.C. Dyre, I. Douglass, and P. Harrowell, J. Chem. Phys. **150**, 114502 (2019).

[179] C. Suryanarayana and A. Inoue, *Bulk Metallic Glasses* (2017).

[180] T.S. Ingebrigtsen, J.C. Dyre, T.B. Schrøder, and C.P. Royall, Phys. Rev. X **9**, 31016 (2019).

[181] J. Colmenero, J. Phys. Condens. Matter **27**, 22 (2015).

[182] Y. Zhang, R. Ashcraft, M. Mendelev, C. Wang, and K. Kelton, J. Chem. Phys. **145**, 204505

(2016).

[183] S. Foiles, M. Baskes, and M.S. Daw, Phys. Rev. B **33**, 7983 (1986).

[184] H. Sheng, https://sites.google.com/site/eampotentials/Home/P (n.d.).

[185] K. Lad, N. Jakse, and A. Pasturel, J. Chem. Phys. **136**, 104509 (2012).

[186] M. Cohen and D. Turnbull, Nature **189**, 131 (1961).

[187] T. Xu, X. Wang, H. Zhang, Q. Cao, D. Zhang, and J. Jiang, J. Chem. Phys. **147**, 144503 (2017).

[188] N. Saunders, Calphad **9**, 297 (1985).

[189] J.-L. Barrat, J. Baschnagel, and A. Lyulin, Soft Matter **6**, 3430 (2010).

[190] J.D. Stevenson, J. Schmalian, and P.G. Wolynes, Nat. Phys. **2**, 268 (2006).

[191] D. Stauffer and A. Aharony, *Introduction to Percolation Theory* (2018).

[192] D.J. Audus, F.W. Starr, and J.F. Douglas, J. Chem. Phys. **144**, 74901 (2016).

[193] H.-B. Yu, R. Richert, and K. Samwer, Sci. Adv. **3**, e1701577 (2017).

[194] W.G. Zhang, F.W. Starr, and J.F. Douglas, J. Phys. Chem. B **123**, 5935 (2019).

[195] N. Lacevic, F.W. Starr, T.B. Schroder, and S.C. Glotzer, J. Chem. Phys. **119**, 7372 (2003).

[196] R.A. Laviolette and F.H. Stillinger, J. Chem. Phys. **83**, 4079 (1985).

[197] Z.H. Jin, P. Gumbsch, K. Lu, and E. Ma, Phys. Rev. Lett. **87**, 55703 (2001).

[198] M.T. Cicerone, Q. Zhong, and M. Tyagi, Phys. Rev. Lett. **113**, 117801 (2014).

[199] C. Toninelli, M. Wyart, L. Berthier, G. Biroli, and J.-P. Bouchaud, Phys. Rev. E **71**, 41505 (2005).

[200] J.F. Douglas and J.B. Hubbard, Macromolecules **24**, 3163 (1991).

[201] J.F. Douglas, Comput. Mater. Sci. **4**, 292 (1995).

[202] E.B. Stukalin, J.F. Douglas, and K.F. Freed, J. Chem. Phys. **129**, 94901 (2008).

[203] T. Bauer, P. Lunkenheimer, and A. Loidl, Phys. Rev. Lett. **111**, 225702 (2013).

[204] E. Flenner, H. Staley, and G. Szamel, Phys. Rev. Lett. **112**, 97801 (2014).

[205] M. Wyart and M.E. Cates, Phys. Rev. Lett. **119**, 195501 (2017).

[206] S. Karmakar, C. Dasguptaa, and S. Sastry, Proc. Natl. Acad. Sci. U. S. A. **106**, 3675 (2009).

[207] J. Dudowicz, K.F. Freed, and J.F. Douglas, Adv. Chem. Phys. **137**, 125 (2008).

[208] E.B. Stukalin, J.F. Douglas, and K.F. Freed, J. Chem. Phys. **131**, 114905 (2009).

[209] K. Kunal, C.G. Robertson, S. Pawlus, S.F. Hahn, and A.P. Sokolov, Macromolecules **41**, 7232 (2008).

[210] F. Vargas-Lara, B.A.P. Betancourt, and J.F. Douglas, J. Chem. Phys. **150**, 101103 (2019).

[211] A.L. Greer, Y.Q. Cheng, and E. Ma, Mater. Sci. Eng. R Reports **74**, 71 (2013).

[212] D. Jang and J.R. Greer, Nat. Mater. **9**, 215 (2010).

[213] C.E. Packard and C.A. Schuh, Acta Mater. **55**, 5348 (2007).

[214] M.F. Ashby and A.L. Greer, Scr. Mater. **54**, 321 (2006).

[215] N.P. Bailey, J. Schiøtz, and K.W. Jacobsen, Phys. Rev. B **73**, 64108 (2006).

[216] Q.-K. Li and M. Li, Appl. Phys. Lett. **88**, 241903 (2006).

[217] Y.Q. Cheng, E. Ma, and H.W. Sheng, Phys. Rev. Lett. **102**, 245501 (2009).

[218] E. Pekarskaya, C.P. Kim, and W.L. Johnson, J. Mater. Res. **16**, 2513 (2001).

[219] C.A. Schuh, T.C. Hufnagel, and U. Ramamurty, Acta Mater. **55**, 4067 (2007).

[220] A.S. Argon, R.D. Andrews, J.A. Godrick, and W. Whitney, J. Appl. Phys. **39**, 1899 (1968).

[221] A. Shavit and R.A. Riggleman, Phys. Chem. Chem. Phys. **16**, 10301 (2014).

[222] E. Ma, Nat. Mater. **14**, 547 (2015).

[223] J. Ding, Y.-Q. Cheng, and E. Ma, Acta Mater. **69**, 343 (2014).

[224] A. Giuntoli, F. Puosi, D. Leporini, F.W. Starr, and J.F. Douglas, Sci. Adv. **6**, eaaz0777 (2020).

[225] A.J. Cao, Y.Q. Cheng, and E. Ma, Acta Mater. **57**, 5146 (2009).

[226] H.-B. Yu, W.-H. Wang, and K. Samwer, Mater. Today **16**, 183 (2013).

[227] H. Zhang, X. Wang, H.-B. Yu, and J.F. Douglas, J. Chem. Phys. **154**, 84505 (2021).

[228] H. Zhang, X. Wang, H.-B. Yu, and J.F. Douglas, Eur. Phys. J. E **44**, 1 (2021).

[229] R. Dasgupta, H.G.E. Hentschel, and I. Procaccia, Phys. Rev. Lett. **109**, 255502 (2012).

[230] V. Hieronymus-Schmidt, H. Rösner, G. Wilde, and A. Zaccone, Phys. Rev. B **95**, 134111 (2017).

[231] M. Baggioli, I. Kriuchevskyi, T.W. Sirk, and A. Zaccone, ArXiv Prepr. ArXiv2101.05529 (2021).

[232] G. Mahmud, H. Zhang, and J.F. Douglas, J. Chem. Phys. **153**, 124508 (2020).

[233] H. Zhang, X. Wang, and J.F. Douglas, J. Chem. Phys. **151**, 71101 (2019).

[234] C. De Michele, E. Del Gado, and D. Leporini, Soft Matter **7**, 4025 (2011).

[235] F. Puosi and D. Leporini, Eur. Phys. J. E **38**, 1 (2015).

[236] F. Puosi and D. Leporini, J. Chem. Phys. **136**, 041104 (2012).

[237] M. Tsamados, A. Tanguy, C. Goldenberg, and J.-L. Barrat, Phys. Rev. E **80**, 26112 (2009).

[238] G.P. Shrivastav, P. Chaudhuri, and J. Horbach, Phys. Rev. E **94**, 42605 (2016).

[239] W.L. Johnson, J. Lu, and M.D. Demetriou, Intermetallics **10**, 1039 (2002).

[240] C. Zhong, H. Zhang, Q.P. Cao, X.D. Wang, D.X. Zhang, U. Ramamurty, and J.Z. Jiang, Scr. Mater. **114**, 93 (2016).

[241] C. Zhong, H. Zhang, Q.P. Cao, X.D. Wang, D.X. Zhang, and J.Z. Jiang, Scr. Mater. **101**, 48 (2015).

[242] C. Zhong, H. Zhang, Q.P. Cao, X.D. Wang, D.X. Zhang, J.W. Hu, P.K. Liaw, and J.Z. Jiang, J. Alloys Compd. **678**, 410 (2016).

[243] F. Shimizu, S. Ogata, and J. Li, Mater. Trans. 710160231 (2007).

[244] R.W. Hertzberg, R.P. Vinci, and J.L. Hertzberg, *Deformation and Fracture Mechanics of Engineering Materials* (John Wiley & Sons, 2020).

[245] Q.P. Cao, Y. Ma, C. Wang, X.D. Wang, and J.Z. Jiang, Thin Solid Films **561**, 60 (2014).

[246] Y. Ma, Q.P. Cao, S.X. Qu, D.X. Zhang, X.D. Wang, and J.Z. Jiang, Acta Mater. **60**, 4136 (2012).

[247] X. Wang, W.-S. Xu, H. Zhang, and J.F. Douglas, J. Chem. Phys. **151**, 184503 (2019).

[248] F. Puosi, A. Tripodo, M. Malvaldi, and D. Leporini, Macromolecules **54**, 2053 (2021).

[249] J.F. Douglas, J. Phys. Condens. Matter **11**, A329 (1999).

[250] T. Fujima, H. Frusawa, and K. Ito, Phys. Rev. E **66**, 31503 (2002).

[251] T.C. Ransom, D. Fragiadakis, and C.M. Roland, Macromolecules **51**, 4694 (2018).

[252] J. Qiao, J.-M. Pelletier, and R. Casalini, J. Phys. Chem. B **117**, 13658 (2013).

[253] G.C. Berry, Polym. Eng. Sci. **16**, 777 (1976).

[254] C.C. Yuan, Z.W. Lv, C.M. Pang, W.W. Zhu, X.-L. Wang, and B.L. Shen, J. Alloys Compd. **806**, 246 (2019).

[255] Y.J. Huang, Y.L. Chiu, J. Shen, J.J.J. Chen, and J.F. Sun, J. Mater. Res. **24**, 993 (2009).

[256] E.N. da C. Andrade, Philos. Mag. **7**, 2003 (1962).

[257] L.C.E. Struik, (1977).

[258] D.J. Plazek and I.C. Choy, J. Polym. Sci. Part B Polym. Phys. **27**, 307 (1989).

[259] C. Henderson, Proc. R. Soc. London. Ser. A. Math. Phys. Sci. **206**, 72 (1951).

[260] A.J. Kennedy, Br. J. Appl. Phys. **4**, 225 (1953).

[261] G. Lenormand, E. Millet, B. Fabry, J.P. Butler, and J.J. Fredberg, J. R. Soc. Interface **1**, 91 (2004).

[262] W.F.O. Pollett, Rheol. Acta **1**, 257 (1958).

[263] A.J. Kennedy, J. Mech. Phys. Solids **1**, 172 (1953).

[264] S. Sastry, P.G. Debenedetti, and F.H. Stillinger, Nature **393**, 554 (1998).

[265] H. Aref and S.W. Jones, Phys. Fluids A Fluid Dyn. **5**, 3026 (1993).

[266] A. Groisman and V. Steinberg, Nature **405**, 53 (2000).

[267] A. Groisman and V. Steinberg, Nature **410**, 905 (2001).

[268] R.G. Larson, Nature **405**, 27 (2000).

[269] G.K. Batchelor, *The Scientific Papers of Sir Geoffrey Ingram Taylor: Volume 1, Mechanics of Solids* (Cambridge University Press, 1958).

[270] C.A. Angell, Science (80-.). **267**, 1924 (1995).

[271] Wikimedia Foundation, (2021).

[272] J.-K. Krüger, T. Britz, J. Baller, W. Possart, and H. Neurohr, Phys. Rev. Lett. **89**, 285701 (2002).

[273] M.L. Wallace, B. Joós, and M. Plischke, Phys. Rev. E **70**, 41501 (2004).

[274] I. Kriuchevskyi, J.P. Wittmer, H. Meyer, and J. Baschnagel, Phys. Rev. Lett. **119**, 147802 (2017).

[275] H. Yoshino and M. Mézard, Phys. Rev. Lett. **105**, 15504 (2010).

[276] J. Rault, J. Non. Cryst. Solids **235**, 737 (1998).

[277] A. Perronace and A. Tenenbaum, Phys. Rev. E **57**, 100 (1998).

[278] R. Simonazzi and A. Tenenbaum, Phys. Rev. E **54**, 964 (1996).

[279] G. Szamel and E. Flenner, Phys. Rev. Lett. **107**, 105505 (2011).

[280] C.L. Klix, F. Ebert, F. Weysser, M. Fuchs, G. Maret, and P. Keim, Phys. Rev. Lett. **109**, 178301 (2012).

[281] J.P. Wittmer, H. Xu, P. Polińska, F. Weysser, and J. Baschnagel, J. Chem. Phys. **138**, 12A533 (2013).

[282] E. Flenner and G. Szamel, Phys. Rev. Lett. **114**, 25501 (2015).

[283] L. Klochko, J. Baschnagel, J.P. Wittmer, and A.N. Semenov, Soft Matter **17**, 7867 (2021).

[284] J.L. Tallon, Phys. Rev. B **29**, 4153 (1984).

[285] E.J. Banigan, M.K. Illich, D.J. Stace-Naughton, and D.A. Egolf, Nat. Phys. **9**, 288 (2013).

[286] N. Saitô, N. Ooyama, Y. Aizawa, and H. Hirooka, Prog. Theor. Phys. Suppl. **45**, 209 (1970).

[287] Y. Aizawa, Y. Kikuchi, T. Harayama, K. Yamamoto, M. Ota, and K. Tanaka, Prog. Theor. Phys. Suppl. **98**, 36 (1989).

[288] F. Baldovin and A. Robledo, Phys. Rev. E **66**, 45104 (2002).

[289] E.P. Borges, C. Tsallis, G.F.J. Añaños, and P.M.C. de Oliveira, Phys. Rev. Lett. **89**, 254103 (2002).

[290] C. Beck, Phys. Rev. Lett. **87**, 180601 (2001).

[291] P. Cao, M.P. Short, and S. Yip, Proc. Natl. Acad. Sci. **114**, 13631 (2017).

[292] M.C. Bellissent-Funel, A. Filabozzi, and S.H. Chen, Biophys. J. **72**, 1792 (1997).

[293] W. Xia, J. Song, N.K. Hansoge, F.R. Phelan, S. Keten, and J.F. Douglas, J. Phys. Chem. B **122**, 2040 (2018).

[294] R.J. Weiss, J.J. DeMarco, G. Weremchuk, L. Corliss, and J. Hastings, Acta Crystallogr. **9**, 42 (1956).

[295] M.T. Cicerone and J.F. Douglas, Soft Matter **8**, 2983 (2012).

[296] Y. Miao, L. Hong, Z. Yi, and J.C. Smith, Eur. Phys. J. E **36**, 1 (2013).

[297] A. Alesadi and W. Xia, Macromolecules **53**, 2754 (2020).

[298] A. Sanz, M. Ruppel, J.F. Douglas, and J.T. Cabral, J. Phys. Condens. Matter **20**, 104209 (2008).

[299] K.E.S. Tang and K.A. Dill, J. Biomol. Struct. Dyn. **16**, 397 (1998).

[300] G. Zaccai, Science (80-.). **288**, 1604 (2000).

[301] C.L. Soles, J.F. Douglas, and W. Wu, J. Polym. Sci. Part B Polym. Phys. **42**, 3218 (2004).

[302] M.T. Cicerone and C.L. Soles, Biophys. J. **86**, 3836 (2004).

[303] R.A. Riggleman and J.J. de Pablo, J. Chem. Phys. **128**, 224504 (2008).

[304] F. Vargas-Lara, F.W. Starr, and J.F. Douglas, Soft Matter **13**, 8309 (2017).

[305] G.J. Papakonstantopoulos, R.A. Riggleman, J.-L. Barrat, and J.J. de Pablo, Phys. Rev. E **77**, 41502 (2008).

[306] M.L. Manning and A.J. Liu, Phys. Rev. Lett. **107**, 108302 (2011).

[307] S.S. Schoenholz, A.J. Liu, R.A. Riggleman, and J. Rottler, Phys. Rev. X **4**, 31014 (2014).

[308] J. Ding, S. Patinet, M.L. Falk, Y. Cheng, and E. Ma, Proc. Natl. Acad. Sci. **111**, 14052 (2014).

[309] C. Rainone, E. Bouchbinder, and E. Lerner, Proc. Natl. Acad. Sci. **117**, 5228 (2020).

[310] X.D. Liu, T.Y. Wang, Y.F. Ye, J.C. Qiao, and Y. Yang, Comput. Mater. Sci. **155**, 104 (2018).

[311] C. Tang, Y. Li, and K. Zeng, Mater. Sci. Eng. A **384**, 215 (2004).

[312] D.Z. Chen, D. Jang, K.M. Guan, Q. An, W.A. Goddard III, and J.R. Greer, Nano Lett. **13**, 4462 (2013).

[313] T.G. Nieh, Y. Yang, J. Lu, and C.T. Liu, Prog. Nat. Sci. Mater. Int. **22**, 355 (2012).

[314] S. Kim and S. Ryu, Sci. Rep. **7**, 1 (2017).

[315] R.J.S. Ivancic and R.A. Riggleman, Soft Matter **15**, 4548 (2019).

[316] Y. Zhang and Z. Fakhraai, Proc. Natl. Acad. Sci. **114**, 4915 (2017).

[317] D.M. Dimiduk, C. Woodward, R. LeSar, and M.D. Uchic, Science (80-.). **312**, 1188 (2006).

[318] Y. Fan, B. Yildiz, and S. Yip, Soft Matter **9**, 9511 (2013).

[319] T. Zhu, J. Li, A. Samanta, H.G. Kim, and S. Suresh, Proc. Natl. Acad. Sci. **104**, 3031 (2007).

[320] Y. Lu, J. Song, J.Y. Huang, and J. Lou, Nano Res. **4**, 1261 (2011).

[321] Z.X. Wu, Y.W. Zhang, M.H. Jhon, J.R. Greer, and D.J. Srolovitz, Acta Mater. **61**, 1831 (2013).

[322] L.Y. Chen, M. He, J. Shin, G. Richter, and D.S. Gianola, Nat. Mater. **14**, 707 (2015).

[323] J. Amodeo, E. Maras, and D. Rodney, Npj Comput. Mater. **7**, 1 (2021).

[324] T. Zhu, J. Li, A. Samanta, A. Leach, and K. Gall, Phys. Rev. Lett. **100**, 25502 (2008).

[325] G.G.N. Angilella, N.H. March, C.C. Matthai, and R. Pucci, in *J. Phys. Conf. Ser.* (IOP Publishing, 2008), p. 12001.

[326] J. Shin, L.Y. Chen, U.T. Sanli, G. Richter, S. Labat, M.-I. Richard, T. Cornelius, O. Thomas, and D.S. Gianola, Acta Mater. **166**, 572 (2019).

[327] R. Gy, Mater. Sci. Eng. B **149**, 159 (2008).

[328] Y.H. Liu, C.T. Liu, W.H. Wang, A. Inoue, T. Sakurai, and M.W. Chen, Phys. Rev. Lett. **103**, 65504 (2009).

[329] B. Yang, C.T. Liu, and T.G. Nieh, Appl. Phys. Lett. **88**, 221911 (2006).

[330] R.T. Qu, Z.Q. Liu, R.F. Wang, and Z.F. Zhang, J. Alloys Compd. **637**, 44 (2015).

[331] A. Vincent and M. Meneguzzi, J. Fluid Mech. **225**, 1 (1991).

[332] J.C. McWilliams, J. Fluid Mech. **146**, 21 (1984).

[333] H.K. Moffatt, S. Kida, and K. Ohkitani, J. Fluid Mech. **259**, 241 (1994).

[334] L.F. Richardson and H. Stommel, J. Meteorol. **5**, 238 (1948).

[335] G. Boffetta and I.M. Sokolov, Phys. Rev. Lett. **88**, 94501 (2002).

[336] S. Grossmann, Ann. Phys. **502**, 577 (1990).

[337] J.P.L.C. Salazar and L.R. Collins, Annu. Rev. Fluid Mech. **41**, 405 (2009).

[338] F. Radjai and S. Roux, Phys. Rev. Lett. **89**, 64302 (2002).

[339] J. Kozicki and J. Tejchman, Granul. Matter **20**, 1 (2018).

[340] L. Viallon-Galinier, G. Combe, V. Richefeu, and A. Picardi Faria Atman, Entropy **20**, 862 (2018).

[341] N. Oyama, H. Mizuno, and K. Saitoh, Phys. Rev. Lett. **122**, 188004 (2019).

[342] S. Abedi, A.L. Rechenmacher, and A.D. Orlando, Granul. Matter **14**, 695 (2012).

[343] S. Ratynskaia, K. Rypdal, C. Knapek, S. Khrapak, A. V Milovanov, A. Ivlev, J.J. Rasmussen, and G.E. Morfill, Phys. Rev. Lett. **96**, 105010 (2006).

[344] B. Liu and J. Goree, Phys. Rev. Lett. **100**, 55003 (2008).

[345] T.E. Angelini, E. Hannezo, X. Trepat, M. Marquez, J.J. Fredberg, and D.A. Weitz, Proc. Natl. Acad. Sci. **108**, 4714 (2011).

[346] D. Bi, X. Yang, M.C. Marchetti, and M.L. Manning, Phys. Rev. X **6**, 21011 (2016).

[347] N.S. Rossen, J.M. Tarp, J. Mathiesen, M.H. Jensen, and L.B. Oddershede, Nat. Commun. **5**, 1 (2014).

[348] H.H. Wensink, J. Dunkel, S. Heidenreich, K. Drescher, R.E. Goldstein, H. Löwen, and J.M. Yeomans, Proc. Natl. Acad. Sci. **109**, 14308 (2012).

[349] K.C. Leptos, J.S. Guasto, J.P. Gollub, A.I. Pesci, and R.E. Goldstein, Phys. Rev. Lett. **103**, 198103 (2009).

[350] Y. Peng, L. Lai, Y.-S. Tai, K. Zhang, X. Xu, and X. Cheng, Phys. Rev. Lett. **116**, 68303 (2016).

[351] H.-P. Zhang, A. Be'er, E.-L. Florin, and H.L. Swinney, Proc. Natl. Acad. Sci. **107**, 13626 (2010).

[352] V. Bratanov, F. Jenko, and E. Frey, Proc. Natl. Acad. Sci. **112**, 15048 (2015).

[353] X. Bian, C. Kim, and G.E. Karniadakis, Soft Matter **12**, 6331 (2016).

[354] K. Saitoh and H. Mizuno, Phys. Rev. E **94**, 22908 (2016).

[355] P. Hähner, K. Bay, and M. Zaiser, Phys. Rev. Lett. **81**, 2470 (1998).

[356] J.-O. Krisponeit, S. Pitikaris, K.E. Avila, S. Küchemann, A. Krüger, and K. Samwer, Nat. Commun. **5**, 1 (2014).

[357] L. Laurson and M.J. Alava, Phys. Rev. E **74**, 66106 (2006).

[358] C. Maloney and A. Lemaitre, Phys. Rev. Lett. **93**, 16001 (2004).

[359] N.P. Bailey, J. Schiøtz, A. Lemaître, and K.W. Jacobsen, Phys. Rev. Lett. **98**, 95501 (2007).

[360] J. Sun, A.K. Thakur, and L. Movileanu, Langmuir **36**, 15247 (2020).

[361] A.R. Bizzarri and S. Cannistraro, Phys. Rev. Lett. **110**, 48104 (2013).

[362] G. Zheng, X.P.A. Gao, and C.M. Lieber, Nano Lett. **10**, 3179 (2010).

[363] S.M. Bezrukov and M. Winterhalter, Phys. Rev. Lett. **85**, 202 (2000).

[364] E.M. Nestorovich and S.M. Bezrukov, Chem. Rev. **112**, 6388 (2012).

[365] L.B. Kish and S.M. Bezrukov, Phys. Lett. A **266**, 271 (2000).

[366] L. Li, F. Hu, J. Jiang, and X. Cheng, Adv. Atmos. Sci. **24**, 271 (2007).

[367] C. Beck, G.S. Lewis, and H.L. Swinney, Phys. Rev. E **63**, 35303 (2001).

[368] A. Pumir, B.I. Shraiman, and E.D. Siggia, Phys. Rev. Lett. **66**, 2984 (1991).

[369] P. Chaudhuri, L. Berthier, and W. Kob, Phys. Rev. Lett. **99**, 60604 (2007).

[370] C. Tsallis, R. Mendes, and A.R. Plastino, Phys. A Stat. Mech. Its Appl. **261**, 534 (1998).

[371] N.A. Malik, PLoS One **13**, e0202940 (2018).

[372] F. Lechenault, O. Dauchot, G. Biroli, and J.-P. Bouchaud, EPL (Europhysics Lett. **83**, 46003 (2008).

[373] O. Dauchot and E. Bertin, Phys. Rev. E **86**, 36312 (2012).

[374] W.H. Wang, Prog. Mater. Sci. **57**, 487 (2012).

[375] A.S. Argon and H.Y. Kuo, Mater. Sci. Eng. **39**, 101 (1979).

[376] R.W. Hall and P.G. Wolynes, J. Chem. Phys. **86**, 2943 (1987).

[377] J.D. Honeycutt and H.C. Andersen, J. Phys. Chem. **91**, 4950 (1987).

[378] F.X. Li and M.Z. Li, J. Appl. Phys. **122**, 225103 (2017).

[379] M. Li, C.Z. Wang, S.G. Hao, M.J. Kramer, and K.M. Ho, Phys. Rev. B **80**, 184201 (2009).

[380] Y.Q. Cheng, H.W. Sheng, and E. Ma, Phys. Rev. B **78**, 14207 (2008).

[381] Y.H. Liu, T. Fujita, D.P.B. Aji, M. Matsuura, and M.W. Chen, Nat. Commun. **5**, 1 (2014).

[382] H.B. Yu, W.H. Wang, H.Y. Bai, Y. Wu, and M.W. Chen, Phys. Rev. B **81**, 220201 (2010).

[383] S. Ashtekar, D. Nguyen, K. Zhao, J. Lyding, W.H. Wang, and M. Gruebele, J. Chem. Phys. **137**, 141102 (2012).

[384] S. Ashtekar, G. Scott, J. Lyding, and M. Gruebele, J. Phys. Chem. Lett. **1**, 1941 (2010).

[385] D. Nguyen, J. Mallek, A.N. Cloud, J.R. Abelson, G.S. Girolami, J. Lyding, and M. Gruebele, J. Chem. Phys. **141**, 204501 (2014).

[386] D. Şopu, A. Stukowski, M. Stoica, and S. Scudino, Phys. Rev. Lett. **119**, 195503 (2017).

[387] J.M. Padbidri, C.M. Hansen, S.D. Mesarovic, and B. Muhunthan, J. Appl. Mech. **79**, (2012).

Appendix A Supplementary Information: String-like Cooperative Motion and Diffusion in the Interfacial Region of Ice

Cooperative particle dynamics presents one of the most characteristic features of the dynamics of glass-forming (GF) fluids. [46,68,110] As a first step in identifying cooperative particle motion, we must identify the 'mobile' atoms in interfacial region of ice. Following standard procedure in the field of GF liquids, the 'mobile' atoms are defined by comparing the self-part of the van Hove correlation function $G_s(r)$ for the strongly interacting particle fluid to an ideal uncorrelated liquid exhibiting Brownian motion. [68] $G_s(r)$ for an interacting fluid usually possesses a long tail at large distances r, indicating the existence of particles with relatively high mobility in an interacting particle system. A comparison of this kind generally produces a crossing of the $G_s(r)$ curves for the interacting and non-interacting systems, and the mobile particles are then naturally defined as those atoms whose displacements exceed the distance at the crossing point after a characteristic diffusive decorrelation time Δt defined in terms of the fourth and second moments of $G_s(r)$. [68] The van Hove correlation function of water molecules does not represent a single-peaked function, but rather has *multiple peaks* centered at successive locations. This type of $G_s(r)$ implies a 'hopping' motion to preferentially quantized distances. Therefore, we conclude that the 'mobile' atoms are essentially those particles moving a distance $r(t)$ that exceeds the typical amplitude of an atomic vibration after Δt but that is smaller than a particular distance. Mathematically, these particles are identified by a threshold condition for the atomic displacement, $a < |r_i(\Delta t) - r_i(0)| < b$, involving constants a and b that can be determined from the van Hove correlation function as shown in Figure 3.5. Then, the identification of cooperative atomic motion requires a consideration of the *relative displacement* of particles.

Collective atomic motion implies that the spatial relation between the atoms is preserved to some degree as the atoms move. Specifically, the reference mobile atoms i and j are considered to be within a collective atom displacement *string* if they remain in each other's neighbourhood, and we specify this proximity relationship by, $min[|r_i(\Delta t) - r_i(0)|, |r_i(0) - r_i(\Delta t)|] < 1.0$ Å. Atomistic simulations of GF liquids indicate that the distribution of string lengths $P(n)$ is approximately an exponential function of the number of atoms in the string n,

$$P(n) \sim \exp\left(-n/\langle n\rangle\right) \qquad \text{A.1}$$

where *P*(*n*) is the probability of finding a string of length *n* at the characteristic time, *t**. We repeat this procedure for a number of *t** intervals to achieve better statistics. Note that the 'string length' *n* is dimensionless as it involves the number of atoms participating in the string. Eq (A.1) implies that the average string length <*n*> = *L*(*t**) = *L* can then be determined from the slope of the fitted lines in Figure 3.11.

Appendix B Supplementary Information: Universal Nature of Dynamics Heterogeneity in Glass-Forming Liquids: A Comparative Study of Metallic and Polymeric Glass-Forming Liquids

A. Definition of Immobile Particles and their Clustering in Supercooled Liquids

The cage size for different alloys is defined using the same methodology as shown in Figure B.1. Apparently, the cage sizes for other systems show similar behavior with temperature as found for $Cu_{64}Zr_{36}$.

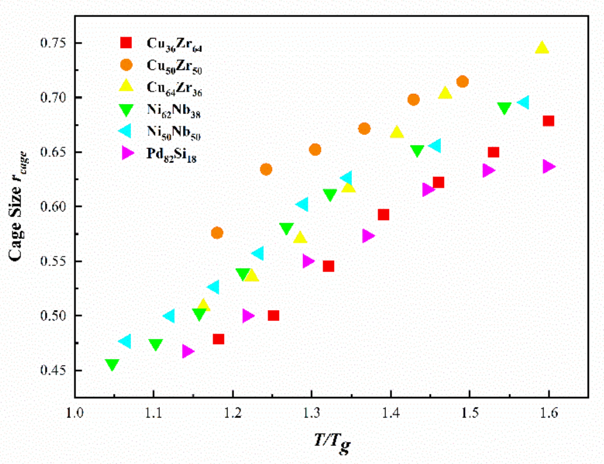

Figure B.1 The cage size as a function of reduced temperature for all metallic alloys investigated.

The fraction of caged particles as a function of time interval at different temperatures in Ni-Nb and Pd-Si alloys show similar behavior as $Cu_{64}Zr_{36}$ metallic alloy. The majority of the particles are caged initially, and over the time the population of caged particles decreases since the particles will eventually escape from the cages. Figure B.2 shows the temporal evolution of the fraction of caged particles in various metallic glass alloys at different temperatures.

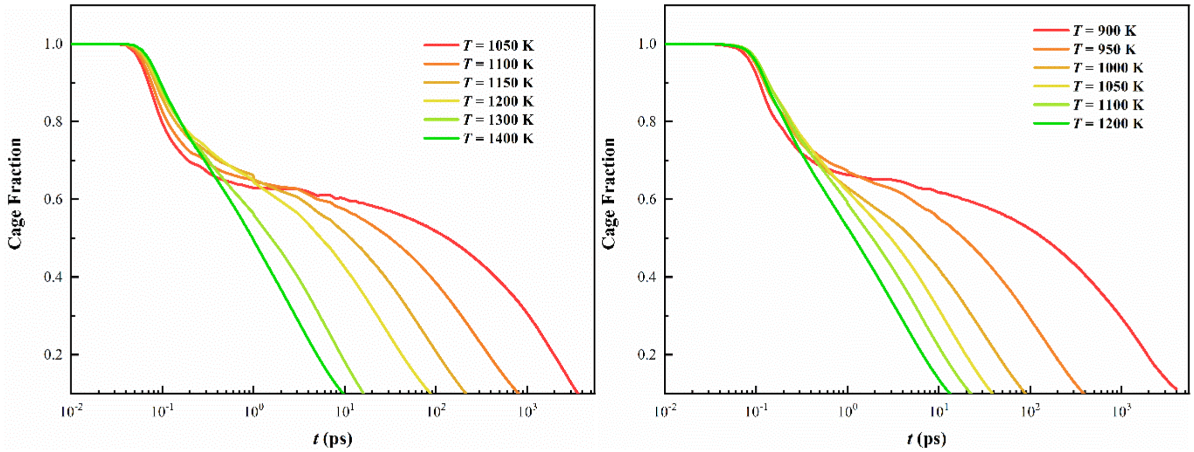

(a) (b)

Figure B.2 Dynamical fraction of caged particles as a function of time interval at different temperatures in $Ni_{62}Nb_{38}$ (a) and $Pd_{82}Si_{18}$ (b) alloys.

Figure B.3 shows the normalized cluster size for caged particles in $Ni_{62}Nb_{38}$ and $Pd_{82}Si_{18}$ alloys at different temperatures, which has similar behaviour as in $Cu_{64}Zr_{36}$ alloy, i.e., the characteristic lifetime of the clusters increases strongly with decreasing temperature.

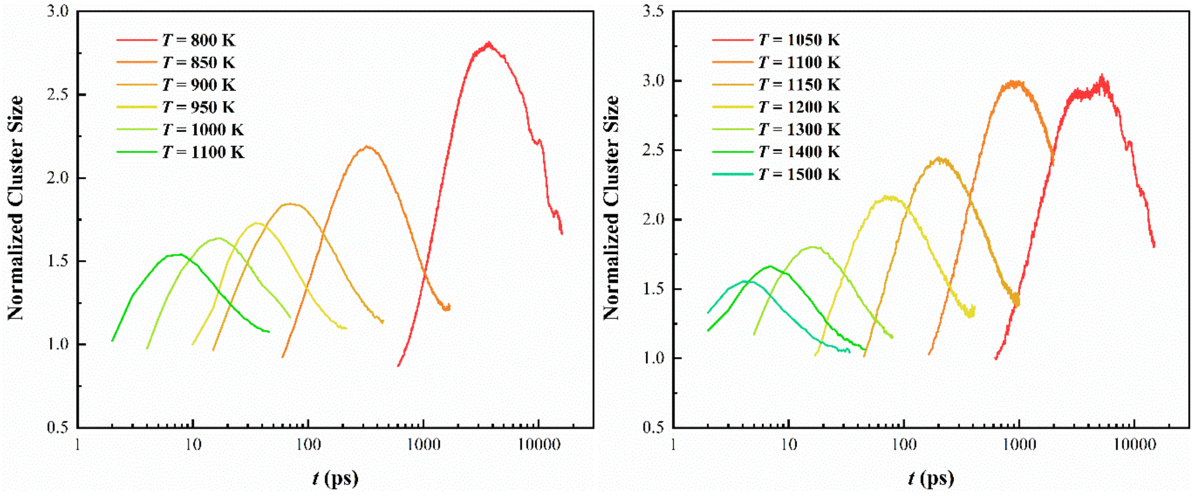

(a) (b)

Figure B.3 Normalized cluster size for caged particles in $Ni_{62}Nb_{38}$ (a) and $Pd_{82}Si_{18}$ (b) alloys at different temperatures.

Figure B.4 shows dynamical cluster sizes for immobile particles at different temperatures for $Ni_{62}Nb_{38}$ and $Pd_{82}Si_{18}$ alloys. $\langle n_I(t)\rangle$ peaks at a characteristic time t_I that increases upon cooling, and the peak value also grows on cooling in general, indicating an increase in the magnitude of mobility correlations related to the immobile particles.

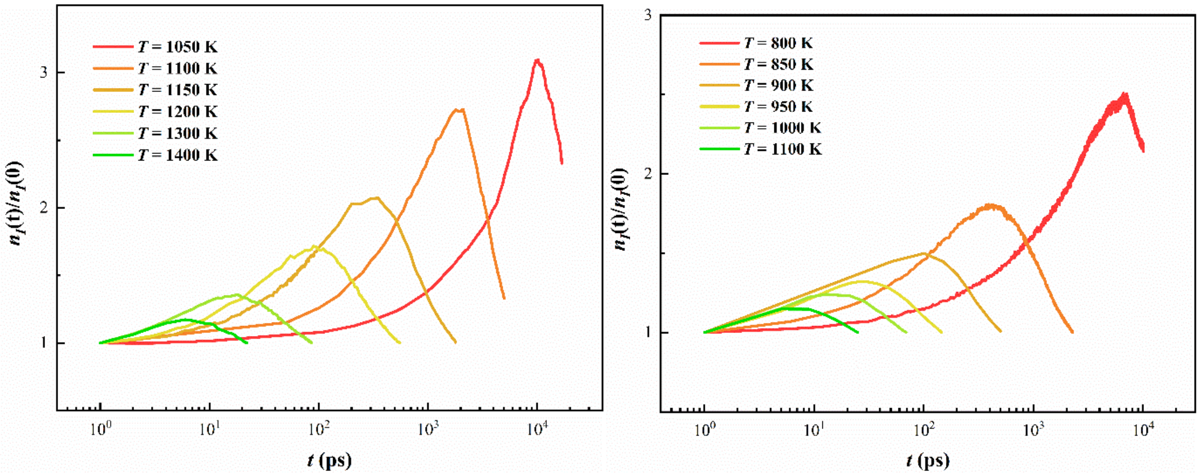

(a) (b)

Figure B.4 Dynamical cluster sizes for immobile particles $\langle n_I(t)\rangle$ at different temperatures for $Ni_{62}Nb_{38}$ (a) and $Pd_{82}Si_{18}$ (b) alloys. The data are normalized by the value at $t = 0$.

B. Size distribution of mobile and immobile particles

The mobile particles were identified by atomic displacement $a < \left|r_i\left(t^*\right) - r_i(0)\right| < b$ at t^*. t^* is the peak time of non-Gaussian parameter. a and b are determined from self-part of van-Hove function $G_s(r, t)$ at t^*. a is the value of the first minimum of the function. For higher temperatures, van-Hove functions do not possess second peaks, so we used the values at lowest temperature.

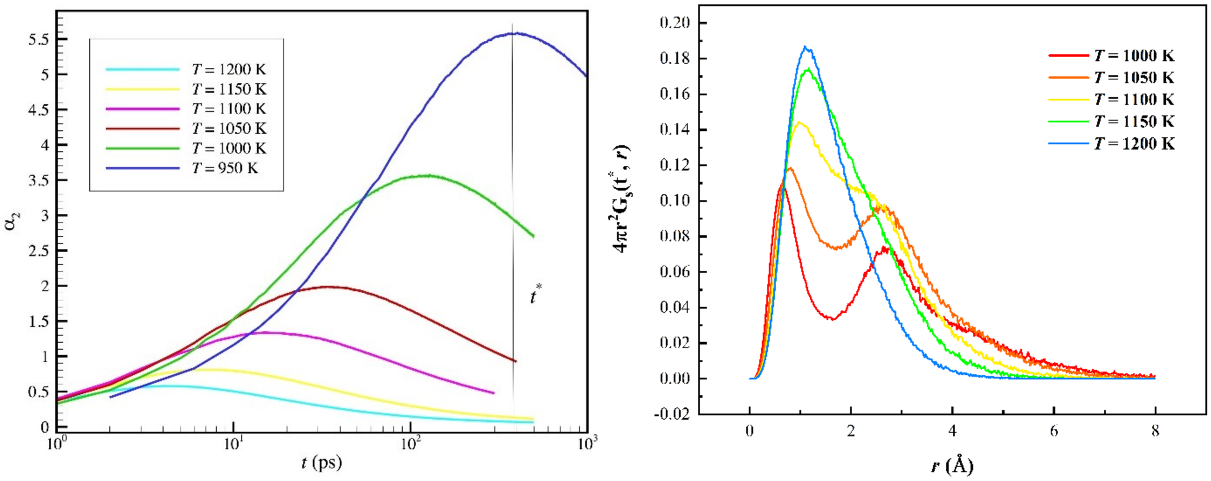

(a) (b)

Figure B.5 The non-Gaussian parameter α_2 in $Cu_{64}Zr_{36}$ as a function of temperature (a). t^* is defined as the time which α_2 exhibits a maximum. The self-part of van-Hove function $G_s(r, t)$ at t^* of $Cu_{64}Zr_{36}$ (b) at different temperatures. At lower temperatures, a notable second peak can be easily recognized.

The immobile clusters distribution can be described by the power-law $P(n) \sim n^{-\tau_F}$, with similar scaling exponent of $\tau_F \approx 1.8 \pm 0.5$, which is similar to the findings in Cu-Zr alloys reported in the main part of the paper.

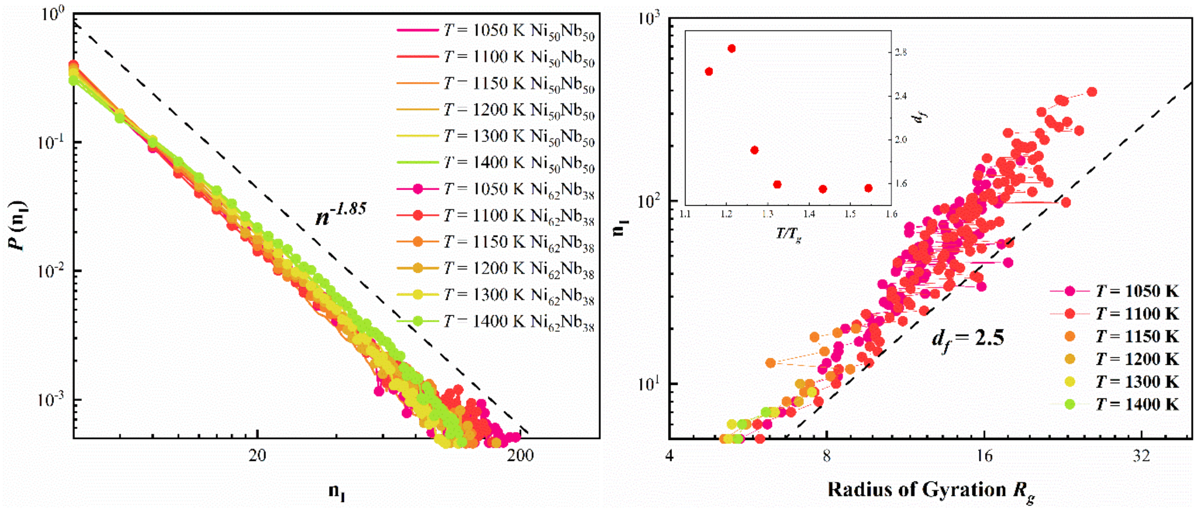

(a) (b)

Figure B.6 (a) The distribution of immobile particle cluster sizes $P(n)$ of Ni-Nb alloys. The distribution can be roughly described by a power law, so we may speak of the fractal dimension of the particle clusters. The dashed line indicates a characteristic power law with $\tau_F = 1.85$ (See text for discussion). (b) Scaling of immobile cluster radius of gyration R_g with its mass n, $n \sim R_g{}^{d_f}$ in the $Ni_{62}Nb_{38}$ alloy. The inset shows that the fractal dimension, d_f, varies with temperature. The general trend is consistent with our finding for the $Cu_{64}Zr_{36}$ alloys reported in the main text, and previous findings of Starr et al. for polymer melts. [55,192]

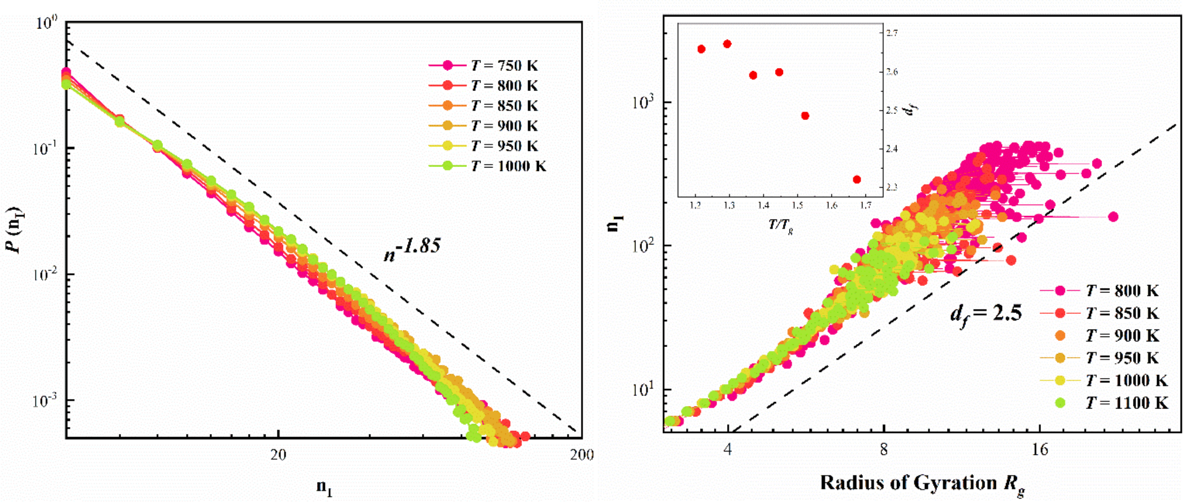

(a) (b)

Figure B.7 (a) The distributions of immobile particle cluster sizes $P(n)$ of $Pd_{82}Si_{18}$ alloys. The distribution can be described by a power law, and the dashed line indicates a characteristic power-law with $\tau_F = 1.85$. (b) Scaling of immobile cluster radius of gyration R_g with its mass n, $n \sim R_g^{d_f}$ in the $Pd_{82}Si_{18}$ alloy. The inset shows that the fractal dimension, d_f, shows a similar trend as in Figure B.6.

C. Correlation Between Locally Well-Packed Voronoi Polyhedra and Immobile Particles

In the previous study, a relationship between dynamic heterogeneity and atomic local structure was shown to exist in simulated Cu-Zr metallic glass materials. [28] This dynamics-structure correspondence was based on Voronoi tessellation, a widely used measure for quantifying local atomic structure. In particular, “local structure” is defined in this previous work by the Voronoi index $\langle n_3, n_4, n_5, n_6 \rangle$, where n_i represents the number of i-edged faces in a Voronoi cell. [377] We revisit this analysis in the present work to determine the extent to which immobile particles overlap with well-packed particles defined by the Voronoi tessellation.

We first characterize the Voronoi index ⟨0,0,0,12⟩ of Cu-centered atoms in $Cu_{64}Zr_{36}$ alloys at 950 K, known as full icosahedral (FI) Voronoi cells, and consider how these regions correlate with the Debye-Waller factor $\langle u^2 \rangle$ of atoms in the centers of these cells, defined by their mean square displacements after a caging time of 1 ps. A strong qualitative correlation between $\langle u^2 \rangle$ of these central atoms and the Voronoi index is shown in Figure B.8 for this metallic glass system, i.e., particles having a lower $\langle u^2 \rangle$ often arise in close-packed regions. In particular, we observe that atoms having a Voronoi index $\langle 0,0,0,12 \rangle$ tend to have especially low-mobility and these atoms and associated Voronoi cells form a polymeric network in Cu-Zr alloys. [28,378,379]

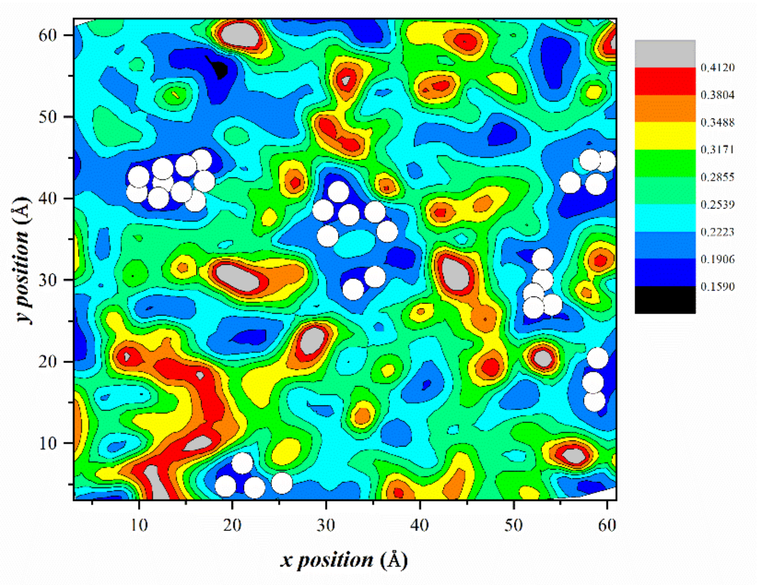

Figure B.8 Correlation between Voronoi index $\langle 0,0,0,12 \rangle$ of Cu-centered atoms and DWF $\langle u^2 \rangle$ in $Cu_{64}Zr_{36}$ alloys at 950 K. Contoured map shows the spatial distribution of DWF in the $Cu_{64}Zr_{36}$ alloys at 950 K. The slab has a thickness of 2.5 Å. The sidebar illustrates the range of DWF, darker color corresponding to the region with smaller value of DWF $\langle u^2 \rangle$. White spots on the map represent Cu particles with Voronoi index $\langle 0,0,0,12 \rangle$.

We next examine more quantitatively the correlation between dominant polyhedron and immobile particles in Cu-Zr systems. The fraction of Cu-center full icosahedral polyhedron in Figure B.8 increases dramatically upon approaching the glass transition temperature, T_g. Near T_g, the fraction in $Cu_{64}Zr_{36}$ is almost 25%, as noted in our previous study. [28] $Cu_{64}Zr_{36}$ also has the highest fraction of Cu-centered FI polyhedra among all three compositions. In all the Cu particles within the FI polyhedra, nearly 72% can be classified as being "immobile" near T_g for $Cu_{64}Zr_{36}$. We conclude that the slowing down of the dynamic in this metallic glass can be associated with a large population of fully icosahedral Voronoi polyhedra. Previous atomic simulation study has also indicated that significant amount of atoms (up to 70%) with icosahedral local packing are immobile. [380] The other two systems show similar values, despite the smaller number of particles exhibiting local close-packed configurations. Clearly, atomic configurations exhibiting closed-packed configurations are more likely to be immobile in Cu-Zr alloys. The generality of this relation between structure and dynamics remains a question, however, so we examined other metallic glasses to assess this question. Unfortunately, we found that the particular relation between local structure and dynamics found for Cu-Zr alloys does not extend to other metallic glasses.

We applied the same analysis in Cu-Zr alloys to Pd-Si alloys. Although there is a much smaller fraction full icosahedra in Pd-Si alloys (e.g., the fraction of full icosahedral polyhedral Voronoi cells in $Pd_{82}Si_{18}$ is 1.50%, which is much lower than the fraction in Cu-Zr alloys noted above), we still found the fraction of immobile particles in full icosahedral polyhedral cells to be close to 68.81% near T_g. However, for Cu-Zr systems, nearly 99% of particles exhibit full icosahedral polyhedron near T_g and the particles at the centers of these cells can be recognized as immobile particles. The correlation between full icosahedron and immobile particles is thus much weaker in Pd-Si systems than in Cu-Zr metallic glass-forming systems. Since Pd-Si does not have significant fraction of full icosahedral polyhedra, we take the most dominant Voronoi polyhedra instead in this system to test how these structurally distinct particles relate to the immobile particles.

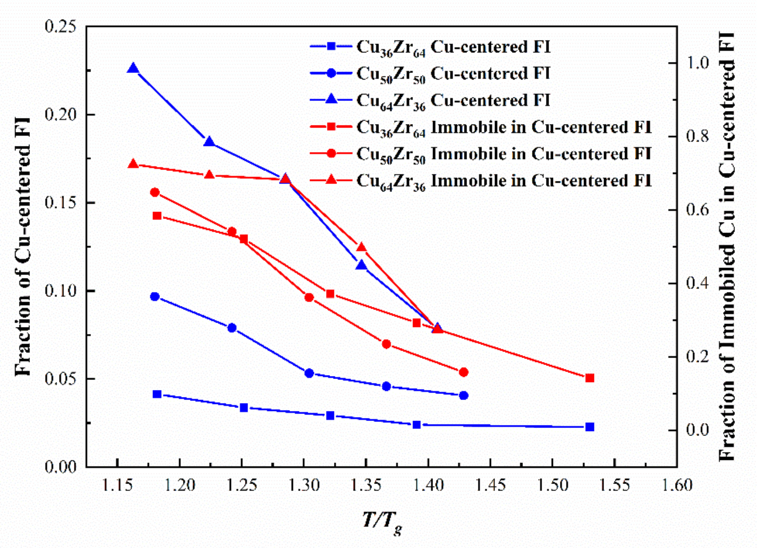

Figure B.9 Correlation between Cu-centered full icosahedral polyhedron and immobile clusters in Cu-Zr systems. Three compositions are considered, $Cu_{36}Zr_{64}$, $Cu_{50}Zr_{50}$, $Cu_{64}Zr_{36}$, over temperature range from 850 K to 1150 K. Blue dots represent fraction of Cu-centered full icosahedral polyhedron. Red dots represent fraction of immobile clusters in Cu particles with full icosahedral polyhedron.

Figure B.10 shows that the fractions of immobile clusters in different Si-centered VPs vary with the fractions of VPs. The fraction of immobile particles in Si-centered ⟨0,4,4,0⟩ increases as the temperature increase, but the fraction of immobile particles in this VP decreases. Fraction of immobile particles in Si-centered ⟨0,3,6,0⟩ shows contrast tendency. Both fractions decrease as we increase the temperature. We can conclude that although some correlation exists between immobile particles and symmetric Voronoi polyhedral cells associated with local close-packing, there is no general predictive relationship between Voronoi type and local mobility. The search for a structural indicator of local mobility thus continues.

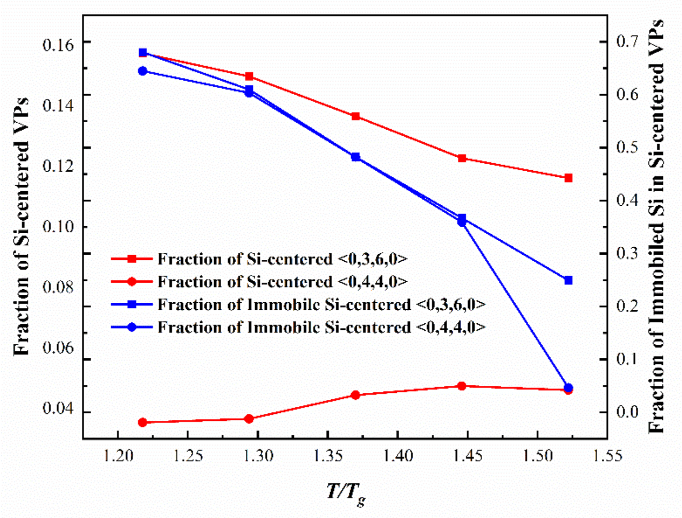

Figure B.10 Correlation between Si-centered ⟨0,4,4,0⟩ and ⟨0,3,6,0⟩ polyhedra and immobile clusters in Pd-Si systems over temperature range from 800 K to 1050 K. Red dots represent the fractions of different Si-centered VPs. Blue dots represent the fraction of immobile particles in those VPs.

To further investigate the correlation between Voronoi polyhedral and immobile clusters, we also compared the distributions of immobile clusters and the clusters of the dominant VPs. Both the immobile particle cluster size distribution and icosahedral polyhedral cluster size distribution can be described as being approximately exponential $P(n) \sim \exp(-n/n_0)$, where n_0 is a constant, but there does seem to be an approach to a power law, $P(n) \sim n^{-\tau_F}$, at low temperatures with a scaling exponent $\tau_F \approx 2$. This crossover is illustrated in Figures 4.7(b) and B.11(a). Even though this scaling exponent is similar, suggesting the growth of branched polymeric structures at equilibrium [192], the size range of the Voronoi polyhedron clusters is quite different from the immobile particle clusters. Apparently, immobile clusters have a significantly larger size ranging from 2 to 80 in our dimensionless units, while the icosahedral polyhedral Voronoi cell clusters vary in size from 2 to 50. As we increase the temperature, the Voronoi cell average cluster size progressively decreases, and at higher temperatures, these clusters contain only between about 2 to 10 atoms, a trend again inconsistent with the immobile cluster size variation with temperature. Since Pd-Si does not possess significant amount of full icosahedral polyhedral Voronoi cells, we examine the cluster distribution of VP ⟨0,3,6,0⟩ and ⟨0,4,4,0⟩ clusters, in Figure B.11(b).

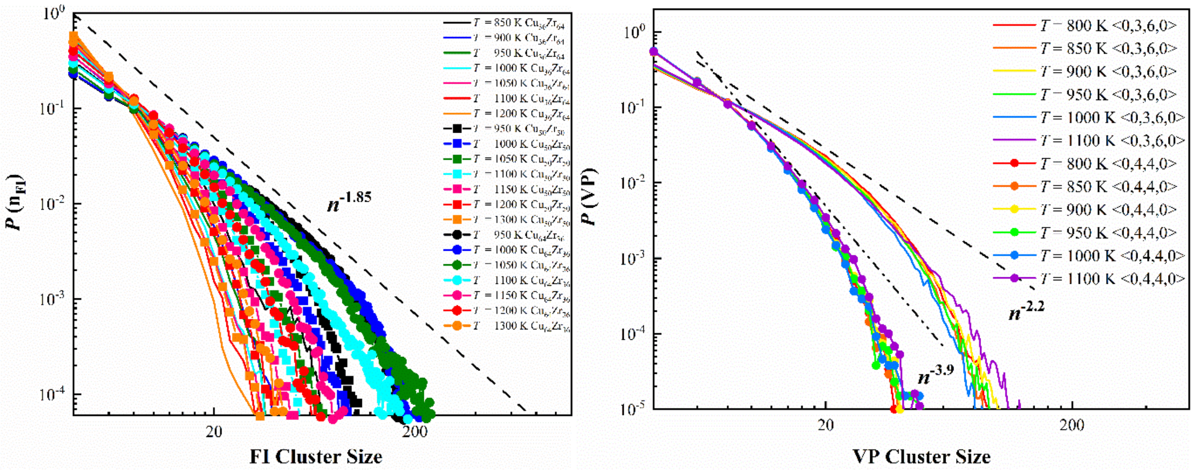

(a) (b)

Figure B.11 (a) The distribution of cluster sizes of particles with full icosahedral polyhedron of Cu-Zr systems for all T studied. (b) The distribution of cluster sizes of particles with VP ⟨0,3,6,0⟩ and ⟨0,4,4,0⟩ of $Pd_{82}Si_{18}$ for all T studied. The dashed lines indicate power-law curves in comparison to the data.

Apparently, the approach to a power-law scaling at low temperatures is not convincing for these clusters, which is an indication of a lack of a direct correspondence between the Voronoi clusters and the immobile particle clusters. We thus observe further evidence that while well-packed particles tend to be somewhat immobile, locally well-packed particles as defined by a Voronoi construction to determine local density does not reliably predict local mobility and the clusters of the atoms exhibiting locally preferred packing exhibit a distinct geometry from the immobile particles.

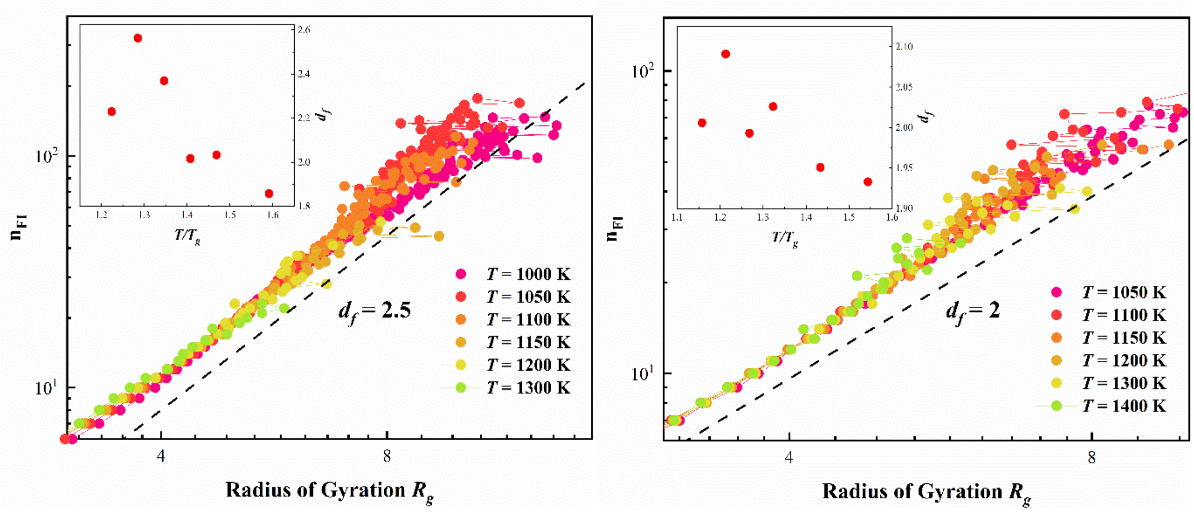

(a) (b)

Figure B.12 Scaling of full icosahedral polyhedron cluster radius of gyration R_g with its mass n, $n \sim R_g^{d_f}$ in the $Cu_{64}Zr_{36}$ (a) and $Ni_{62}Nb_{38}$ (b) alloys. The inset shows that the fractal dimension, d_f, varies slowly from a value around 2 for smaller clusters to a value of about 2.5 for $Cu_{64}Zr_{36}$ alloy, but d_f remains close to 2 for the $Ni_{62}Nb_{38}$ alloy. This general trend of d_f is consistent with expectations that the clusters have a geometry with equilibrium polymers. [192]

Appendix C Supplementary Information: The Initiation of Shear Band Formation in Deformed Metallic Glasses From Soft Localized Domains

A. Definition of Mobile Particles

We follow the methodology developed by Starr et al. [55] to estimate the fraction of 'mobile particles'. In particular, we first bin particles according to the magnitude of their relative displacement as a function of time for a range of threshold fractions, e.g., the 1 % fraction of particles having greatest displacement, the 2 % fraction of particles having greatest displacement, etc. The particles in these classes are 'relatively mobile' to a degree that depends on the cut-off fraction. Clustering of these relatively mobile particles can be defined for each cut-off value as groups of these particles whose nearest-neighbor distance is less than the nearest-neighbor distance defined with reference to the radial distribution function. Following Starr et al., the effect of trivial clusters that exist for randomly located particles is accounted for in the definition of the average cluster mass of these relatively mobile particles. In particular, the average mass of the mobile clusters is normalized by the cluster mass of the same fraction of particles chosen at random. [55] The normalized mass of the relatively mobile particles exhibits a peak for each cut-off value and a *unique* cut-off value can be determined by the particular cut-off size at which the mobile cluster mass is maximized. If the cut-off had been chosen too small then one only determines fragments of the mobile particles of interest and if the cut-off is chosen too large, then one starts to incorporate particles that exist because of clustering at random. The methodology allows one to zero in on the average cut-off value in a systematic and objective fashion. The data in Figure C.1 indicates the normalized maximum cluster size maximizes at a cut-off value of 2.75 % for this material. Specifically, we define 'mobile particles' as those particles that have the top 2.75 % displacement at any time *t*. The time at which the average mass of the mobile particle peaks is the mobile particle lifetime, τ_M. See Starr et al. for illustration of the time dependence of the mobile particle mass.[55] The near linear relation between τ_M and the peak in the non-Gaussian parameter t^* shown in Figure 5.5(a) of the main paper relies only on holds when the fraction of mobile particles is estimated with some precision (roughly about 2.75 % ± 1.0 %) because the mobile particle lifetime τ_M slightly depends on the choice of cut-off for defining mobile particles.

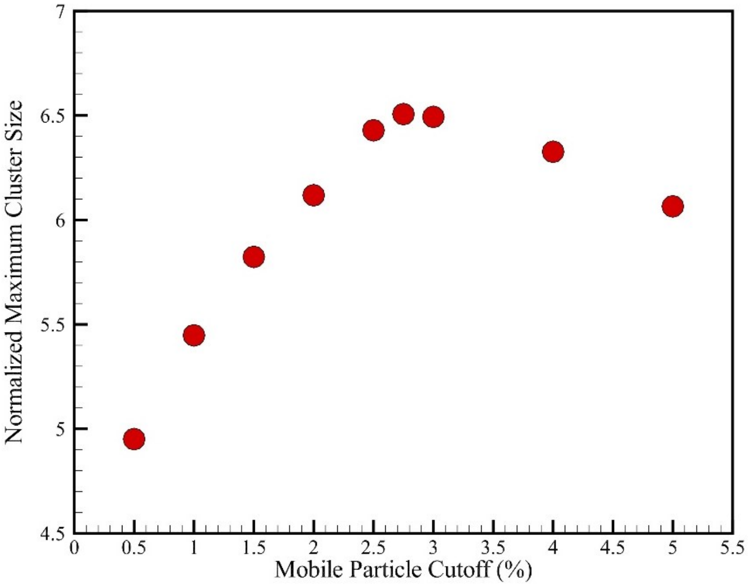

Figure C.1 Normalized maximum cluster size as a function of mobile particle cutoff when ε = 7.0 % in a sample with h = 300 Å at T = 50 K.

B. Spatial and size distribution and fractal geometry of mobile particles in the interior and interfacial regions

We next examine the geometry of the mobile particles in interior and interfacial regions. We calculate the fractal dimension, d_f, to characterize the geometrical properties of mobile clusters in both regions. The 'fractal' dimension of the mobile clusters is calculated using the relation, $n \sim R_g^{d_f}$, where n is the number of particle clusters and R_g is the radius of gyration of the given clusters which is calculated using the equation: $R_g^2 = \frac{1}{2N}\sum_{i,j}\left(r_i - r_j\right)^2$ (N is the total number of mobile particles in the cluster and r_i, r_j are the positions of the i^{th} and j^{th} particles). As shown in the inset of Figure C.2, we found out that d_f varies between 2.6 and 2.9 in the strain range and regions that we studied, similar to the findings in our previous studies on mobile clusters in the metallic glasses systems at temperatures above the glass transition temperature, T_g [247]. Next, we consider the size distribution of the mobile particle clusters in both regions. $P(n)$ can be described using a power law $P(n) \sim n^{-\tau_F}$ where τ_F is the size distribution scaling exponent. As illustrated in Figure C.3, we see that τ_F around 1.5 in both regions. The size distribution exponent ('Fisher exponent') for mobile particle clusters is also nearly the same as we have seen before [247] for the same metallic glass system for a T range much greater than T_g so there is apparently no essential difference in the geometry of the mobile particle clusters above and below T_g.

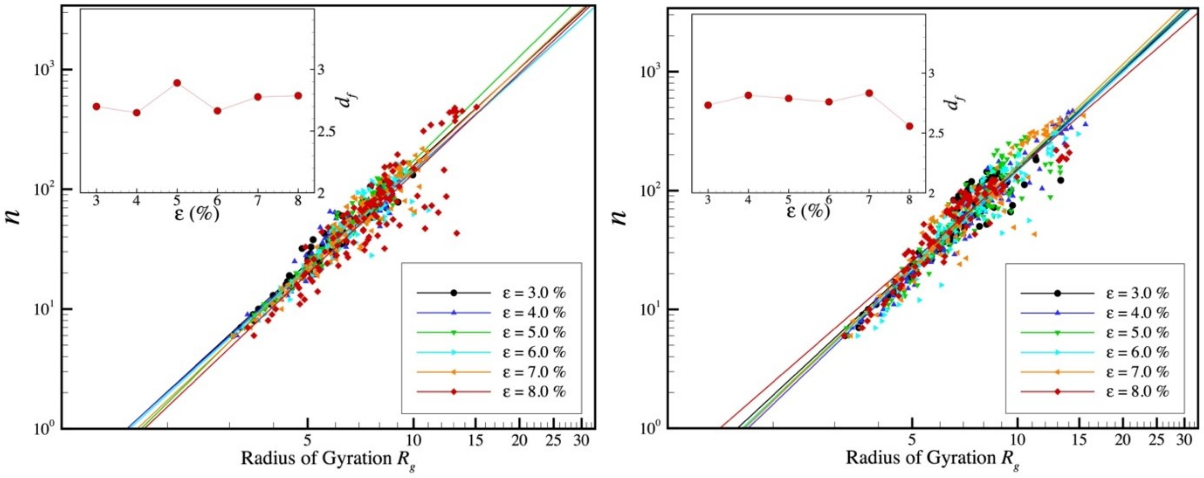

(a) (b)

Figure C.2 Cluster radius of gyration R_g with its mass n, $n \sim R_g^{d_f}$ at different strains in the interior (a) and interfacial (b) regions. The inset shows that the fractal dimensions, d_f, do not vary significantly with strain or regions. The fractal dimensions in both regions are around 2.8.

We show some randomly selected mobile particle clusters in the interior and interfacial regions of the metallic glass (MG) in the inset where it is apparent that these clusters take a relatively compact and symmetric form. This is natural since a perfectly compact object, like a sphere, has a fractal dimension $d_f = 3$. Notice that the average mass of these clusters ranges from about 10 to 500. Based on our discussion in the main text indicating that the lifetime of the mobile particles can be identified with the Johari-Goldstein (JG) relaxation time and the commonly stated correlation between the JG relaxation process and shear transformation zones (STZs), we suggest that the 'mobile particle clusters' can be identified as being a concrete realization of STZs [226,381,382]. Recent atomic resolution imaging of the interface of metallic glass and other glass-forming liquids using ultrahigh vacuum scanning microscopy have indicated the presence of relatively compact mobile particle clusters on the surface of glasses deep in their glass state where the dynamics of their rearrangement motion was suggested to be consistent with the JG relaxation process and where the size of the clusters was estimated to be in the range of 4 to 5 atom diameters [383–385]. The appearance and reported size of these clusters seem to be consistent with our simulations. Further comparisons between simulation and these clusters observations seem warranted.

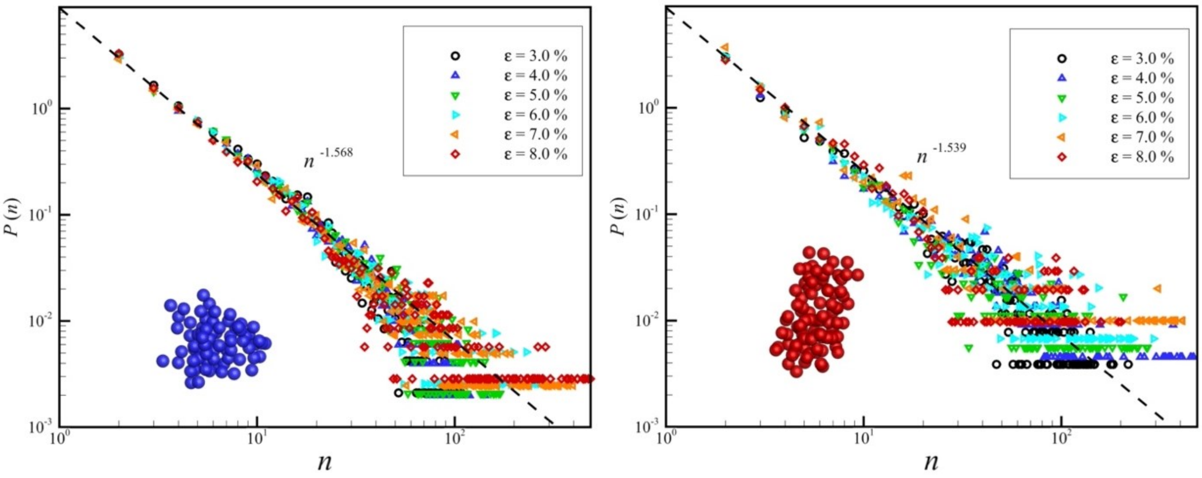

(a) (b)

Figure C.3 The distribution of mobile particle cluster sizes $P(n)$ in the interior (a) and interfacial (b) regions at different strains. The distribution can be described using a power law with size distribution exponent (Fisher exponent) τ_F around 1.5. Atomic configurations of representative clusters in both regions at ε = 8.0 % are also shown.

C. New Protocol to Eliminate Stress Fluctuation

First, we examine the stress vs. strain relation in our material, which is indicated in the Figure 5.1(a) in the chapter 5. The stress fluctuations in the large deformation regime are well-known and expected for glass materials beyond their point of “yield” and this is naturally attributed to the highly heterogeneous nature of the material in its shear banded state. The fluctuations at low strain are another matter. We did not expect “fluctuation effects” in this regime and it is a fair question to ask where these fluctuation effects come from. The magnitude of the estimated $<u^2>$ showed some fluctuations in this low deformation regime so we considered further what these “fluctuations at low ε might represent.

It then occurred to us that the quench process of our metallic glass might lead to appreciable residual stresses in the low temperature that might be relieved small amplitude deformations. There have been many experimental and computational reports recently of how the application of small stresses can alter the "energy landscape" of glassy materials so this seemed like a plausible reason for the appreciable stress fluctuation effects that we observe at very low deformations. To check this hypothesis, we subjected the material to a very small prestress (deformation) to allow these hypothetical residual stresses to relax and then took the resulting material to be our relaxed undeformed material. This procedure not only essentially eliminated the stress fluctuations at low ε (see inset to Figure C.4), this pre-stress procedure also essentially eliminated the "noisy" nature of the average value of $<u^2>$ data at low deformation. The average value of $<u^2>$ at $\varepsilon = 0$ % is now quite consistent with the average value of predicted from expression in the paper.

The random fluctuations of $<u^2>$ as function of time on a ps timescale in apparent in Figure C.4 are to be expected and we have studied this phenomenon extensively in our previous works on glass-forming materials and the interfacial dynamics of crystalline materials. The time series no doubt exhibits colored noise which is characteristic of dynamic heterogeneity in glass-forming liquids and this phenomenon is particularly associated with the Johari-Goldstein relaxation process, as we discuss in our recent paper focusing on this relaxation process [227]; (see Fig. 4a of this paper where a similar time series is discussed for the Al-Sm metallic glass at low temperatures). We also see a nice example of this type of fluctuation in our study of the interfacial dynamics of TIP4P ice [147] (See Fig. 12), the interfacial dynamics of crystalline Ni [48] (See Fig. 8) and in the internal dynamics of the protein ubiquitin [123]. This colored noise phenomenon is discussed extensively in papers dedicated to understanding colored noise in relation to dynamic heterogeneity [13,119].

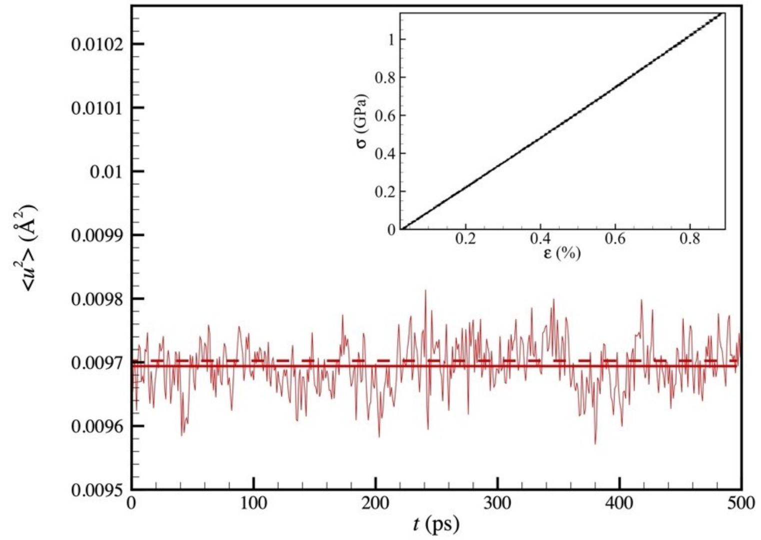

Figure C.4 Stress versus strain in deformed ZrCu material subjected to pre-stress and resulting time series of $<u^2>$ as a function of time t and $\varepsilon = 0$. The power spectrum of $<u^2>$ fluctuation in the undeformed state exhibits a power-law scaling with frequency, where the color noise exponent is equal to 0.35. The dashed horizontal line represents the predicted average value of $<u^2>$ from the expression for $<u^2>$ versus ε given our paper and the solid horizontal line represents the average value of $<u^2>$ over 500 ps in the undeformed state. The inset of this paper shows the stress versus strain relation of the pre-stressed material where we see that the "fluctuations" observed before have now been essentially eliminated.

Since we have previously observed in many condensed matter systems that temperature greatly influences the noise color, it is natural to expect that deforming the material should also alter the color of the noise in times series for $<u^2>$, the potential energy and other properties probing the local molecular environment of the particles in the material. A study of how strain influences this time of colored noise is an obvious topic for a future publication, but such an analysis is beyond the scope of the present paper.

D. Turbulent-like State of the Shear Band Region

Figure C.5 shows the local shear modulus distribution captured from the system with h = 300 Å which contains part of the SB shown in blue, with the displacement vector in the corresponding region.

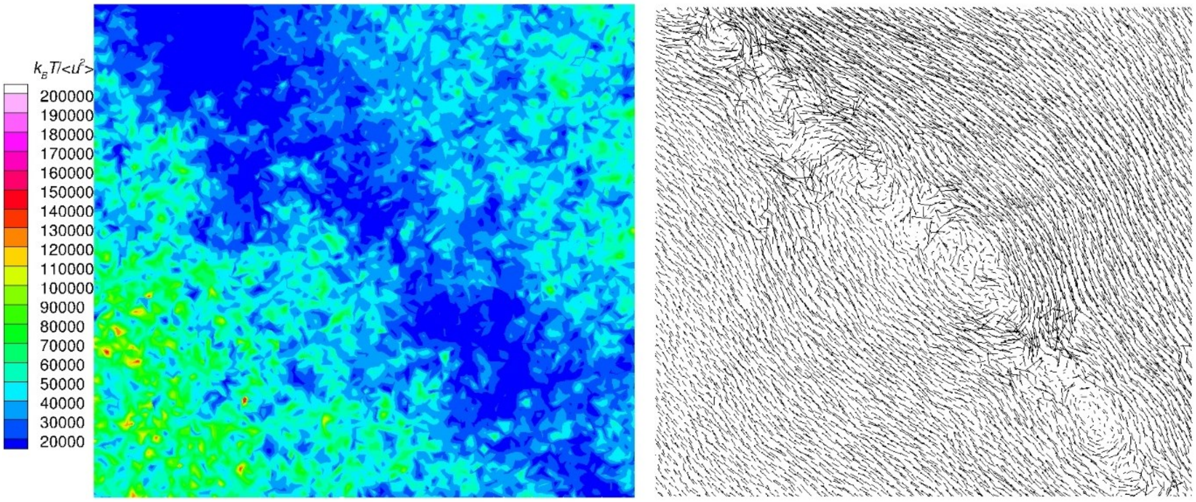

Figure C.5 Contour map of local shear modulus $k_B\ T\,/<u^2>$ around shear band in the system with thickness h = 300 Å, and displacement vector in the corresponding region at ε = 8.9 %, corresponding to shear banded state. From the corresponding particle displacement vector, a circular collective, and vortex-like motion has been observed, similar to the findings from Sopu's work [386]. This is also a common type of collective motion seen in dense granular materials [387].

This type of vortex-like motion has been previously reported in the SB region and these coherent vortex-like structures were interpreted to arise from the percolation of smaller STZs structures [386]. Note the vortex patterns involving collective particle displacement that are also characteristic of turbulent fluids and other materials that have been characterized by analogy as being “turbulent”.